İSTANBUL TECHNICAL UNIVERSITY ★ INSTITUTE OF SCIENCE AND TECHNOLOGY

INVERSE SCATTERING PROBLEMS FOR THE OBJECTS BURIED IN PENETRABLE CYLINDERS

Ph.D. Thesis by
Fatih YAMAN

Department : Electronics and Communications Engineering

Programme : Telecommunications Engineering

NOVEMBER 2009

İSTANBUL TECHNICAL UNIVERSITY ★ INSTITUTE OF SCIENCE AND TECHNOLOGY

INVERSE SCATTERING PROBLEMS FOR THE OBJECTS BURIED IN PENETRABLE CYLINDERS

Ph.D. Thesis by
Fatih YAMAN
(504042309)

Date of submission : 15 July 2009
Date of defence examination : 05 November 2009

Supervisor (Chairman) : Assoc. Prof. Dr. Ali YAPAR (ITU)
Co-Supervisor : Prof. Dr. Rainer KRESS (U. of Göttingen)
Members of the Examining Committee : Prof. Dr. İbrahim AKDUMAN (ITU)
Prof. Dr. İrşadi AKSUN (Koç U.)
Prof. Dr. Tayfun GÜNEL (ITU)
Prof. Dr. Mevlüt TEYMÜR (ITU)
Assoc. Prof. Dr. İbrahim TEKİN (Sabancı U.)

NOVEMBER 2009

İSTANBUL TEKNİK ÜNİVERSİTESİ ★ FEN BİLİMLERİ ENSTİTÜSÜ

GEÇİRGEN SİLİNDİRLER İÇERİSİNE GÖMÜLÜ CİSİMLER İÇİN TERS SAÇILMA PROBLEMLERİ

DOKTORA TEZİ

Fatih YAMAN
(504042309)

Tezin Enstitüye Verildiği Tarih : 15 Temmuz 2009
Tezin Savunulduğu Tarih : 05 Kasım 2009

Tez Danışmanı	:	**Doç. Prof. Dr. Ali YAPAR (İTÜ)**
Eş-Danışman	:	**Prof. Dr. Rainer KRESS (Göttingen Ü.)**
Diğer Jüri Üyeleri	:	**Prof. Dr. İbrahim AKDUMAN (İTÜ)**
		Prof. Dr. İrşadi AKSUN (Koç Ü.)
		Prof. Dr. Tayfun GÜNEL (İTÜ)
		Prof. Dr. Mevlüt TEYMÜR (İTÜ)
		Doç. Dr. İbrahim TEKİN (Sabancı Ü.)

KASIM 2009

FOREWORD

It was a great pleasure for me to study on my thesis under the supervision of Prof. Dr. Rainer Kress and feel myself lucky for carrying this honour for the rest of my life. Furthermore, I thank to Assoc. Prof. Dr. Ali Yapar for the guidance to my studies in Istanbul Technical University.

I am grateful to Dr. Olha Ivanyshyn for her scientific suggestions to improve the qualities of my studies and continuous moral support which have helped to keep my patience against to all non-scientific issues. Additionally, I thank to Dr. Serkan Şimşek and Dr. Mehmet Çayören for their supports in a friendly manner.

Moreover, the hospitability of the Numerical and Applied Mathematics Institute at Georg-August University of Göttingen and the financial support of DAAD (German Academic Exchange Service) for my studies are thankfully acknowledged.

Since this thesis is the most precious thing I have ever had till now, I would like to devote it to my parents Gülen & Hüseyin Yaman and to my sister Hilâl Yaman Taşkıran.

November 2009 Fatih YAMAN

TABLE OF CONTENTS

ABBREVIATIONS

CBC	:	Conductive Boundary Condition
IBC	:	Impedance Boundary Condition
TBC	:	Transmission Boundary Condition
PEC	:	Perfect Electric Conductor
MoM	:	Method of Moments

LIST OF TABLES

LIST OF FIGURES

Page

LIST OF SYMBOLS

$\boldsymbol{E}$	:	Electric field vector
$\boldsymbol{d}$	:	Direction of electromagnetic wave propagation
$\boldsymbol{\phi}_0$	:	Incidence angle
$\boldsymbol{\Gamma}_0$	:	Boundary curve of the buried obstacle
$\boldsymbol{\Gamma}_1$	:	Boundary curve of the penetrable cylinder
$\boldsymbol{\nu_0}$	:	Normal vector to Γ_0
$\boldsymbol{\nu_1}$	:	Normal vector to Γ_1
$\boldsymbol{D}_0$	:	Domain bounded by Γ_0 and Γ_1
$\boldsymbol{D}_1$	:	Unbounded background medium
$\boldsymbol{\Phi}_m(x,y)$	:	Fundamental solution to the two-dimensional homogeneous, Helmholtz equation with wave number k_m
$\boldsymbol{u}_0$	:	Total Field in the domain D_0
$\boldsymbol{u}_1$	:	Total Field in the domain D_1
$\boldsymbol{u}^i$	:	Incident field
$\boldsymbol{u}^s$	:	Scattered field
$\boldsymbol{u}_\infty$	:	Far-field
$\boldsymbol{k}_0, \boldsymbol{k}_1$	:	Wave numbers of the domains D_0 and D_1
$\boldsymbol{\varepsilon}_0, \varepsilon_1$	:	Electric Permitivites of the domains D_0 and D_1
$\boldsymbol{\sigma}_0, \sigma_1$	:	Conductivities of the domains D_0 and D_1
$\boldsymbol{\mu}_0, \mu_1$	:	Magnetic Permeabilities of the domains D_0 and D_1
$\boldsymbol{\Omega}$	:	Unit circle
$\boldsymbol{\Omega}^m$	:	Measurement circle
$\boldsymbol{\omega}$	:	Radial frequency
$\mathbf{H_n^{(1)}}$	:	Hankel function of the first kind of order n
$\mathbf{J_n}$	:	Bessel function of order n
$\mathbf{Y_n}$	:	Neumann function of order n
ψ, ϕ, χ	:	Density functions
$\mathbf{S}$	:	Single-layer operator
$\mathbf{K}$	:	Double-layer operator
$\mathbf{K}'$	:	Normal derivative of the single-layer operator
$\mathbf{T}$	:	Normal derivative of the double-layer operator
$\mathbf{I}$	:	Identity operator
$\mathbf{S}_\infty$	:	Far-field operator
$\boldsymbol{\eta}$	:	Inhomogeneous impedance function
$\boldsymbol{\lambda}$	:	Inhomogeneous conductivity function
$\boldsymbol{\delta}$	:	Noise ratio
$\alpha, \alpha_1, \alpha_2, \beta_1 \beta_2$	:	Tikhonov regularization parameters
R , M	:	Degree of polynomials used in Least Squares Approximation
n , N	:	Number of discretization points
C	:	Euler Constant
$\mathbf{SC_1}, \mathbf{SC_2}$	:	Stopping criterias
$\bar{\varepsilon}_1, \bar{\varepsilon}_2$	:	Stopping criteria bounds

$\mathbf{ERR}^{\boldsymbol{\eta}}$	:	Percentage error obtained by the reconstruction of η
$\mathbf{ERR}^{\boldsymbol{\lambda}}$	:	Percentage error obtained by the reconstruction of λ
$\mathbf{ERR}^{\boldsymbol{\Gamma_0}}$	:	Percentage error obtained by the reconstruction of Γ_0
$\mathbf{C}^{\lvert\mathbf{d}\rvert}$	:	Absolute difference between the center coordinates of the exact and reconstructed Γ_0
$\mathbf{j_L}$	:	Iteration number for location reconstruction of Γ_0
$\mathbf{j_S}$	:	Iteration number for shape reconstruction of Γ_0
$\boldsymbol{\lambda}^{(0)}$	:	Initially guessed conductivity function
$\boldsymbol{\Gamma}^{(0)}$	:	Initally guessed boundary
$\boldsymbol{\Gamma}^{a}$	:	Apple-shaped contour
$\boldsymbol{\Gamma}^{c}$	:	Circle-shaped contour
$\boldsymbol{\Gamma}^{e}$	:	Elliptic contour
$\boldsymbol{\Gamma}^{k}$	:	Kite-shaped contour
$\boldsymbol{\Gamma}^{p}$	:	Peanut-shaped contour
$\boldsymbol{\Gamma}^{s}$	:	Rounded square-shaped contour
$\boldsymbol{\Gamma}^{r}$	:	Rounded rectangular-shaped contour
$\boldsymbol{\Gamma}^{t}$	:	Rounded triangular-shaped contour
$\boldsymbol{C}(G)$	:	Normed space of real or complex-valued continuous functions defined on G
$\boldsymbol{C}^{0,\beta}(G)$	:	Normed space of real or complex-valued uniformly Hölder continuous functions defined on G with $0 < \beta \leq 1$, $\beta \in \mathbb{R}$
$\boldsymbol{C}^{1,\beta}(G)$	:	Normed space of real or complex-valued uniformly Hölder continuously differentiable functions defined on G with $0 < \beta \leq 1$, $\beta \in \mathbb{R}$
$\boldsymbol{L}^{p}(G)$	:	Set of functions whose p th power is integrable over G in the sense of Lebesgue
$\boldsymbol{H}^{1}(G)$	:	Sobolev space of all functions $f \in L^2(G)$ with the property that $f \circ z \in H^1[0,2\pi]$ for the boundary G parametrized in the form $z(t) = (z_1(t), z_2(t))$, $t \in [0,2\pi]$ where $(f \circ z)(t) := f(z(t))$.

INVERSE SCATTERING PROBLEMS FOR THE OBJECTS BURIED IN PENETRABLE CYLINDERS

SUMMARY

Inverse problem related to objects buried in cylindrically layered media is one of the interesting subject in inverse scattering theory not only from its mathematical and physical importance but also for its wide range of practical applications. The main aim of such an inverse problem is to recover the geometrical and/or physical properties of the object buried in a cylindrical region from the scattered field measurements performed on a certain domain outside the objects. Although the problem has many important application areas such as medical imaging, non-destructive testing etc., there are a few studies related to subject in the literature and it is open to new contributions. Within this framework in this study numerical solutions of a group of inverse electromagnetic scattering problems related to objects buried in arbitrarily shaped penetrable cylinders are presented. In principle solution of an inverse problem requires measured data, therefore for each problem considered in the thesis a corresponding direct problem is also solved in order to produce synthetic data. The formulations of both direct and inverse problems are based on systems of boundary integral equations which contain single- and double-layer potentials.

Three different inverse problems related to different configurations considered in the thesis are defined as follows:

i. Reconstruction of the inhomogeneous surface impedance of an arbitrarily shaped object (whose shape is known) buried in an arbitrarily shaped dielectric cylinder.
ii. Reconstruction of the location and shape of a perfect electric conductor (PEC) buried in an arbitrarily shaped dielectric cylinder.
iii. Reconstruction of the shape of a PEC object buried in an arbitrarily shaped cylinder having conductive boundary condition on its surface as well as the inhomogeneous conductivity function of this cylinder.

The first inverse problem investigated in the thesis is devoted to the impedance reconstructions of the obstacles buried in dielectric cylinders where both shapes of the scatterers and the wave numbers of the media are known. This problem has not been studied before in the open literature. However, in the thesis we combine our new algorithm for the reconstructions of the fields with a modification of a decomposition method to obtain the inhomogeneous impedance function varies on the buried obstacle. In the second problem location and shape reconstructions of PEC objects buried in dielectric cylinders are presented. Our inversion method which is based on Newton iterations contains a new algorithm for the location reconstructions and an application of the so-called hybrid method for the shape reconstructions.

In the final part we want to reconstruct the physical properties of penetrable cylinders. To this aim we first study on the inhomogeneous conductivity function reconstructions of the obstacles in free space. Then, in order to solve another new inverse problem whose aim is to reconstruct the shape of the buried perfect electric conductor and the value of the conductivity function varies on the boundary of the exterior cylinder

we employ the methods investigated in the thesis for shape and conductivity function reconstructions, simultaneously.

In the thesis, we choose boundary integral equation methods depending on potential approach to formulate and to solve direct and inverse problems. That is, the fields appear from the interaction of the scatterers with the time-harmonic plane wave are expressed by the integrals containing source (density) functions. From mathematical point of view, we reduce our problems for seeking solutions of the homogeneous Helmholtz equation under some physical constraints and theoretical assumptions according to the type of an investigated problem. Since any solution to the Helmholtz equation can be represented as a combination of potentials we employ layer potentials. Thus, to obtain systems of boundary integral equations for the unknown density functions we substitute considered potential representations of the fields to the boundary conditions of the corresponding problem under proper jump relations. Even integral equations derived in the direct problems are well-posed, we obtain ill-posed integral equations in the solution of the inverse problems and apply to them Tikhonov regularizations to find stable solutions of the desired density functions. Finally, density functions and related potentials allow us to compute the values of the scattered and total fields in every region. Along this line, general definitions of the problems, integral representations of the fields for the direct and inverse problems, the detailed explanations of the layer potentials, boundary integral operators and their numerical evaluations are also presented.

Last sections of each chapter is allocated to illustrate the simulation results and to discuss the experiences obtained from numerical implementations of the methods. In particular, different scenarios to observe and identify the behaviors of the proposed methods to the variations of the problem parameters are considered. Consequently, successful and interesting numerical results that show the applicability and the effectiveness of our solutions are obtained.

GEÇİRGEN SİLİNDİRLER İÇERİSİNE GÖMÜLÜ CİSİMLER İÇİN TERS SAÇILMA PROBLEMLERİ

ÖZET

Silindirik katmanlı ortamlara gömülü cisimlere ilişkin ters saçılma problemi matematiksel ve fiziksel açıdan önemli olmasının yanısıra geniş pratik uygulama alanının bulunması nedeniyle ters saçılma teorisinde ilgi çekici konulardan bir tanesidir. Bu türden bir ters problemin temel amacı cisimlerin dışarısındaki bir bölgede gerçekleştirilen saçılan alan ölçümlerinden silindirik bölge içerisine gömülü cismin geometrik ve/veya fiziksel özelliklerini belirlemektir. Bu problemin tıbbi görüntüleme, temassız muayene vb. önemli uygulama alanları olmasına karşın konuyla ilgili literatürde az sayıda çalışma bulunmakta ve konu yeni katkılara açıktır. Bu çerçevede, bu çalışmada keyfi şekle sahip geçirgen silindirler içerisine gömülü cisimlere ait bir grup elektromagnetik ters saçılma probleminin sayısal çözümleri sunulmaktadır. Prensip olarak bir ters problemin çözümü ölçüm verisi gerektirir. Bu nedenle tezde ele alınan her ters probleme ilişkin düz problem de sentetik veri üretmek için çözülmüştür. Düz ve ters problemlerin formülasyonu tek- ve çift-katman potansiyelleri içeren sınır integral denklem sistemlerine dayanmaktadır.

Tezde ilgilenilen farklı konfigurasyonlara sahip üç farklı ters problem aşağıda tanımlanmıştır:

i. Keyfi şekilli bir dielektrik silindir içerisine gömülü keyfi şekilli (şekli bilinen) bir cismin inhomojen yüzey empedansının belirlenmesi.
ii. Keyfi şekilli dielektrik bir silindir içerisine gömülü mükemmel iletkenin şeklinin ve lokasyonunun belirlenmesi.
iii. Yüzeyi üzerinde kondüktif sınır koşulu sağlanan keyfi şekilli bir silindir içerisine gömülü mükemmel iletken cismin şeklinin ve dış silindire ait inhomojen kondüktivite fonksiyonunun belirlenmesi.

Tezde incelenen ilk ters problem saçıcıların şekillerinin ve ortamların dalga sayılarının bilinmesi halinde dielektrik silindirler içerisine gömülü cisimlerin empedanslarının belirlenmesidir. Bu problem daha önceden açık literatürde incelenmemiştir. Oysa bu çalışmada, gömülü cisim üzerinde değişen inhomojen empedans fonksiyonunu elde edebilmek için; alanların bulunması amacıyla sunduğumuz yeni algoritma ile bir dekompozisyon metodunun modifikasyonu kombine edilerek kullanılmıştır.

İkinci problemde dielektrik silindirler içerisine gömülü mükemmel iletken cisimlerin lokasyon ve şekillerinin belirlenmesi sunulmuştur. Newton iterasyonları tabanlı tersini alma metodumuz, lokasyon bulunması için yeni bir algoritma ve hibrid olarak bilinen metodun bir uygulamasını içermektedir.

Son kısımda ise geçirgen silindirin fiziksel özelliklerinin bulunması hedeflenmiştir. Bu amaçla boş uzayda cisimlerin inhomojen kondüktivite fonksiyonlarının bulunması üzerine çalışılmıştır. Sonrasında, amacı gömülü mükemmel iletkenin şeklinin ve dış silindir üzerinde değişen kondüktivite fonksiyonunun değerinin bulunması olan bir başka yeni ters problemi çözebilmek için tezde incelenen şekil ve kondüktivite fonksiyonunu bulma metodları ardışık olarak kullanılmıştır.

Tezde, düz ve ters problemleri formüle etmek ve çözmek için potansiyel yaklaşımına dayanan sınır integral denklem metodları seçilmiştir. Öyle ki, zamana bağlı düzlem dalganın saçıcılar ile etkileşimi sonucu görülen alanlar, kaynak(yoğunluk) fonksiyonları içeren integraller ile ifade edilmiştir. Matematiksel açıdan problemler, homojen Helmholtz denkleminin incelenen problemin türüne bağlı olarak bazı fiziksel kısıtlamalar ve teorik varsayımlar altında çözümlerini aramaya indirgenmiştir. Helmholtz denkleminin herhangi bir çözümü potansiyellerin kombinasyonu türünden ifade edilebileceğinden katman potansiyelleri kullanılmıştır. Böylece bilinmeyen yoğunluk fonksiyonlarına ait sınır integral denklem sistemlerini elde etmek için uygun sıçrama koşulları altında alanlara ilişkin potansiyel gösterilimleri sınır koşullarında yerine konulmuştur. Her ne kadar düz problemlerde türetilen integral denklemler iyi-kurulmuş olsa da ters problemlerin çözümünde kötü-kurulmuş integral denklemler elde edilmiş ve istenilen yoğunluk fonksiyonlarının kararlı çözümlerini bulabilmek için kötü-kurulmuş bu denklemlere Tikhonov regülarizasyonu uygulanmıştır. Son olarak, yoğunluk fonksiyonları ve bunlara ilişkin potansiyeller bize her bölgede saçılan ve toplam alanları hesaplamayı olanaklı hale getirmiştir. Bu çizgide, tezin içersinde problemlerin genel tanımları, düz ve ters problemler için alanların integral gösterilimleri, katman potansiyellerin detaylı açıklamaları, sınır integral operatörleri ve onların sayısal olarak değerlendirmeleri de sunulmuştur.
Herbir bölümün son kısımları simülasyon sonuçlarını izah etmeye ve metodların nümerik olarak gerçeklenmesi sırasında elde edilen tecrübelerin tartışılmasına ayrılmıştır. Özellikle, önerilen metodların problem parametrelerinin değişimine göre davranışlarını gözlemlemek ve aydınlatmak için farklı senaryolar tasarlanmıştır. Netice olarak çözümlerimizin uygulanabilirlik ve etkinliğini gösteren başarılı ve ilgi çekici sonuçlar elde edilmiştir.

1. INTRODUCTION

More than two thousand years ago, Plato in his study entitled with the *Republic* book VII presented the allegory of the cave to illustrate the philosophical phenomenon about reconstructing the realities from the observations of shadows on a den wall, [1]. Keeping the same approach, that is finding causes from the knowledge of their effects constitutes the main idea which stays behind of solving inverse problems. Furthermore, it is known that small changes in the effects might result in large differences in the causes or the same effect might be obtained from more than one cause. Therefore, it is difficult or sometimes impossible to distinguish clearly or to find exactly actual reasons by observing effects. These are improperly or ill-posed characteristics of inverse problems. Hadamard [2] postulated three requirements to classify problems as well-posed in mathematical physics such that: a solution should exist, the solution should be unique and the solution should depend continuously on the data. In this context, it can be concluded that inverse problems are ill-posed in the sense of Hadamard and to solve them some additional techniques have to be used [1, 3–6].

Generally accepted view about the first mathematical investigation of inverse problems is the study of Abel's on a mechanical problem for finding the curve of an unknown path in 1826, [3]. However, invention of radar and sonar during the Second World War inspired researchers to focus on inverse scattering problems whose aims are not only to determine locations of the targets from the transmitter/receiver antennas but also to construct the images of them, [7]. This motivation induced the progress of developing new theoretical methods. Furthermore, the advent of powerful computers and high technologies made it possible to evaluate and process large volume of data for finding accurate solutions of practical inverse scattering problems in the areas of mine detection, medical imaging, non-destructive testing and geophysical explorations, [7–17].

Inverse scattering problems can roughly be divided into two classes as the inverse obstacle and inverse medium problems. In this thesis we restrict ourselves to the first type of problems.

For the solution of an inverse scattering problem one needs the scattered field data which can be obtained either experimentally or numerically. Indeed, the main objective of direct scattering problems in acoustic or electromagnetic theory is to find the scattered near-/far-field pattern when a penetrable or an impenetrable obstacle is illuminated by a single(multi) time-harmonic plane wave(s) at fixed or variable frequency, see Figure 1.1. Obviously, this scattered field data contains

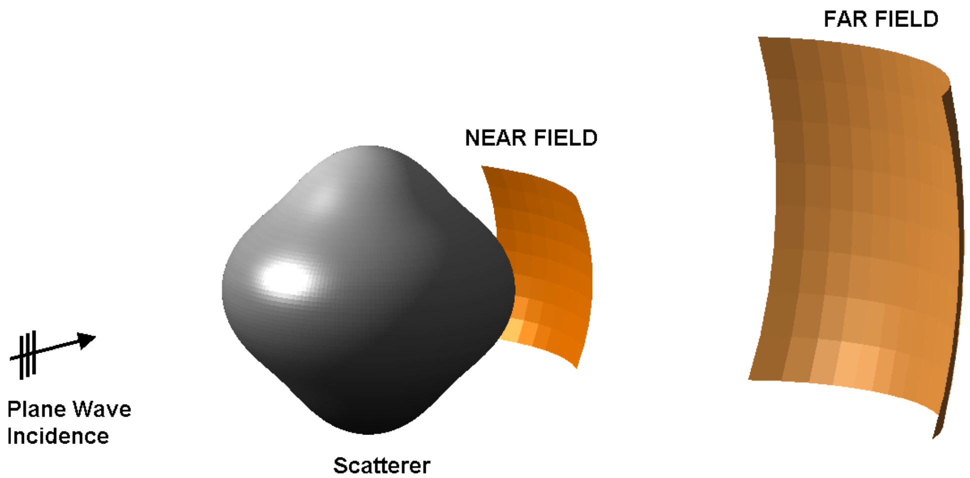

Figure 1.1: Geometry of the direct scattering problems

some information related to geometrical and physical properties of the obstacle under investigation and the identification of the desired parameters (location, shape, conductivity etc.) constitutes an important class in inverse scattering theory. Along this line, in the thesis we stay in the context of inverse electromagnetic scattering principles for two-dimensional geometries and focus on inverse problems related to impenetrable obstacles buried in penetrable arbitrarily shaped cylinders. Moreover in this study, proposed solutions are effective in the resonance region such that the diameters of the scatterers and the wavelength is of a comparable size. In this intermediate frequency range high frequency methods (physical, geometric optics) or low frequency methods (impedance tomography) do not yield valid approximations, [11, 12].

Two fundamental goals of solving inverse obstacle problems are to reconstruct geometrical and/or physical properties of penetrable/impenetrable objects from the knowledge of the scattered near-/far-field. For the solution of the mentioned problems large volume of studies, some of which will be recalled here, containing different type of methods were introduced in the open literature, [6, 98]. In order to discuss the published solution techniques we take a simple scattering problem. Let us consider an infinitely long and arbitrarily shaped perfectly conducting cylinder (PEC) which is modelled by a bounded domain $D \in \mathbb{R}^2$ located in a space of infinite extent. Then the Dirichlet condition is satisfied on its boundary Γ having a unit normal ν, see Figure 1.2. Furthermore assume that this cylinder is illuminated by a time-harmonic TM-polarized

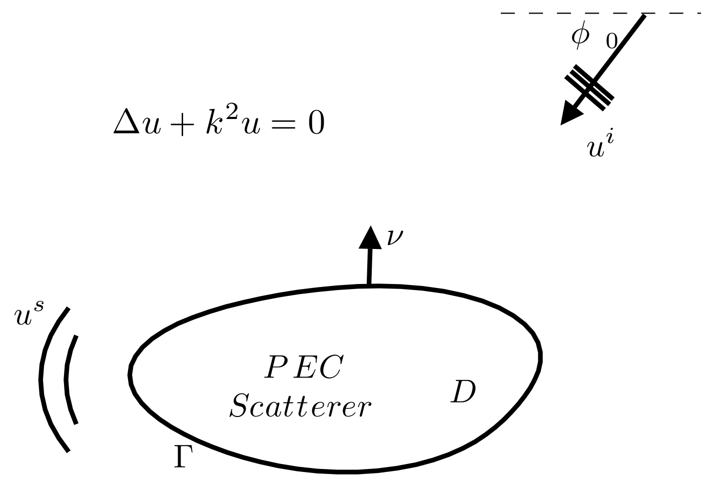

Figure 1.2: Geometry of a two-dimensional simple scattering problem

electromagnetic wave with an incidence angle ϕ_0, at a fixed frequency ω, excited in a simple medium having a wave number k, where the electric field vector $\boldsymbol{E}^i$ of the incident wave stays always parallel to the infinitely long dimension of the cylinder, that is,

$$\boldsymbol{E}^i = (0, 0, u^i), \quad u^i = e^{ik\boldsymbol{x}\cdot\boldsymbol{d}}, \quad \boldsymbol{x} = (x_1, x_2) \quad \text{and} \quad \boldsymbol{d} = (\cos\phi_0, \sin\phi_0). \tag{1.1}$$

Physically speaking the scattered field u^s appears from the interaction of the incident wave with the cylinder. The Sommerfeld radiation condition ensures that the scattered wave is outgoing. Additionally, another popular approach for the solution of inverse scattering problems is the usage of the far-field pattern u_∞, which can be obtained from the asymptotic behavior of the scattered wave. Now, the total field u exists in the background medium is given by the superposition of the incident and scattered fields $u = u^i + u^s$, that has to satisfy homogeneous Helmholtz equation in the exterior domain of the obstacle,

$$\triangle u + k^2 u = 0 \quad \text{in} \quad \mathbb{R}^2 \backslash \bar{D}, \tag{1.2}$$

and the Dirichlet condition on the boundary of the cylinder,

$$u = 0 \quad \text{on} \quad \Gamma. \tag{1.3}$$

The aim of the direct problem for this configuration is to find the far-field. However in this section our main concern is to mention the available methods for reconstructing the boundary Γ from the knowledge of the far-field. The inverse problem considered here is nonlinear due to the mathematical relation between the far-field and the shape of the cylinder and it is ill-posed since the determination of Γ does not depend continuously on the scattered field, [16]. To solve this inverse problem properly many different methods were introduced which are listed below. However, since we want to give a brief discussion about some techniques we do not claim to cover entire literature in the list.

▶ Iterative Methods:	▷ Newton-Kantorovich	[18,19]
	▷ Regularized Newton	[20–43]
	▷ Landweber iterations	[44,45]
▶ Decomposition Methods:	▷ Colton-Monk	[46–48]
	▷ Kirsch-Kress	[43,49–52]
	▷ Angell-Kleinmann-Roach	[53–55]
	▷ Hybrid Method	[56,61]
	▷ Point Source	[62–64]
▶ Probe and Sampling Methods:	▷ Linear Sampling	[65–68]
	▷ Factorization	[69,70]
	▷ Singular Sources	[15,64,71]
	▷ Probe Method	[72,73]
	▷ Enclosure Method	[74,75]
	▷ No-Response Test	[76–78]

In order to present the idea of the first group of methods [18,45], we define an operator $A : \Gamma \mapsto u_\infty$ which maps the boundary Γ of the scatterer D onto the far-field. Then the exact solution of the following ill-posed nonlinear operator equation,

$$A(\Gamma) = u_\infty, \tag{1.4}$$

gives the actual boundary Γ. To solve this nonlinear equation via iterative methods an initial guess Γ_0, with star-like parametrization

$$\Gamma_0 = \{z(t) := r(t)(\cos t, \sin t) : t \in [0, 2\pi)\} , \tag{1.5}$$

is chosen and the equation (1.4) is first linearized as,

$$A(z) + A'(z)\, h = u_\infty . \tag{1.6}$$

Then, due to the ill-posedness of the linearized equation some regularization technique for instance Tikhonov regularization is applied to (1.6) and the following equation

$$\alpha h + \left[A(z)'\right]^* A'(z)\, h = \left[A(z)'\right]^* \left[u_\infty - A(z)\right] , \tag{1.7}$$

is obtained where α is a positive number. The solution h is sufficiently small update function for the shape of the obstacle. This procedure is repeated iteratively until a suitable stopping criteria is fulfilled, see [16].

One can obtain successful results with a good initial guess using iterative methods. However, an accurate result of a forward solver for every iteration is needed. Furthermore, the convergence of regularized Newton iterations has not been completely settled although some work has been done, [32, 33].

Decomposition methods [46, 64], are optimization based techniques and their main idea is to split the equation given by (1.4) into linear ill-posed and nonlinear well-posed equations and after that to solve each of them, separately. In Kirsch-Kress method [43, 49–52] a closed boundary Γ_0 is considered inside the obstacle. Then the scattered field u^s, can be represented by a single-layer potential

$$u^s(\boldsymbol{x}) = \frac{i}{4} \int_{\Gamma_0} H_0^{(1)}(k\,|\boldsymbol{x} - \boldsymbol{y}|)\, \varphi(\boldsymbol{y})\, ds(\boldsymbol{y}) , \quad \boldsymbol{x} \neq \boldsymbol{y} , \quad \boldsymbol{x} \in \mathbb{R}^2 \backslash \bar{D} , \tag{1.8}$$

if k^2 is not a Dirichlet eigenvalue for the negative Laplacian in the interior of Γ_0 for an unknown continuous density(source) function φ, defined over the boundary Γ_0 and the Hankel function $H_0^{(1)}$ of the first kind and zero order, [43]. The far-field representation of the scattered field (1.8) can be obtained from the asymptotic behavior of the Hankel function. For the solution of the inverse problem in the case of a given far-field, one first has to solve the Fredholm-type integral equation of the first kind in order to compute the density function using a kind regularization technique. Then the approximate total field can be computed as

$$\widetilde{u}(\boldsymbol{x}) \;:=\; u^i(\boldsymbol{x}) \;+\; \frac{i}{4}\int_{\Gamma_0} H_0^{(1)}(k\,|\boldsymbol{x}-\boldsymbol{y}|)\;\widetilde{\varphi}(\boldsymbol{y})\,ds(\boldsymbol{y})\,, \qquad \boldsymbol{x}\in \mathbb{R}^2\backslash\bar{D}\,, \tag{1.9}$$

which should satisfy the Dirichlet boundary condition on Γ for the exact reconstruction. To this aim we introduce an operator G, which maps Γ into the values of the approximate total field $\widetilde{u}$, on Γ such that

$$G:\Gamma \mapsto \widetilde{u}|_{\Gamma}\,. \tag{1.10}$$

Then the inverse problem is reduced to the solution of the following optimization problem

$$G(\Gamma)=0\,, \tag{1.11}$$

which can be done in a least square sense by minimizing the defect $\|G(\Gamma)\|_{L^2(\Gamma)}$. Even though the decomposition methods yield good reconstructions they have some limitations of such as the boundary condition and also a priori information for choosing the boundary Γ_0 has to be known. However, in the decomposition methods there is no need of a forward solver as in the sense of iterative methods.

More recently, two inversion algorithms which are based on the modifications of Kirsch-Kress [56] and Kress-Rundell [36] methods have been introduced. In the first one called as *hybrid method* [56–61], the boundary Γ_0, is arbitrarily chosen under some regularity conditions and it is assumed to be an approximation of the unknown boundary on the contrary to the decomposition method where Γ_0 should be inside of unknown boundary. Moreover the unknown density function $\widetilde{\varphi}$ is also computed as in the decomposition methods. Then the following linearized equation

$$G(z)+G'(z)h=0 \tag{1.12}$$

is solved for the shape update function h. This allow us to update the initially guessed boundary Γ_0 and completes the first iteration. These two steps repeats iteratively for the updated shape until a desired stopping criteria is fulfilled. In another Newton-type method one solves a system of two nonlinear integral equations to find the update for the density and shape functions in each iteration step, [36–41].

The main idea of the sampling method which suggested by Kirsch and Colton [65–68] is to find an indicator function such that its value provides whether an arbitrarily tested space coordinate lies inside or outside of the object. In the application, a fine grid is considered which includes the object to be reconstructed and each point of this grid is checked to determine the shape of the obstacle. The most impressive property of sampling methods which is important from practical point of view is that without having any a priori information for the obstacle they can find shape of the scatterers. But for this, sampling methods requires knowledge of the far-field in all directions by multi-illuminations. On the other hand, iterative and decomposition methods work for single illumination.

After introducing some information on the shape reconstruction techniques, now we are in a position to discuss on the other class of inverse scattering problems whose aims are to construct some specific functions which are defined on the boundary of the obstacles. In electromagnetic theory, impedance boundary condition is used to model imperfectly conducting scatterers, perfectly conducting objects with a penetrable or absorbing boundary layer, or scatterers with a corrugated boundary, [82, 85, 108]. Indeed, the obstacle having impedance boundary condition on its surface is impenetrable for electromagnetic waves. Mathematically, this condition is defined as

$$u+\frac{\eta}{ik}\frac{\partial u}{\partial \boldsymbol{\nu}}=0, \quad \text{on}\,\Gamma. \tag{1.13}$$

The case $\eta \to 0$, reduces the impedance boundary condition to the Dirichlet boundary condition for sound-soft obstacles in acoustics or perfect electric conductors in electromagnetics.

Researchers also made progress on the solution of impedance reconstruction problems by introducing different techniques or extending some methods mentioned above, see [57, 79–85]. Along this line, in [79–81] theoretical investigations of 3-D obstacles with impedance boundary condition are given for acoustic theory where in [81] electromagnetic case is also included.

The study [80] is devoted to show the applicability of the Kirsch-Kress and Colton-Monk decomposition methods for the reconstruction of impedance functions. For the theoretical implementation of the Kirsch-Kress method in [80] a multi-illumination case is assumed. Furthermore, the Fréchet differentiability of the boundary to far-field operator is given in [81] by extending the approach suggested by

Kress and Päivärinta for perfect electric conductors to the obstacles with impedance boundary condition.

In the paper [82], in the spirit of the Kirsch-Kress decomposition method a new technique is introduced for recovering the inhomogeneous impedance function defined over the boundary of an obstacle in two dimensions. For the reconstruction algorithm, the scattered field is represented via single-layer potential as in (1.8). However, in this method the boundary integral is written over the known boundary of the impedance cylinder Γ, instead of defining an auxiliary closed curve. Then the approximate density function $\widetilde{\varphi}$, is found via Tikhonov regularization. By using the value of the density function which is reconstructed from the far-field now one can compute the total field

$$\widetilde{u}(\boldsymbol{x}) = u^i(\boldsymbol{x}) + \int_\Gamma \Phi(\boldsymbol{x},\boldsymbol{y})\, \widetilde{\varphi}(\boldsymbol{y})\, ds(\boldsymbol{y}) \,, \qquad \boldsymbol{x} \in \Gamma, \tag{1.14}$$

and the normal derivative of the total field

$$\frac{\partial \widetilde{u}}{\partial \boldsymbol{\nu}}(\boldsymbol{x}) = \frac{\partial u^i}{\partial \boldsymbol{\nu}}(\boldsymbol{x}) + \int_\Gamma \frac{\partial \Phi(\boldsymbol{x},\boldsymbol{y})}{\partial \boldsymbol{\nu}(\boldsymbol{x})}\, \widetilde{\varphi}(\boldsymbol{y})\, ds(\boldsymbol{y}) - \frac{1}{2}\widetilde{\varphi}(\boldsymbol{x}) \,, \qquad \boldsymbol{x} \in \Gamma, \tag{1.15}$$

on the boundary of the obstacle via jump relations [43]. Here $\Phi(\boldsymbol{x},\boldsymbol{y})$ is fundamental solution of the Helmholtz equation in two dimensions in terms of the Hankel function $H_0^{(1)}$ of the first kind and zero order. Finally, the function η can be found from the equation (1.13). However, since this solution will be sensitive to errors in the normal derivative of u in the vicinity of zero, in order to obtain a more stable solution, the unknown function η is expressed in terms of some proper basis functions with corresponding unknown coefficients. Then by substituting the approximation of η to the equation (1.13) the resultant equation can be evaluated in the least squares sense.

Moreover, efforts have been given both for the shape and impedance reconstructions of 2-D obstacles in acoustics, [57, 83, 84]. For this the hybrid method just mentioned above is applied in [57]. Specifically in [84], to reconstruct the shape and impedance of 2-D obstacles from multi-illuminations a level set algorithm is combined with boundary integral equations in acoustic theory. Furthermore, it has been shown in [83] that the knowledge of the scattered fields corresponding to three incident waves can be used for the determination of the shape and the impedance via integral equation methods.

Up to this point the obstacles that we considered were all impenetrable scatterers. However, from now on we mention about the inverse scattering problems for the penetrable objects. To this aim, we consider an arbitrarily shaped penetrable obstacle and define total fields u_1 and u_0 in exterior and interior domains, respectively. The general form of the condition defined on the surface of penetrable obstacles is called conductive boundary condition (CBC) such that,

$$\left.\begin{aligned} & u_0 = u_1 \\ & \frac{\partial u_1}{\partial \boldsymbol{\nu}} - \frac{\partial u_0}{\partial \boldsymbol{\nu}} = \lambda u_1 \end{aligned}\right. \quad \text{on} \quad \Gamma . \tag{1.16}$$

Here the parameter λ is so-called *conductivity function*, see [94]. From physical point of view the conductive boundary condition can occur when a dielectric obstacle is covered by an infinitely thin non-ideal type conductor with the excitation of electrical current on the surface. In this context, the derivation of the CBC for time-harmonic electromagnetic waves is described in [90]. Uniqueness theorems for the inverse obstacle scattering with CBC are proven for time harmonic electromagnetic and acoustic waves by Hettlich in 1996 [91] and by Gerlach and Kress in 1996 [92], respectively. And also for the latter case, the properties of the far-field operator is investigated in [93]. In the study [94], the method suggested by Akduman and Kress was extended for the reconstructions of the conductivity functions of the obstacles in free space and then applied for the obstacles buried in penetrable cylinders [95] by Yaman, in 2008. On the other hand, in the case of $\lambda \to 0$ the condition (1.16) is reduced to transmission conditions which are also called dielectric boundary conditions in electromagnetic theory. Indeed, transmission conditions ensure the continuity of the total fields and their normal derivatives across the surface/boundary of the penetrable obstacles.

In the thesis, we consider an arbitrarily shaped impenetrable obstacle which is buried in an arbitrarily shaped penetrable cylinder and both are located in an infinite homogeneous background medium in two-dimensions. That is on the boundary of the buried obstacle Γ_0, the Dirichlet or impedance boundary condition is posed and on the boundary of the exterior cylinder Γ_1, conductive or transmission boundary condition has to be satified according to the aim of the problem under investigation, see Figure 1.3. As another initial condition, we consider sufficiently smooth boundaries such that the unit normal vectors $\boldsymbol{\nu}_0$ and $\boldsymbol{\nu}_1$ can be defined at any point of Γ_0 and Γ_1, respectively. Furthermore we assume that any medium in the problem configuration is simple and scatterers are illuminated by a time-harmonic electromagnetic wave excited by a source which is sufficiently far away and the waves have a fixed oscillation frequency. Following the same analogy as illustrated in previous pages related to TM-polarized electromagnetic waves, the incoming wave has the representation given in (1.1) and the scattered field that occurs in the domain D_1 has to satisfy Sommerfeld radiation condition for the wave number k_1. In this configuration, the homogeneous Helmholtz equation should be satisfied in each medium

$$\triangle u_1 + k_1^2 u_1 = 0 \quad \text{in } D_1 \qquad \text{and} \qquad \triangle u_0 + k_0^2 u_0 = 0 \quad \text{in } D_0\,, \tag{1.17}$$

for the corresponding wave numbers, where the solutions of the above differential equations provide the exterior u_1 and the interior u_0 total fields, respectively.

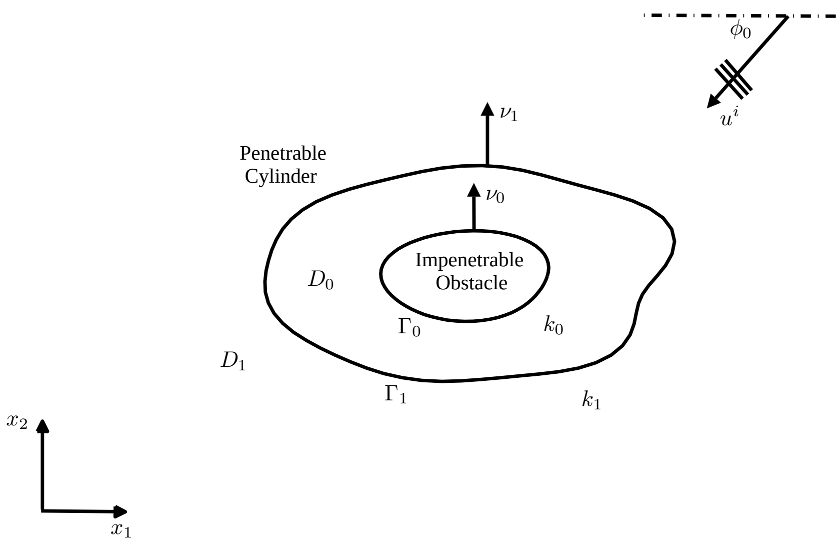

Figure 1.3: Geometry of the problems in the thesis

For the given problem statement we studied on the inverse problems for the objects buried in penetrable cylinders whose aims are,

- to reconstruct the inhomogeneous impedance function defined on the buried obstacle,
- to find the location and the shape of the buried obstacle having the Dirichlet condition satisfy on its boundary,
- to find the shape of the perfectly conducting buried obstacle and the inhomogeneous conductivity function varies on the penetrable cylinder,

from the knowledge of the scattered field in principle, for one plane wave incidence.

In order to achieve any of these final goals we first need to reconstruct the interior total field from the knowledge of the near- or far-field data. For this we propose a new algorithm based on the potential approach [43, 44, 98] in the thesis. In this method, the fields exist in any domain in the whole space can be represented via boundary integrals containing source (density) functions and the corresponding fundamental solution of the Helmholtz equation in two dimensions. Then the problem is reduced to the reconstruction of unknown density functions. For such geometry as given by the Figure 1.3 we locate two density functions on Γ_1 and one density function on Γ_0, see [85, 88, 89, 95, 98].

$$u_1(\boldsymbol{x}) = e^{ik_1\boldsymbol{x}\cdot\boldsymbol{d}} + \int_{\Gamma_1} \Phi_1(\boldsymbol{x},\boldsymbol{y})\,\varphi(\boldsymbol{y})\,ds(\boldsymbol{y}), \quad \boldsymbol{x} \in D_1, \tag{1.18}$$

$$u_0(\boldsymbol{x}) = \int_{\Gamma_1} \Phi_0(\boldsymbol{x},\boldsymbol{x})\,\psi(\boldsymbol{y})\,ds(\boldsymbol{y}) + \int_{\Gamma_0} \Phi_0(\boldsymbol{x},\boldsymbol{y})\chi(\boldsymbol{y})\,ds(\boldsymbol{y}), \quad \boldsymbol{x} \in D_0. \tag{1.19}$$

One of the densities which stays over the penetrable layer is reconstructed from the solution of the first kind integral equation via Tikhonov regularization. The values of the other two unknown densities are calculated by applying second Tikhonov regularization to the equations obtained from transmission or conductive boundary conditions on Γ_1. Once all the density functions are known one can compute the total fields in every region. This two-step algorithm is one of the contribution of the thesis.
Then according to the aim of the considered problem we extend some of chosen methods described in the previous pages to the buried cases. In this scope, as a first investigation we define a new problem and extend Akduman-Kress method [82] for the impedance reconstructions of obstacles buried in arbitrarily shaped dielectric cylinders. This model corresponds to applications in biomedical imaging, nondestructive testing and geophysical explorations. In biomedical applications, for example, the bone of an arm can be modeled in terms of an inhomogeneous impedance boundary condition while the muscular structure over it can be considered as a lossy dielectric layer. In nondestructive evaluation of the coating on a conducting wire, the coating can be characterized as an arbitrarily shaped lossy dielectric layer and the conducting wire is modeled by an inhomogeneous surface impedance [85].
In the second problem, we concern with the location and shape reconstructions of perfectly conducting obstacles buried in dielectric cylinders. Our integral equation based Newton method consists of a new algorithm for the solution of location

reconstruction problem and the extension of the idea introduced in [56] by employing the strategy given in [85, 88], iteratively. The paper [56] is devoted to the solution of the shape reconstruction problem of sound-soft obstacles in free space and the study [85] is focused on the impedance reconstructions of the objects buried in dielectric cylinders for given shapes of the scatterers. Since the algorithm presented in [56] yields satisfactory results, it is applied to shape reconstructions of sound-hard obstacles [58], and three-dimensional sound-soft scatterers [59]. Furthermore the behavior of the method is analysed in [61] by using higher order terms in the Taylor series. However, we should point out that in [56, 58, 59, 61] all the scatterers stay in free-space and the more realistic case as the problem stated in the thesis for buried obstacles with the method given in [56] has not been investigated before. On the other hand, the same and similar problems have already studied with different types of methods. For instance, the papers [86, 87] deal with the same location and shape reconstruction problem using multi-illumination and frequency data, respectively. In [86], a method is proposed depending on the algorithm for recovering conductivity of a penetrable object which uses high conductivity fact and in [87], Newton-Kantorovich and modified gradient methods are applied. However, our method is satisfactorily flexible and yields reasonable results with single illumination at fixed frequency even for the limited aperture case with noisy data.

As a last investigation of the thesis, we propose another new problem which deals with the shape reconstructions of perfectly conducting buried obstacles and the conductivity functions defined on the penetrable cylinders. The idea of solving such a problem is to combine the methods introduced for shape [56] and conductivity function reconstructions [94] which is also an original study. However, due to the complexity and highly ill-posedness of the problem this study still needs some improvements for obtaining stable results.

The plan of the thesis is as follows. In chapter 2, we define the basics and fundamental properties of the potential approach and boundary integral operators as well as their numerical evaluations. Furthermore the problems under investigation and the tools for the solutions of direct and inverse problems are also stated in the general formulation chapter. Then we continue with the first problem for the impedance reconstructions of buried obstacles, in chapter 3. The aim of the problem mentioned in chapter 4 is to find the location and the shape of the perfectly conducting objects buried in dielectric cylinders. Chapter 5 starts with the conductivity function reconstruction problem for arbitrarily shaped objects placed in unbounded homogeneous background mediums. Afterwards a new problem deals with recovering of a real valued conductivity function defined over the surface Γ_1 see Figure 1.3 and the shape of a perfectly conducting obstacle is introduced. Numerical results are clearly illustrated and corresponding conclusions are provided at the end of each chapter. Finally, general conclusions for the whole study are given in Chapter 6.

We note, that a time factor $e^{-i\omega t}$ is assumed and omitted throughout the thesis and bold characters are used to indicate vector variables.

2. GENERAL FORMULATION

In this chapter the problems investigated in the thesis and the approaches used for their numerical solutions are presented in details. The main aim of the problems is to determine the unknown physical and/or geometrical properties of the buried scatterer(s) from measured scattered field data. In this direction we consider three different type of problems which will be proposed in the following sections. For the numerical solution of the problems an integral equation based method is chosen. Therefore the scattered and the total fields are represented as superpositions of integrals defined on the boundaries of the scatterers depending on several *potential approaches*. The details of the potential approach will also be discussed in this chapter.

It should be noted that our investigations are valid in the *resonance region* [43], that is if we define the typical dimension of the object by a and the wave number by k, then the resonance region is the frequency region where the condition $ka \approx 1$ is satisfied. Therefore we assume that diffraction mechanism which can be seen in high frequency regions ($ka >> 1$) does not effect our solutions.

2.1 Statements of the Problems

We considered arbitrarily shaped infinitely long cylindrical objects that are buried in arbitrarily shaped cylinders, see Figure 2.1. In this configuration a domain $D_0 \subset \mathbb{R}^2$ is bounded by analytical curves Γ_0 and Γ_1, and connected to the unbounded domain D_1 via Γ_1 where $\Gamma_0 \cap \Gamma_1 = \emptyset$. The domain D_0 and D_1 are simple dielectric materials with parameters, $\left(\varepsilon_j\,,\; \mu_j\,,\; \sigma_j\right)\; j = 0,1$. We further assume that the materials have the same physical magnetic properties, i.e. $\mu_0 = \mu_1$. We shall denote the unit normal to Γ_0 directed into the interior of D_0 by $\boldsymbol{\nu}_0$ and the unit normal to Γ_1 directed into the exterior of D_0 by $\boldsymbol{\nu}_1$.

We define the three following different direct and inverse scattering problems with the geometry given in Figure 2.1 by changing the boundary conditions on the surfaces of the scatterers.

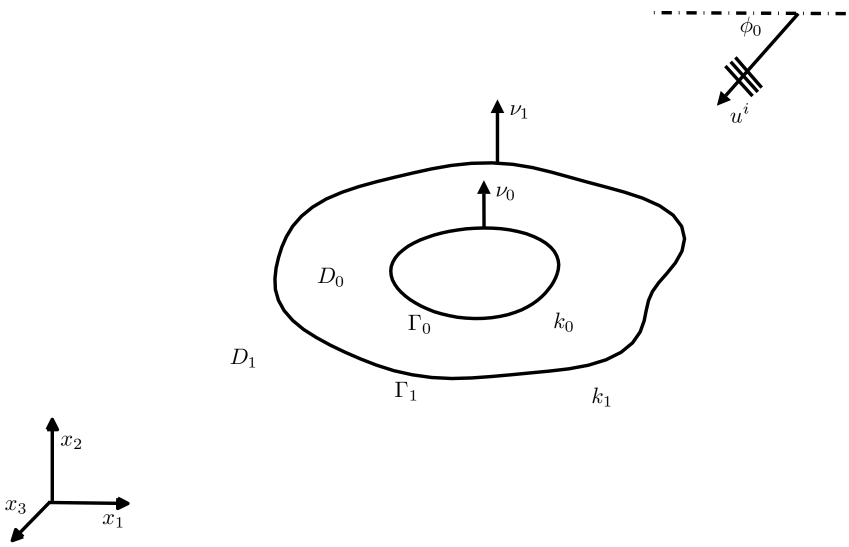

Figure 2.1: General geometry of the problems

i. In the first problem we consider transmission boundary condition on Γ_1 and impedance boundary condition on Γ_0.
ii. The second problem is defined when transmission boundary condition holds on Γ_1 and the Dirichlet boundary condition on Γ_0.
iii. As a third problem we consider conductive boundary condition on Γ_1 and the Dirichlet boundary condition on Γ_0.

In all problems, the scatterers are illuminated by a time-harmonic TM-polarized electromagnetic wave excited in D_1 having a wave number k_1 with a fixed radial frequency ω. The electric field vector of the incident wave is always parallel to the x_3-axis, that is,

$$\boldsymbol{E}^i(\boldsymbol{x}) = (0,0,u^i(\boldsymbol{x})), \quad u^i(\boldsymbol{x}) = e^{ik_1\boldsymbol{x}\cdot\boldsymbol{d}}, \tag{2.1}$$

in which

$$\boldsymbol{x} = x_1\boldsymbol{e}_1 + x_2\boldsymbol{e}_2\,, \quad \boldsymbol{d} = \cos\phi_0\boldsymbol{e}_1 + \sin\phi_0\boldsymbol{e}_2\,. \tag{2.2}$$

where $\boldsymbol{e}_1, \boldsymbol{e}_2$ are the unit vectors and $\boldsymbol{x}$ is the location vector while $\boldsymbol{d}$ denotes the propagation direction with incidence angle ϕ_0. Due to the symmetry and homogeneity along the x_3-axis the total electric field vector will be polarized both inside and outside of the cylinder parallel to the x_3-axis where we denote the total electric field in the bounded domain D_0 by $\boldsymbol{E}_0 = (0,0,u_0)$ and in the unbounded domain D_1 by $\boldsymbol{E}_1 = (0,0,u_1)$. Then the problem is reduced to a scalar one in terms of total fields that have to satisfy Helmholtz equations

$$\triangle u_j + k_j^2 u_j = 0 \quad \text{in } D_j, \quad j = \{0,1\}, \tag{2.3}$$

with the wave numbers

$$k_j = \omega\sqrt{\mu_j\left(\varepsilon_j + i\,\sigma_j/\omega\right)}, \tag{2.4}$$

given in terms of the dielectric permittivity ε_j, the magnetic permeability μ_j, and the conductivity σ_j of the medium D_j. The sign of the square root is chosen such that,

$$\mathrm{Re}\left\{k_j\right\} > 0 \quad \text{and} \quad \mathrm{Im}\left\{k_0\right\} \geq 0, \tag{2.5}$$

for all problems in this study.

The external total field u_1 can be decomposed as $u_1 = u^i + u^s$ into the incident field u^i given in (2.1) and the scattered field u^s that has to obey the Sommerfeld radiation condition

$$\lim_{r\to\infty} \sqrt{r}\left(\frac{\partial u^s}{\partial r} - ik_1 u^s\right) = 0, \quad r = |\boldsymbol{x}| = \sqrt{x_1^2 + x_2^2}\,, \tag{2.6}$$

uniformly for all directions. The Sommerfeld radiation condition (2.6) guarantees an asymptotic behavior of the scattered wave in the form of an outgoing wave

$$u^s(\boldsymbol{x}) = \frac{e^{ik_1|\boldsymbol{x}|}}{\sqrt{|\boldsymbol{x}|}}\left\{u_\infty\left(\frac{\boldsymbol{x}}{|\boldsymbol{x}|}\right) + O\left(\frac{1}{|\boldsymbol{x}|}\right)\right\}, \quad |\boldsymbol{x}| \to \infty, \tag{2.7}$$

uniformly for all directions with the amplitude factor u_∞ known as the far-field pattern and defined on the unit circle Ω.

In the thesis aims of the direct problems are to obtain the near- or far-field pattern. For the inverse problems from the knowledge of one these fields we consider:

i. to determine the impedance function defined over Γ_0,
ii. to reconstruct the location and shape of a PEC scatterer buried in a dielectric cylinder,
iii. to determine the conductivity function defined over Γ_1 and the shape of the PEC scatterer buried in Γ_1,

under corresponding boundary conditions, via potential approaches.

2.2 Potential Approach

We choose different potential approaches for the solutions of direct and inverse problems. Physically, single- and double-layer potentials correspond to a layer of monopoles and dipoles, respectively. Furthermore, any solution to the Helmholtz equation can be represented as a combination of the layer potentials in terms of the boundary values and the normal derivatives on the boundary [43].

In order to define layer potentials, let Γ_j and Γ_ℓ be closed bounded curves and f be a given integrable function. Then the integrals

$$u_{j\ell,m}(\boldsymbol{x}) := \int_{\Gamma_j} f(\boldsymbol{y})\,\Phi_m(\boldsymbol{x},\boldsymbol{y})\,ds(\boldsymbol{y})\,, \qquad \boldsymbol{x} \in \Gamma_\ell\,, \quad x \notin \Gamma_j\,, \quad j,\ell,m = \{0,1\}\,, \tag{2.8}$$

and

$$\upsilon_{j\ell,m}(\boldsymbol{x}) := \int_{\Gamma_j} f(\boldsymbol{y})\,\frac{\partial \Phi_m(\boldsymbol{x},\boldsymbol{y})}{\partial \nu_j(\boldsymbol{y})}\,ds(\boldsymbol{y})\,, \quad \boldsymbol{x} \in \Gamma_\ell\,, \quad x \notin \Gamma_j\,, \quad j,\ell,m = \{0,1\}\,. \tag{2.9}$$

are called, single- and double-layer potentials with density f, respectively. Here, $\Phi_m(\boldsymbol{x},\boldsymbol{y})$ is the fundamental solution to the two-dimensional homogeneous Helmholtz equation, with a wave number k_m in terms of Hankel function $H_0^{(1)}$ of the first kind and zero order, defined as

$$\Phi_m(\boldsymbol{x},\boldsymbol{y}) := \frac{i}{4} H_0^{(1)}(k_m\,|\boldsymbol{x}-\boldsymbol{y}|)\,, \qquad \boldsymbol{x} \neq \boldsymbol{y}\,, \qquad m = \{0,1\}\,. \tag{2.10}$$

The behavior of the layer potentials at the boundary $j = \ell = \{0,1\}$ is described by regularity and jump relations given in [43, 98]. These equations for single-layer potentials for $m = \{0,1\}$ at the boundary curve are,

$$u_{\ell\ell,m}(\boldsymbol{x}) = \int_{\Gamma_\ell} f(\boldsymbol{y})\,\Phi_m(\boldsymbol{x},\boldsymbol{y})\,ds(\boldsymbol{y})\,, \qquad \boldsymbol{x} \in \Gamma_\ell\,, \tag{2.11}$$

$$\frac{\partial u^{\pm}_{\ell\ell,m}}{\partial \boldsymbol{\nu}_\ell}(\boldsymbol{x}) = \int_{\Gamma_\ell} f(\boldsymbol{y})\,\frac{\partial \Phi_m(\boldsymbol{x},\boldsymbol{y})}{\partial \boldsymbol{\nu}_\ell(\boldsymbol{x})}\,ds(\boldsymbol{y}) \mp \frac{1}{2} f(\boldsymbol{x})\,, \qquad \boldsymbol{x} \in \Gamma_\ell\,, \tag{2.12}$$

and for double-layer potentials,

$$\upsilon^{\pm}_{\ell\ell,m}(\boldsymbol{x}) = \int_{\Gamma_\ell} f(\boldsymbol{y})\,\frac{\partial \Phi_m(\boldsymbol{x},\boldsymbol{y})}{\partial \boldsymbol{\nu}_\ell(\boldsymbol{y})}\,ds(\boldsymbol{y}) \pm \frac{1}{2} f(\boldsymbol{x})\,, \qquad \boldsymbol{x} \in \Gamma_\ell\,, \tag{2.13}$$

$$\frac{\partial \upsilon_{\ell\ell,m}}{\partial \boldsymbol{\nu}_\ell}(\boldsymbol{x}) = \frac{\partial}{\partial \boldsymbol{\nu}_\ell(\boldsymbol{x})} \int_{\Gamma_\ell} \frac{\partial \Phi_m(\boldsymbol{x},\boldsymbol{y}\,)}{\partial \boldsymbol{\nu}_\ell(\boldsymbol{y}\,)}\,f(\boldsymbol{y})\,ds(\boldsymbol{y})\,, \qquad \boldsymbol{x} \in \Gamma_\ell\,. \tag{2.14}$$

We shall distinguish the superscripts $'+'$ and $'-'$ the limits obtained by approaching the boundary Γ_ℓ from outside or inside, respectively, that is

$$\upsilon^{+}_{\ell\ell,m}(\boldsymbol{x}) = \lim_{\substack{\boldsymbol{y} \to \boldsymbol{x} \\ \boldsymbol{y} \in \mathbb{R}^2 \setminus \overline{\Gamma}_\ell}} \upsilon_{\ell\ell,m}(\boldsymbol{y})\,, \qquad \upsilon^{-}_{\ell\ell,m}(\boldsymbol{x}) = \lim_{\substack{\boldsymbol{y} \to \boldsymbol{x} \\ \boldsymbol{y} \in \overline{\Gamma}_\ell}} \upsilon_{\ell\ell,m}(\boldsymbol{y})\,, \qquad \boldsymbol{x} \in \Gamma_\ell\,.$$

Here, the line which stays over the Γ_ℓ indicates the closure of the interior domain bounded by Γ_ℓ.

2.3 Boundary Integral Operators

We use different combinations of the layer potentials for the solutions of direct and inverse problems in order to avoid *inverse crimes*. According to these combinations different types of integral equations are obtained. To write the mentioned equations in compact forms throughout the thesis we introduce the boundary integral operators such as the single- and double-layer operators

$$(S_{j\ell,m}f)(\boldsymbol{x}) := 2\int_{\Gamma_j} \Phi_m(\boldsymbol{x},\boldsymbol{y})\, f(\boldsymbol{y})\, ds(\boldsymbol{y}), \qquad \boldsymbol{x}\in\Gamma_\ell, \tag{2.15}$$

$$(K_{j\ell,m}f)(\boldsymbol{x}) := 2\int_{\Gamma_j} \frac{\partial\Phi_m(\boldsymbol{x},\boldsymbol{y})}{\partial\boldsymbol{\nu}_j(\boldsymbol{y})} f(\boldsymbol{y})\, ds(\boldsymbol{y}), \quad \boldsymbol{x}\in\Gamma_\ell, \tag{2.16}$$

and the corresponding normal derivative operators

$$(K'_{j\ell,m}f)(\boldsymbol{x}) := 2\int_{\Gamma_j} \frac{\partial\Phi_m(\boldsymbol{x},\boldsymbol{y})}{\partial\boldsymbol{\nu}_\ell(\boldsymbol{x})} f(\boldsymbol{y})\, ds(\boldsymbol{y}), \quad \boldsymbol{x}\in\Gamma_\ell, \tag{2.17}$$

$$(T_{j\ell,m}f)(\boldsymbol{x}) := 2\frac{\partial}{\partial\boldsymbol{\nu}_\ell(\boldsymbol{x})}\int_{\Gamma_j} \frac{\partial\Phi_m(\boldsymbol{x},\boldsymbol{y})}{\partial\boldsymbol{\nu}_j(\boldsymbol{y})} f(\boldsymbol{y})\, ds(\boldsymbol{y}), \quad \boldsymbol{x}\in\Gamma_\ell, \tag{2.18}$$

for $j,\ell,m=\{0,1\}$. Since the operators $S_{j\ell,m}, K'_{j\ell,m}, K_{j\ell,m}, T_{j\ell,m}$ are defined on closed curves Γ_j, $j=\{0,1\}$ it is possible to transform them to $[0,2\pi]$ type integral operators with 2π-periodic parametrization. We note that the parametric representations of the curves which are in the form of $r(t)(\cos t,\sin t)$, $t\in[0,2\pi]$ such as circle, apple shaped, rounded triangular etc. are called starlike [56], see Table 1.

Using parametrized representations of the integrals we solve the system of integral equations by the Nyström method which guarantees the exponential convergence for analytic boundaries and right hand sides. In this direction we assume that the boundary curves are parametrized in the form

$$\Gamma_j = \left\{\boldsymbol{z}_j(t) = \left(z_{j1}(t), z_{j2}(t)\right) : t\in[0,2\pi]\right\}, \quad \boldsymbol{z}_j \neq 0, \quad j=0,1, \tag{2.19}$$

where z_{j1} and z_{j2} are 2π –periodic and analytic functions having star-like form

$$z_{j1} = r_j(t)\cos t \quad \text{and} \quad z_{j2} = r_j(t)\sin t, \quad t\in[0,2\pi], \tag{2.20}$$

satisfying $r_j \neq 0$. The normal vectors are given by

$$\boldsymbol{\nu}_j(t) = \frac{1}{|\boldsymbol{z}'_j(t)|}\,[\boldsymbol{z}'_j(t)]^\perp, \quad t\in[0,2\pi], \quad j=0,1. \tag{2.21}$$

Here z_j' is the derivative of z_j and for any vector $z_j = (z_{j1}, z_{j2})$, the vector $z_j^\perp$ is obtained as $z_j^\perp := (z_{j2}, -z_{j1})$ by rotating a counter-clockwise by 90 degrees. Along this line the parametrized operators can be defined as

$$\widetilde{S}_{j\ell,m}, \widetilde{K}'_{j\ell,m}, \widetilde{K}_{j\ell,m}, \widetilde{T}_{j\ell,m} \,:\, C[0,2\pi] \to C[0,2\pi]\,, \qquad j,\ell,m = \{0,1\}\,.$$

The density function f which stays over the boundary Γ_j is given in the parametrized form as $\tilde{f}(t)$, $t \in [0,2\pi]$. For the operators $\widetilde{S}_{j\ell,m}$ and $\widetilde{K}'_{j\ell,m}$ we define the relation $\tilde{f} = |z_j'|\, f \circ z_j$ and for the operators $\widetilde{K}_{j\ell,m}$ and $\widetilde{T}_{j\ell,m}$, $\tilde{f} = f \circ z_j$ are used. This notation states that the parametrized density function has values at the points which belong to the boundary under the same parametrization.

In this direction for $\{t,\tau\} \in [0,2\pi]$ now we want to introduce the parametrized single-layer operator,

$$(\widetilde{S}_{j\ell,m}\tilde{f})(t) := \frac{i}{2}\int_0^{2\pi} H_0^{(1)}(k_m\left|z_\ell(t) - z_j(\tau)\right|)\,\tilde{f}(\tau)\,d\tau, \tag{2.22}$$

and the parametrized normal derivative of the single-layer operator,

$$(\widetilde{K}'_{j\ell,m}\tilde{f})(t) := \frac{ik_m}{2}\int_0^{2\pi} \frac{\left[z_\ell'(t)\right]^\perp \cdot\, \left[z_\ell(t) - z_j(\tau)\right]}{|z_\ell'(t)|\left|z_\ell(t) - z_j(\tau)\right|}\, H_0^{(1)\prime}(k_m\left|z_\ell(t) - z_j(\tau)\right|)\,\tilde{f}(\tau)\,d\tau. \tag{2.23}$$

The parametrized double-layer operator and it's normal derivative operator (see [85] and [94]) for $\tilde{f} = f \circ z_j$ are given via

$$(\widetilde{K}_{j\ell,m}\tilde{f})(t) := \frac{ik_m}{2}\int_0^{2\pi} \frac{\left[z_j'(\tau)\right]^\perp \cdot\, \left[z_j(\tau) - z_\ell(t)\right]}{\left|z_\ell(t) - z_j(\tau)\right|}\, H_0^{(1)\prime}(k_m\left|z_\ell(t) - z_j(\tau)\right|)\,\tilde{f}(\tau)d\tau, \tag{2.24}$$

$$\begin{aligned}(\widetilde{T}_{j\ell,m}\tilde{f})(t) :=& \int_0^{2\pi} U_{j\ell,m}(t,\tau)\, H_0^{(1)\prime}(k_m|z_\ell(t) - z_j(\tau)|)\tilde{f}(\tau)d\tau \\ &+ \int_0^{2\pi} V_{j\ell,m}(t,\tau)\left\{k_m H_0^{(1)\prime\prime}(k_m|z_\ell(t) - z_j(\tau)|) - \frac{H_0^{(1)\prime}(k_m|z_\ell(t) - z_j(\tau)|)}{|z_\ell(t) - z_j(\tau)|}\right\}\tilde{f}(\tau)d\tau,\end{aligned} \tag{2.25}$$

where

$$U_{j\ell,m}(t,\tau) = -\frac{ik_m}{2}\,\frac{z_\ell'(t)\cdot z_j'(\tau)}{|z_\ell'(t)|\,|z_\ell(t) - z_j(\tau)|},$$

and

$$V_{j\ell,m}(t,\tau) = \frac{ik_m}{2}\,\frac{[z_\ell'(t)]^\perp \cdot [z_\ell(t) - z_j(\tau)]}{|z_\ell'(t)|\,|z_\ell(t) - z_j(\tau)|}\,\frac{[z_j'(\tau)]^\perp \cdot\, [z_j(\tau) - z_\ell(t)]}{|z_\ell(t) - z_j(\tau)|}\,.$$

Here, $H_0^{(1)\prime}$ and $H_0^{(1)\prime\prime}$ are the first and the second derivatives of the Hankel function $H_0^{(1)}$ of order zero and of the first kind, respectively.

We denote by $C^{0,\beta}(\Gamma_j)$ and $C^{1,\beta}(\Gamma_j)$ the spaces of Hölder continuous and Hölder continuously differentiable functions with exponent $0 < \beta \leq 1$, respectively. Then all the above operators are compact from $C(\Gamma_j)$ into $C^{0,\beta}(\Gamma_\ell)$ and from $C^{0,\beta}(\Gamma_j)$ into $C^{1,\beta}(\Gamma_\ell)$ for $j \neq \ell$. Furthermore the operators $S_{jj,m} : C^{0,\beta}(\Gamma_j) \to C^{1,\beta}(\Gamma_j)$ are bounded (see Theorem 3.4 in [43]). However in chapter 3 and section 5.1 of chapter 5 we consider $S_{j\ell,m}, K_{j\ell,m}, K'_{j\ell,m} : C(\Gamma_j) \to C(\Gamma_\ell)$ are in the space of continuous functions. In this case the mentioned operators are also compact since they represent integral operators with weakly singular kernels for $j = \ell$ and continuous kernels for $j \neq \ell$. For $j \neq \ell$ the operator $T_{j\ell,m} : C(\Gamma_j) \to C(\Gamma_\ell)$ also has a continuous kernel and therefore is compact, but the operator $T_{jj,m}$ is a hypersingular operator that is only defined on subspaces $V_j \subset C\left(\Gamma_j\right)$ of sufficiently smooth functions. However, the difference operator $T_{jj,1} - T_{jj,0} : C(\Gamma_j) \to C(\Gamma_j)$ again has a weakly singular kernel and is compact. For these compactness properties we refer to Section 3.1 in [43].

2.4 On the Numerical Evaluation of the Boundary Integral Operators

The Hankel functions can be expressed by the summation of the Bessel functions and the Neumann functions of order n.

$$H_n^{(1,2)} := J_n \pm iY_n, \quad n = 0, 1, 2, \dots \tag{2.26}$$

Series expansions of the Bessel functions and the Neumann functions for the argument $t \in (0, \infty)$ are given as follows

$$J_n(t) := \sum_{p=0}^{\infty} \frac{(-1)^p}{p!(n+p)!} \left(\frac{t}{2}\right)^{n+2p}, \tag{2.27}$$

$$\begin{aligned} Y_n(t) \quad &:= \quad \frac{2}{\pi}\left\{\ln\frac{t}{2} + C\right\} J_n(t) - \frac{1}{\pi}\sum_{p=0}^{n-1} \frac{(n-1-p)!}{p!}\left(\frac{2}{t}\right)^{n-2p} \\ & \qquad -\frac{1}{\pi}\sum_{p=0}^{\infty} \frac{(-1)^p}{p!(n+p)!}\left(\frac{t}{2}\right)^{n+2p} \{\psi(p+n) + \psi(p)\}. \end{aligned} \tag{2.28}$$

Here we define $\psi(0) := 0$, and

$$\psi(p) := \sum_{m=1}^{p} \frac{1}{m}, \quad p = 1, 2, \dots \tag{2.29}$$

and C is the Euler constant given by

$$C := \lim_{p\to\infty}\left\{\sum_{m=1}^{p}\frac{1}{m} - \ln p\right\}, \tag{2.30}$$

which is approximately equals to $C \approx 0.577215$.

Kernels of the integral operators given by (2.22) - (2.25) contain Hankel functions having logarithmic singularities at $t=\tau$ for $j=\ell=\{0,1\}$ which can be seen from the series expansion of the Neumann function in (2.28). Therefore for the proper numerical treatment of the singularities occuring in the mentioned operators we follow [43, 99, 100] and split the kernels as a summation of singular and continuous terms

$$M_{\ell\ell,m}(t,\tau) = M^{[1]}_{\ell\ell,m}(t,\tau)\,\ln\left(4\sin^2\frac{t-\tau}{2}\right) + M^{[2]}_{\ell\ell,m}(t,\tau), \qquad \ell\in(0,1). \tag{2.31}$$

Here $M_{\ell\ell,m}$ is one of the kernels in (2.22) - (2.25) and $M^{[1]}_{\ell\ell,m}$ and $M^{[2]}_{\ell\ell,m}$ are the appropriate functions for each kernel which permits us to split the singular and regular parts of the kernel $M_{\ell\ell,m}$. Then we approximate the integrals by quadrature formulas. To this aim we choose $2n$ equidistant points via

$$\tau_p := p\frac{\pi}{n}, \qquad p=0,\cdots,2n-1\,, \tag{2.32}$$

and use quadrature rules

$$\int_0^{2\pi}\ln\left(4\sin^2\frac{t-\tau}{2}\right)M^{[1]}_{\ell\ell,m}(t,\tau)\,d\tau \approx \sum_{p=0}^{2n-1}R^{(n)}_p(t)\,M^{[1]}_{\ell\ell,m}(t,\tau_p), \quad t\in[0,2\pi], \tag{2.33}$$

$$\int_0^{2\pi}M^{[2]}_{\ell\ell,m}(t,\tau)\,d\tau \approx \frac{\pi}{n}\sum_{p=0}^{2n-1}M^{[2]}_{\ell\ell,m}(t,\tau_p), \quad t\in[0,2\pi], \tag{2.34}$$

where

$$R^{(n)}_p(t) := -\frac{2\pi}{n}\sum_{r=1}^{n-1}\frac{1}{r}\cos r\,(t-\tau_p) - \frac{\pi}{n^2}\cos n\,(t-\tau_p), \qquad p=0,\cdots,2n-1\,.$$

In order to solve an integral equation in the form

$$\psi(t) - \int_0^{2\pi}M_{\ell\ell,m}(t,\tau)\,\psi(\tau)\,d\tau \;=\; g(t), \qquad 0\le t\le 2\pi, \tag{2.35}$$

we apply quadrature rules (2.33) - (2.34) and obtain a fully discrete linear system for the unknown values of the density function ψ,

$$\psi^{(n)}(t_i) - \sum_{p=0}^{2n-1}\left\{R^{(n)}_{|i-p|}(t_i)\,M^{[1]}_{\ell\ell,m}(t_i,\tau_p) \;+\; \frac{\pi}{n}M^{[2]}_{\ell\ell,m}(t_i,\tau_p)\right\}\psi^{(n)}(\tau_p) \;=\; g(t_i), \tag{2.36}$$

for $t_i := i\pi/n$, and $i = 0, \cdots, 2n-1$. Then the function ψ can be computed at any point via the following representation

$$\psi^{(n)}(t) := \sum_{p=0}^{2n-1} \left\{ R_p^{(n)}(t)\, M_{\ell\ell,m}^{[1]}(t,\tau_p) \;+\; \frac{\pi}{n} M_{\ell\ell,m}^{[2]}(t,\tau_p) \right\} \psi^{(n)}(\tau_p) \;+\; g(t)\,. \tag{2.37}$$

We continue our study with presenting the expressions of $M_{\ell\ell,m}$, $M_{\ell\ell,m}^{[1]}$ and $M_{\ell\ell,m}^{[2]}$ for each parametrized boundary integral operator (2.22) - (2.25) which can be obtained after splitting the mentioned operators according to the form given in (2.31). In this direction, the kernel $M_{\ell\ell,m}$ of the single-layer operator $\widetilde{S}_{\ell\ell,m}$

$$M_{\ell\ell,m}(t,\tau) = \frac{i}{2} H_0^{(1)}\left(k_m |z_\ell(t) - z_\ell(\tau)|\right), \tag{2.38}$$

is given. As indicated above we obtained the following expressions for $t \neq \tau$,

$$\begin{aligned} M_{\ell\ell,m}^{[1]}(t,\tau) &= -\frac{1}{2\pi} J_0\left(k_m |z_\ell(t) - z_\ell(\tau)|\right), \\ M_{\ell\ell,m}^{[2]}(t,\tau) &= M_{\ell\ell,m}(t,\tau) - M_{\ell\ell,m}^{[1]}(t,\tau) \ln\left(4\sin^2\frac{t-\tau}{2}\right), \end{aligned} \tag{2.39}$$

and for $t = \tau$,

$$M_{\ell\ell,m}^{[1]}(t,t) = -\frac{1}{2\pi}, \tag{2.40}$$

and

$$M_{\ell\ell,m}^{[2]}(t,t) = \frac{i}{2} - \frac{C}{\pi} - \frac{1}{2\pi} \ln\left(\frac{k_m^2}{4}\{[z_{1\ell}'(t)]^2 + [z_{2\ell}'(t)]^2\}\right). \tag{2.41}$$

The last two expressions corresponds to the diagonal terms of the kernel given in (2.38). For the double-layer operator $\widetilde{K}_{\ell\ell,m}$ the kernel is given by

$$M_{\ell\ell,m}(t,\tau) = \frac{ik_m}{2} \frac{[z_\ell'(\tau)]^\perp \cdot [z_\ell(\tau) - z_\ell(t)]}{|z_\ell'(\tau)|\,|z_\ell(t) - z_\ell(\tau)|} H_0^{(1)\prime}(k_m |z_\ell(t) - z_\ell(\tau)|), \tag{2.42}$$

where

$$\begin{aligned} M_{\ell\ell,m}^{[1]}(t,\tau) &= \frac{k_m}{2\pi} \frac{[z_\ell'(\tau)]^\perp \cdot [z_\ell(t) - z_\ell(\tau)]}{\{|z_\ell(t) - z_\ell(\tau)|\}\{[z_{1\ell}'(\tau)]^2 + [z_{2\ell}'(\tau)]^2\}^{1/2}} J_1\left(k_m |z_\ell(t) - z_\ell(\tau)|\right), \\ M_{\ell\ell,m}^{[2]}(t,\tau) &= M_{\ell\ell,m}(t,\tau) - M_{\ell\ell,m}^{[1]}(t,\tau) \ln\left(4\sin^2\frac{t-\tau}{2}\right), \end{aligned} \tag{2.43}$$

and the diagonal terms

$$M_{\ell\ell,m}^{[2]}(t,t) = \frac{1}{2\pi} \frac{z_{1\ell}'(t)\, z_{2\ell}''(t) - z_{2\ell}'(t)\, z_{1\ell}''(t)}{\{[z_{1\ell}'(t)]^2 + [z_{2\ell}'(t)]^2\}^{3/2}}. \tag{2.44}$$

Applying the same procedure to the normal derivative of the single-layer operator $\widetilde{K}'_{\ell\ell,m}$ we obtain

$$M_{\ell\ell,m}(t,\tau) = \frac{ik_m}{2}\,\frac{[z'_\ell(t)]^\perp\cdot[z_\ell(t)-z_\ell(\tau)]}{|z'_\ell(t)|\,|z_\ell(t)-z_\ell(\tau)|}\,H_0^{(1)\prime}(k_m|z_\ell(t)-z_\ell(\tau)|)\,, \tag{2.45}$$

where

$$M^{[1]}_{\ell\ell,m}(t,\tau) = \frac{k_m}{2\pi}\,\frac{[z'_\ell(t)]^\perp\cdot[z_\ell(\tau)-z_\ell(t)]}{\{|z_\ell(t)-z_\ell(\tau)|\}\{[z'_{1\ell}(t)]^2+[z'_{2\ell}(t)]^2\}^{1/2}}\,J_1\left(k_m|z_\ell(t)-z_\ell(\tau)|\right),$$

$$M^{[2]}_{\ell\ell,m}(t,\tau) = M_{\ell\ell,m}(t,\tau) - M^{[1]}_{\ell\ell,m}(t,\tau)\ln\left(4\sin^2\frac{t-\tau}{2}\right), \tag{2.46}$$

and the diagonal terms

$$M^{[2]}_{\ell\ell,m}(t,t) = \frac{1}{2\pi}\frac{z'_{1\ell}(t)\,z''_{2\ell}(t)-z'_{2\ell}(t)\,z''_{1\ell}(t)}{[z'_{1\ell}(t)]^2+[z'_{2\ell}(t)]^2}\,. \tag{2.47}$$

Borrowing the following identity

$$\widetilde{T}_{\ell\ell,m}\widetilde{f} = \frac{d}{d\boldsymbol{s}}\widetilde{S}_{\ell\ell,m}\frac{d\widetilde{f}}{d\boldsymbol{s}} + k_m^2\,\boldsymbol{\nu}_\ell\cdot\widetilde{S}_{\ell\ell,m}(\boldsymbol{\nu}_\ell\widetilde{f}) \tag{2.48}$$

from the paper [101] enables us to introduce the idea how to split the normal derivative of the parametrized double-layer operator $\widetilde{T}_{\ell\ell,m}$ where $\widetilde{f}$ is a parametrized density function. The derivation of the equation (2.48) is given in the page 102 of [44] for $k_m = 0$. The first part of the summation in the right hand side of the the equation (2.48) can be decomposed as

$$\left(\frac{d}{d\boldsymbol{s}}\widetilde{S}_{\ell\ell,m}\frac{d\widetilde{f}}{d\boldsymbol{s}}\right)z_\ell(t) = \frac{1}{|z'_\ell(t)|}\int_0^{2\pi}\left\{\frac{1}{2\pi}\cot\frac{\tau-t}{2}\frac{d\widetilde{f}(z_\ell(\tau))}{d\tau} - N_{\ell\ell,m}(t,\tau)\widetilde{f}(z_\ell(\tau))\right\}d\tau \tag{2.49}$$

The integral having cotangent kernel can be approximately computed,

$$\frac{1}{2\pi}\int_0^{2\pi}\cot\frac{\tau-t}{2}\,\widetilde{f}'(\tau)\,d\tau \approx \sum_{p=0}^{2n-1} T_p^{(n)}(t)\,\widetilde{f}(\tau_p)\,,\quad t\in[0,2\pi]\,, \tag{2.50}$$

with quadrature weights

$$T_p^{(n)}(t) := -\frac{1}{n}\sum_{r=1}^{n-1} r\cos r\,(t-\tau_p^{(n)}) - \frac{1}{2}\cos n\,(t-\tau_p^{(n)})\,,\qquad p = 0,\cdots,2n-1\,. \tag{2.51}$$

$N_{\ell\ell,m}(t,\tau)$ appearing in the equation (2.49) can be splitted

$$N_{\ell\ell,m}(t,\tau) = N^{[1]}_{\ell\ell,m}(t,\tau)\,\ln\left(4\sin^2\frac{t-\tau}{2}\right) + N^{[2]}_{\ell\ell,m}(t,\tau). \tag{2.52}$$

Here,

$$N^{[1]}_{\ell\ell,m}(t,\tau) = -\frac{1}{2\pi}N^{\dagger}_{\ell\ell,m}(t,\tau)\left\{k_m^2 J_0(k_m|z_\ell(t)-z_\ell(\tau)|) - \frac{2k_m J_1(k_m|z_\ell(t)-z_\ell(\tau)|)}{|z_\ell(t)-z_\ell(\tau)|}\right\}$$
$$-\frac{k_m z'_\ell(t)\cdot z'_\ell(\tau)}{2\pi|z_\ell(t)-z_\ell(\tau)|} J_1(k_m|z_\ell(t)-z_\ell(\tau)|) \tag{2.53}$$

and $N^{\dagger}_{\ell\ell,m}$ is defined

$$N^{\dagger}_{\ell\ell,m}(t,\tau) := \frac{z'_\ell(t)\cdot(z_\ell(t)-z_\ell(\tau))\, z'_\ell(\tau)\cdot(z_\ell(t)-z_\ell(\tau))}{|z_\ell(t)-z_\ell(\tau)|^2}\,. \tag{2.54}$$

$N^{[2]}_{\ell\ell,m}$ appearing in the equation (2.52) can be expressed by terms of $N_{\ell\ell,m}$ and $N^{[1]}_{\ell\ell,m}$ as follows

$$N^{[2]}_{\ell\ell,m}(t,\tau) = N_{\ell\ell,m}(t,\tau) - N^{[1]}_{\ell\ell,m}(t,\tau)\ \ln\left(4\sin^2\frac{t-\tau}{2}\right). \tag{2.55}$$

where we have an expression of

$$N_{\ell\ell,m}(t,\tau) = \frac{i}{2}N^{\dagger}_{\ell\ell,m}(t,\tau)\left\{k_m^2 H_0^{(1)}(k_m|z_\ell(t)-z_\ell(\tau)|) - \frac{2k_m H_1^{(1)}(k_m|z_\ell(t)-z_\ell(\tau)|)}{|z_\ell(t)-z_\ell(\tau)|}\right\}$$
$$+\frac{i}{2}\frac{k_m z'_\ell(t)\cdot z'_\ell(\tau)}{|z_\ell(t)-z_\ell(\tau)|} H_1^{(1)}(k_m|z_\ell(t)-z_\ell(\tau)|) + \frac{1}{4\pi\sin^2\frac{1}{2}(t-\tau)}\,. \tag{2.56}$$

The diagonal terms of $N^{[1]}_{\ell\ell,m}$ and $N^{[2]}_{\ell\ell,m}$ are given by

$$N^{[1]}_{\ell\ell,m}(t,t) = -\frac{k_m^2|z'_\ell(t)|^2}{4\pi} \tag{2.57}$$

$$N^{[2]}_{\ell\ell,m}(t,t) = \left(\pi i - 1 - 2C - 2\ln\frac{k_m|z'_\ell(t)|}{2}\right)\frac{k_m^2|z'_\ell(t)|^2}{4\pi}$$
$$+\frac{1}{12\pi} + \frac{[z'_\ell(t)\cdot z''_\ell(t)]^2}{2\pi|z'_\ell(t)|^4} - \frac{|z''_\ell(t)|^2}{4\pi|z'_\ell(t)|^2} + \frac{z'_\ell(t)\cdot z'''_\ell(t)}{6\pi|z'_\ell(t)|^2} \tag{2.58}$$

2.5 Integral Representations of the Fields

Throughout the thesis for the solution of direct problems we seek integral representations of the scattered field u^s and the interior total field u_0 in the form of combined single- and double-layer potentials by defining continuous density functions

ψ, ϕ, χ, on the boundaries of the obstacles. That is,

$$u^s(\boldsymbol{x}) = \int_{\Gamma_1} \left\{ \frac{\partial \Phi_1(\boldsymbol{x},\boldsymbol{y})}{\partial \boldsymbol{\nu}_1(\boldsymbol{y})} \, \psi(\boldsymbol{y}) + \Phi_1(\boldsymbol{x},\boldsymbol{y}) \varphi(\boldsymbol{y}) \right\} ds(\boldsymbol{y}), \quad \boldsymbol{x} \in D_1, \tag{2.59}$$

$$u_0(\boldsymbol{x}) = \int_{\Gamma_1} \left\{ \frac{\partial \Phi_0(\boldsymbol{x},\boldsymbol{y})}{\partial \boldsymbol{\nu}_1(\boldsymbol{y})} \, \psi(\boldsymbol{y}) + \Phi_0(\boldsymbol{x},\boldsymbol{y}) \varphi(\boldsymbol{y}) \right\} ds(\boldsymbol{y}) + \tag{2.60}$$
$$+ \int_{\Gamma_0} \Phi_0(\boldsymbol{x},\boldsymbol{y}) \chi(\boldsymbol{y}) \, ds(\boldsymbol{y}), \quad \boldsymbol{x} \in D_0.$$

We substitute these field representations to the proper boundary conditions for every direct problem and obtain a system of boundary integral equations for the unknown potential densities. The numerical solution of these equations allow us to compute the scattered field (near-field). The parametric form of the scattered field for $\boldsymbol{x} \in D_1$

$$u^s(\boldsymbol{x}) = \int_0^{2\pi} [z_1'(\tau)]^{\perp} \cdot \operatorname{grad} \Phi_1(\boldsymbol{x}, z_1(\tau)) \; \psi(z_1(\tau)) \, d\tau +$$
$$+ \int_0^{2\pi} \Phi_1(\boldsymbol{x}, z_1(\tau)) \; \varphi(z_1(\tau)) \, |z_1'(\tau)| \, d\tau, \tag{2.61}$$

and for $\boldsymbol{x} \in D_0$ the interior total field are given as

$$u_0(\boldsymbol{x}) = \int_0^{2\pi} [z_1'(\tau)]^{\perp} \cdot \operatorname{grad} \Phi_0(\boldsymbol{x}, z_1(\tau)) \; \psi(z_1(\tau)) \, d\tau +$$
$$+ \int_0^{2\pi} \Phi_0(\boldsymbol{x}, z_1(\tau)) \; \varphi(z_1(\tau)) \, |z_1'(\tau)| \, d\tau + \int_0^{2\pi} \Phi_0(\boldsymbol{x}, z_0(\tau)) \; \chi(z_0(\tau)) \, |z_0'(\tau)| \, d\tau. \tag{2.62}$$

By the asymptotics of the Hankel function, the integral representation of the far-field pattern of (2.59) is given by

$$u_\infty(\boldsymbol{x}) = \frac{e^{-i\pi/4}}{\sqrt{8\pi k_1}} \int_{\Gamma_1} \{ k_1 \boldsymbol{x} \cdot \boldsymbol{\nu}_1(\boldsymbol{y}) \psi(\boldsymbol{y}) + i \, \varphi(\boldsymbol{y}) \} \, e^{-ik_1 \boldsymbol{x} \cdot \boldsymbol{y}} \, ds(\boldsymbol{y}), \quad \boldsymbol{x} \in \Omega, \tag{2.63}$$

where Ω is the unity circle. The parametrized form of (2.63)

$$u_\infty(\boldsymbol{x}) = \gamma \int_0^{2\pi} \left\{ k_1 \, [z_1'(\tau)]^{\perp} \cdot \boldsymbol{x} \; \psi(z_1(\tau)) + i \, \varphi(z_1(\tau)) \, |z_1'(\tau)| \right\} e^{-ik_1 z_1(\tau) \cdot \boldsymbol{x}} \, d\tau \tag{2.64}$$

where $\gamma = e^{-i\pi/4} / \sqrt{8\pi k_1}$ and $\boldsymbol{x} \in \Omega$.

For the inverse problem case we represent the fields by using only single-layer potentials such as,

$$u^s(\boldsymbol{x}) = \int_{\Gamma_1} \Phi_1(\boldsymbol{x},\boldsymbol{y}) \varphi(\boldsymbol{y}) ds(\boldsymbol{y}), \quad \boldsymbol{x} \in D_1, \tag{2.65}$$

$$u_0(\boldsymbol{x}) = \int_{\Gamma_1} \Phi_0(\boldsymbol{x},\boldsymbol{y}) \psi(\boldsymbol{y}) \, ds(\boldsymbol{y}) + \int_{\Gamma_0} \Phi_0(\boldsymbol{x},\boldsymbol{y}) \chi(\boldsymbol{y}) \, ds(\boldsymbol{y}), \quad \boldsymbol{x} \in D_0. \tag{2.66}$$

In this thesis, here and further on whenever we consider single-layer potential representation of the field we always assume that $k_j^2,\ j=0,1$ is not a Dirichlet eigenvalue for the negative Laplacian in the interior of the integration curve. The parametrized field representations are

$$u^s(\boldsymbol{x}) = \int_0^{2\pi} \Phi_1(\boldsymbol{x}, z_1(\tau))\, \varphi(z_1(\tau))\, |z_1'(\tau)|\, d\tau, \quad \boldsymbol{x} \in D_1, \tag{2.67}$$

$$\begin{aligned} u_0(\boldsymbol{x}) &= \int_0^{2\pi} \Phi_0(\boldsymbol{x}, z_1(\tau))\, \psi(z_1(\tau))\, |z_1'(\tau)|\, d\tau + \\ &+ \int_0^{2\pi} \Phi_0(\boldsymbol{x}, z_0(\tau))\, \chi(z_0(\tau))\, |z_0'(\tau)|\, d\tau, \quad \boldsymbol{x} \in D_0. \end{aligned} \tag{2.68}$$

And according to the scattered field representation in (2.65) now the far-field and its parametric expressions for $\boldsymbol{x} \in \Omega$ are

$$u_\infty(\boldsymbol{x}) = \frac{e^{i\pi/4}}{\sqrt{8\pi k_1}} \int_{\Gamma_1} e^{-ik_1 \boldsymbol{x}\cdot\boldsymbol{y}}\, \varphi(\boldsymbol{y})\, ds(\boldsymbol{y}), \tag{2.69}$$

$$u_\infty(\boldsymbol{x}) = \frac{e^{i\pi/4}}{\sqrt{8\pi k_1}} \int_0^{2\pi} e^{-ik_1 \boldsymbol{x}\cdot z_1(\tau)}\, \varphi(z_1(\tau))|z_1'(\tau)|\, d\tau. \tag{2.70}$$

However to avoid suffering from any *inverse crime* in the solutions of inverse problems not only we represent the fields by using only single-layer potentials as given (2.65) and (2.66) but also change the algorithm for finding unknown densities due to the ill-posedness of the problems. The reconstruction algorithms are different for each considered problem and will be explained in details in the following chapters.

In order to obtain noisy data, random errors are added point-wise to the field values u as

$$\tilde{u} = u + \delta\,\rho\, \frac{\|u\|}{\|\rho\|}. \tag{2.71}$$

Here, random variable $\rho \in \mathbb{C}$ and $\{\mathrm{Re}\,\rho, \mathrm{Im}\,\rho\} \in (0,1)$. Parameter δ is called as the *noise ratio* and in this study, it is chosen as $\delta = 0.03$ to have a noise level of 3% and $\delta = 0.05$ to have a noise level of 5%.

Furthermore, in the thesis we prefer to introduce wave numbers for the related numerical experiments. That is, one can compute the operating frequency by choosing medium parameters: dielectric permittivity, magnetic permeability, conductivity etc. For instance, in the case of choosing medium D_1 as dry soil and medium D_0 as mica given in Figure 2.1 one can read mentioned parameters from [107] for soil,

$$\varepsilon_1 \approx 2.8 \times \frac{10^{-9}}{36\pi}\ [F/m], \qquad \mu_1 \approx 4\pi \times 10^{-7}\ [H/m], \qquad \sigma_1 \approx 10^{-4}\ [S/m],$$

and for mica,

$$\varepsilon_0 \approx 5.4 \times \frac{10^{-9}}{36\pi}\,[F/m]\,, \qquad \mu_0 \approx 4\pi \times 10^{-7}\,[H/m]\,, \qquad \sigma_0 \approx 10^{-15}\,[S/m]\,.$$

Then the wave numbers can be computed from the expression (2.4) , i.e.

$$k_1 \approx 3.504 + i0.011 \quad \text{and} \quad k_0 \approx 4.866\,,$$

for the operating frequency 100[MHz]. And wave numbers used in the numerical examples are also in the same range with this example.

In the next chapters of the thesis, we will investigate the solutions of the direct and inverse problems for chosen configurations by using background knowledge given in this chapter and present some illustrative numerical results.

3. IMPEDANCE RECONSTRUCTIONS

This chapter is devoted to reconstructions of impedance functions defined on the boundaries of the buried obstacles from the near-/far-field data for given the shapes of the impedance objects (Γ_0) and the dielectrics (Γ_1). This problem can be considered as an extension of the problem studied by Akduman and Kress in 2003 [82] for the buried obstacles.

3.1 Statement of the Direct Problem

The direct scattering problem considered here is the computation of the scattered near- or far-field pattern of an arbitrarily shaped impedance cylinder buried in another arbitrarily shaped dielectric cylinder in 2-D for single time-harmonic plane wave excitation provided that the interior and the exterior total fields both satisfy the Helmholtz equation in the corresponding media. Therefore, we consider the geometry of the problem as given in Figure 3.1

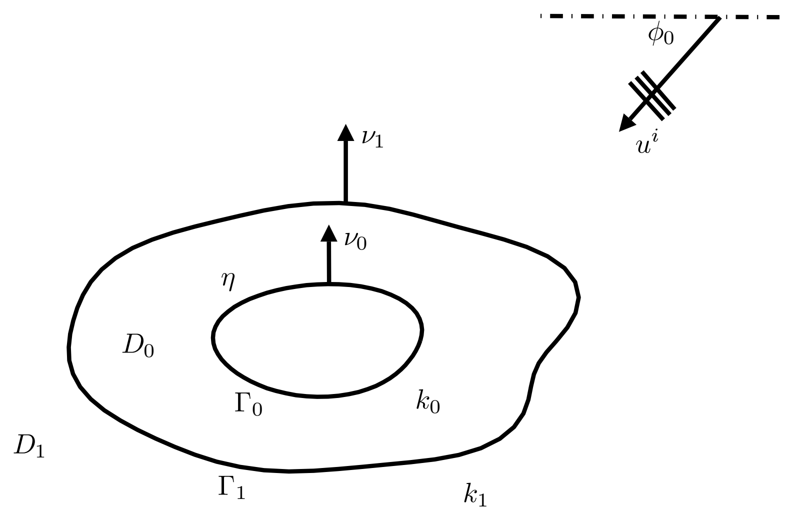

η : Inhomogeneous impedance function

Figure 3.1: Geometry of the buried impedance reconstruction problem

Furthermore, in this problem it is considered that the total fields satisfy the transmission conditions

$$u_0 = u_1 \qquad \text{on} \quad \Gamma_1\,, \tag{3.1}$$

$$\frac{\partial u_1}{\partial \boldsymbol{\nu}_1} = \frac{\partial u_0}{\partial \boldsymbol{\nu}_1} \qquad \text{on} \quad \Gamma_1\,, \tag{3.2}$$

and the impedance boundary condition

$$u_0 + \frac{\eta}{ik_0}\,\frac{\partial u_0}{\partial \boldsymbol{\nu}_0} = 0 \qquad \text{on} \quad \Gamma_0\,, \tag{3.3}$$

for some continuous function η satisfying

$$\mathrm{Re}\,\frac{\eta}{k_0} \geq 0 \tag{3.4}$$

in order to establish the unqiue solution of the direct problem, see [85] and

$$\eta(x) \neq 0\,, \quad x \in \Gamma_0\,. \tag{3.5}$$

We also assume that $\sigma_1 = 0$, i.e., k_1 is real and positive. Here, transmission conditions (3.1) and (3.2) ensures the continuity of the tangential components of the electric and the magnetic field at the interface Γ_1 and the condition (3.3) models the standard impedance condition on the boundary Γ_0.

For the solution of the direct scattering problem we follow Chapter 2, Section 2.5 and use the integral representations of the fields which are given by the equations (2.59) and (2.60). However, in order to substitute scattered (2.59) and interior total fields (2.60) to the considered boundary conditions the field expressions have to be rewritten on the boundaries according to the jump relations. After that we can substitute resultant expressions to the boundary conditions defined by (3.1)-(3.3) using the decomposition $u_1 = u^i + u^s$. For the sake of brevity, we will write the integral equations in the operator form. To do so we first define the fields on the boundaries.

Scattered field on Γ_1:

$$2u^s(\boldsymbol{x})|_{\Gamma_1} = \underbrace{2\int_{\Gamma_1} \frac{\partial \Phi_1(\boldsymbol{x},\boldsymbol{y})}{\partial \boldsymbol{\nu}_1(\boldsymbol{y})}\,\psi(\boldsymbol{y})\,ds(\boldsymbol{y})}_{K_{11,1}\psi} + \psi(\boldsymbol{x}) + \underbrace{2\int_{\Gamma_1} \Phi_1(\boldsymbol{x},\boldsymbol{y})\,\varphi(\boldsymbol{y})\,ds(\boldsymbol{y})}_{S_{11,1}\varphi} \tag{3.6}$$

Normal derivative of the scattered field on Γ_1:

$$2\frac{\partial u^s}{\partial \boldsymbol{\nu}_1}(\boldsymbol{x})\bigg|_{\Gamma_1} = \underbrace{2\frac{\partial}{\partial \boldsymbol{\nu}_1(\boldsymbol{x})}\int_{\Gamma_1}\frac{\partial \Phi_1(\boldsymbol{x},\boldsymbol{y})}{\partial \boldsymbol{\nu}_1(\boldsymbol{y})}\,\psi(\boldsymbol{y})\,ds(\boldsymbol{y})}_{T_{11,1}\psi} + \underbrace{+2\int_{\Gamma_1}\frac{\partial \Phi_1(\boldsymbol{x},\boldsymbol{y})}{\partial \boldsymbol{\nu}_1(\boldsymbol{x})}\,\varphi(\boldsymbol{y})\,ds(\boldsymbol{y})}_{K'_{11,1}\varphi} - \varphi(\boldsymbol{x}) \tag{3.7}$$

Interior total field on Γ_1:

$$2u_0(\boldsymbol{x})|_{\Gamma_1} = \underbrace{2\int_{\Gamma_1}\frac{\partial \Phi_0(\boldsymbol{x},\boldsymbol{y})}{\partial \boldsymbol{\nu}_1(\boldsymbol{y})}\,\psi(\boldsymbol{y})\,ds(\boldsymbol{y})}_{K_{11,0}\psi} - \psi(\boldsymbol{x}) + \underbrace{+2\int_{\Gamma_1}\Phi_0(\boldsymbol{x},\boldsymbol{y})\,\varphi(\boldsymbol{y})\,ds(\boldsymbol{y})}_{S_{11,0}\varphi} + \underbrace{2\int_{\Gamma_0}\Phi_0(\boldsymbol{x},\boldsymbol{y})\,\chi(\boldsymbol{y})\,ds(\boldsymbol{y})}_{S_{01,0}\chi} \tag{3.8}$$

Normal derivative of the interior total field on Γ_1:

$$2\frac{\partial u_0}{\partial \boldsymbol{\nu}_1}(\boldsymbol{x})\bigg|_{\Gamma_1} = \underbrace{2\frac{\partial}{\partial \boldsymbol{\nu}_1(\boldsymbol{x})}\int_{\Gamma_1}\frac{\partial \Phi_0(\boldsymbol{x},\boldsymbol{y})}{\partial \boldsymbol{\nu}_1(\boldsymbol{y})}\,\psi(\boldsymbol{y})\,ds(\boldsymbol{y})}_{T_{11,0}\psi} + \underbrace{+2\int_{\Gamma_1}\frac{\partial \Phi_0(\boldsymbol{x},\boldsymbol{y})}{\partial \boldsymbol{\nu}_1(\boldsymbol{x})}\,\varphi(\boldsymbol{y})\,ds(\boldsymbol{y})}_{K'_{11,0}\varphi} + \varphi(\boldsymbol{x}) + \underbrace{2\int_{\Gamma_0}\frac{\partial \Phi_0(\boldsymbol{x},\boldsymbol{y})}{\partial \boldsymbol{\nu}_1(\boldsymbol{x})}\,\chi(\boldsymbol{y})\,ds(\boldsymbol{y})}_{K'_{01,0}\chi} \tag{3.9}$$

Interior total field on Γ_0:

$$2u_0(\boldsymbol{x})|_{\Gamma_0} = \underbrace{2\int_{\Gamma_1}\frac{\partial \Phi_0(\boldsymbol{x},\boldsymbol{y})}{\partial \boldsymbol{\nu}_1(\boldsymbol{y})}\,\psi(\boldsymbol{y})\,ds(\boldsymbol{y})}_{K_{10,0}\psi} + \underbrace{2\int_{\Gamma_1}\Phi_0(\boldsymbol{x},\boldsymbol{y})\,\varphi(\boldsymbol{y})\,ds(\boldsymbol{y})}_{S_{10,0}\varphi} + \underbrace{+2\int_{\Gamma_0}\Phi_0(\boldsymbol{x},\boldsymbol{y})\,\chi(\boldsymbol{y})\,ds(\boldsymbol{y})}_{S_{00,0}\chi} \tag{3.10}$$

Normal derivative of the interior total field on Γ_0:

$$2\frac{\partial u_0}{\partial \boldsymbol{\nu}_0}(\boldsymbol{x})\bigg|_{\Gamma_0} = \underbrace{2\frac{\partial}{\partial \boldsymbol{\nu}_0(\boldsymbol{x})}\int_{\Gamma_1}\frac{\partial \Phi_0(\boldsymbol{x},\boldsymbol{y})}{\partial \boldsymbol{\nu}_1(\boldsymbol{y})}\,\psi(\boldsymbol{y})\,ds(\boldsymbol{y})}_{T_{10,0}\psi} + \underbrace{+2\int_{\Gamma_1}\frac{\partial \Phi_0(\boldsymbol{x},\boldsymbol{y})}{\partial \boldsymbol{\nu}_0(\boldsymbol{x})}\,\varphi(\boldsymbol{y})\,ds(\boldsymbol{y})}_{K'_{10,0}\varphi} + \underbrace{2\int_{\Gamma_0}\frac{\partial \Phi_0(\boldsymbol{x},\boldsymbol{y})}{\partial \boldsymbol{\nu}_0(x)}\,\chi(\boldsymbol{y})\,ds(\boldsymbol{y})}_{K'_{00,0}\chi} - \chi(\boldsymbol{x}) \tag{3.11}$$

Now one obtains a system of integral equations by substituting the field representations (3.6) - (3.11) to the transmission (3.1),(3.2) and impedance (3.3) boundary conditions as given below

$$
\begin{aligned}
&2\psi + K_{11,1}\psi - K_{11,0}\psi + S_{11,1}\varphi - S_{11,0}\varphi - S_{01,0}\chi = -2u^i|_{\Gamma_1} \,, \\
&2\varphi - T_{11,1}\psi + T_{11,0}\psi - K'_{11,1}\varphi + K'_{11,0}\varphi + K'_{01,0}\chi = 2\left.\frac{\partial u^i}{\partial \boldsymbol{\nu}_1}\right|_{\Gamma_1} \,, \\
&\chi - (T_{10,0}\psi + K'_{10,0}\varphi + K'_{00,0}\chi) - \frac{ik_0}{\eta}(K_{10,0}\psi + S_{10,0}\varphi + S_{00,0}\chi) = 0 \,.
\end{aligned}
\tag{3.12}
$$

The direct scattering problem has at most one solution, provided k_0^2 is not a Dirichlet eigenvalue of the negative Laplacian in the interior of Γ_0, and it is shown in [85] that the fields given by (2.59) and (2.60) solve the direct scattering problem if the continuous densities ψ, φ, χ satisfy the system in (3.12). It suffices to consider (3.12) in $C(\Gamma_1)\times C(\Gamma_1)\times C(\Gamma_0)$ since the mapping properties of the operators imply that for $\psi, \varphi, \chi \in C(\Gamma_1)\times C(\Gamma_1)\times C(\Gamma_0)$ automatically $\varphi \in C^{0,\beta}(\Gamma_1)$, $\chi \in C^{0,\beta}(\Gamma_0)$ and $\psi \in C^{1,\beta}(\Gamma_1)$.

Now, we want to write the system in the abbreviated form. Therefore we introduce an operator,

$A_1 : C(\Gamma_1)\times C(\Gamma_1)\times C(\Gamma_0) \to C(\Gamma_1)\times C(\Gamma_1)\times C(\Gamma_0)$ by

$$
A_1 := \begin{pmatrix}
K_{11,1} - K_{11,0} & S_{11,1} - S_{11,0} & -S_{01,0} \\
-T_{11,1} + T_{11,0} & -K'_{11,1} + K'_{11,0} & K'_{01,0} \\
-2T_{10,0} - \frac{2ik_0}{\eta}K_{10,0} & -2K'_{10,0} - \frac{2ik_0}{\eta}S_{10,0} & -2K'_{00,0} - \frac{2ik_0}{\eta}S_{00,0}
\end{pmatrix},
$$

which is compact since all its components are compact, [43, 85, 98]. Then the integral equation system can be written as

$$
(2I + A_1)\begin{pmatrix} \psi \\ \varphi \\ \chi \end{pmatrix} = 2\begin{pmatrix} -u^i|_{\Gamma_1} \\ \partial u^i/\partial \boldsymbol{\nu}_1|_{\Gamma_1} \\ 0 \end{pmatrix}, \tag{3.13}
$$

where I is the identity operator. Note that in order to obtain density functions ψ, φ, χ we solve the system numerically using parametrized forms of the operators as defined in (2.22) - (2.25) and evaluate singular and regular parts of the parametrized operators, separately. Then substituting the density functions ψ and φ to the equations (2.61) and (2.64) one can obtain the near-field and the far-field, respectively.

3.2 Numerical Examples for the Direct Problem

We use the following tests for the accuracy of the forward code. The transmission boundary value problem of an arbitrarily shaped cylinder mentioned in Chapter 3.8 of [98] can be considered as a special case of our direct problem when the buried obstacle is omitted from the configuration of the problem in Figure 3.1. Hence, first of all we compared our results with some results obtained by the Method of Moments (MoM) for the transmission problem (see [103, 104]).

As a first test using a Potential Approach and Method of Moments we compute near-field on a measurement circle Ω^m, having radius $c_0 = 3$ for a kite-shaped obstacle shown in Figure 3.2.

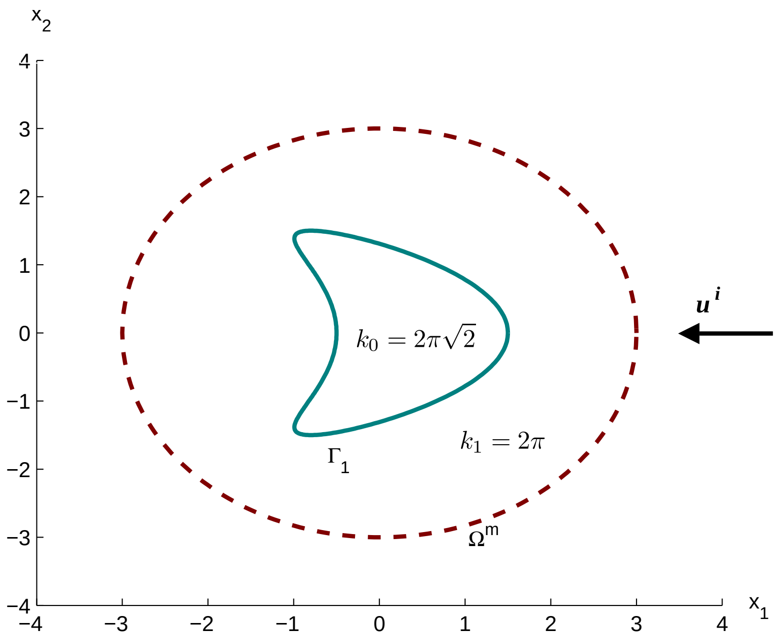

Figure 3.2: Geometry of the problem for Test-1

In particular for the Potential Approach, the near-field is obtained via evaluating the integral given in (2.59). It can be seen from the Figure 3.3 that near-fields match accurately.

In the second investigation we want to compare the far fields obtained by the Potential approach and MoM for another type of obstacle. Therefore for a given peanut shaped geometry in Figure 3.4 we use equation (2.64) to compute the far-field via Potential Approach. And for MoM the scattered field is computed over a measurement circle Ω^m, having radius $c_0 = 10$. Here we also use complex wave number for the interior medium of the dielectric scatterer.

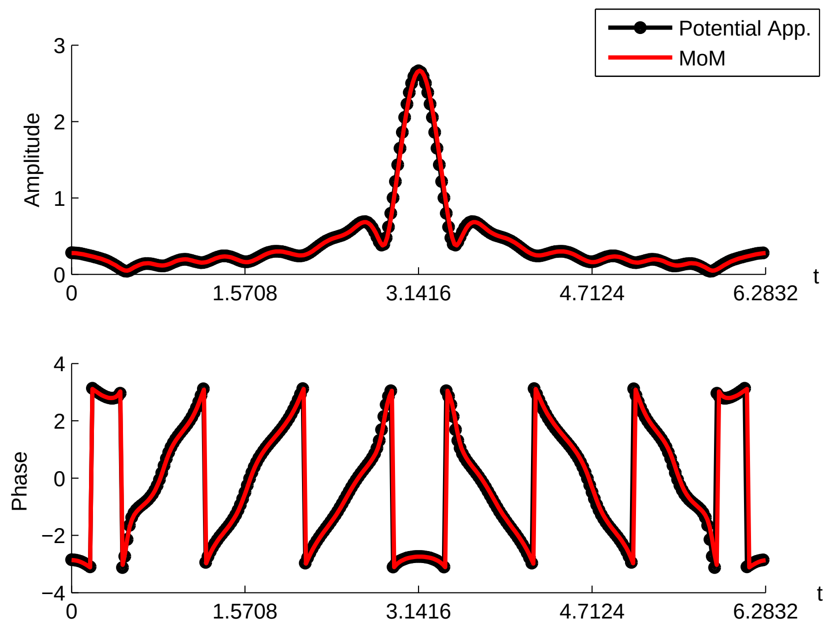

Figure 3.3: Near-fields computed by Potential approach and MoM

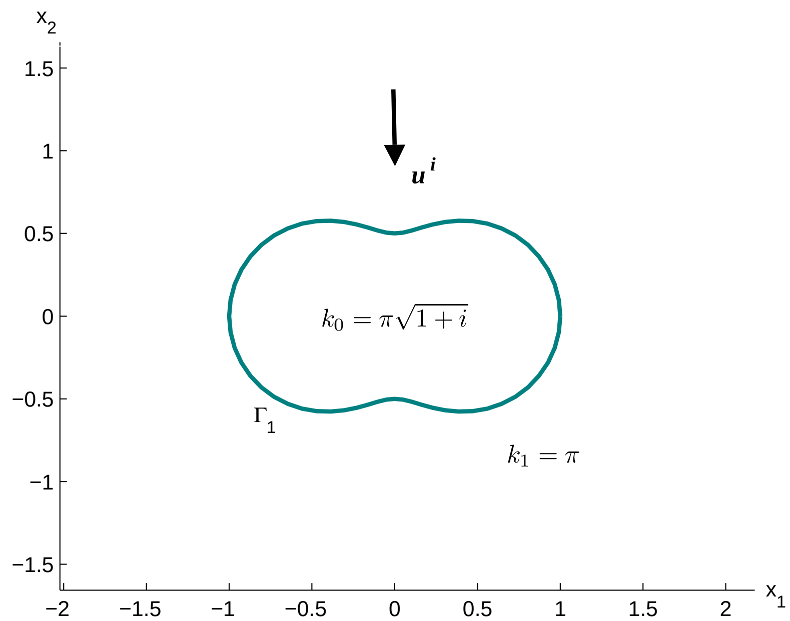

Figure 3.4: Geometry of the problem for Test-2

The comparison of the far-fields obtained by two different methods are given in Figure 3.5.

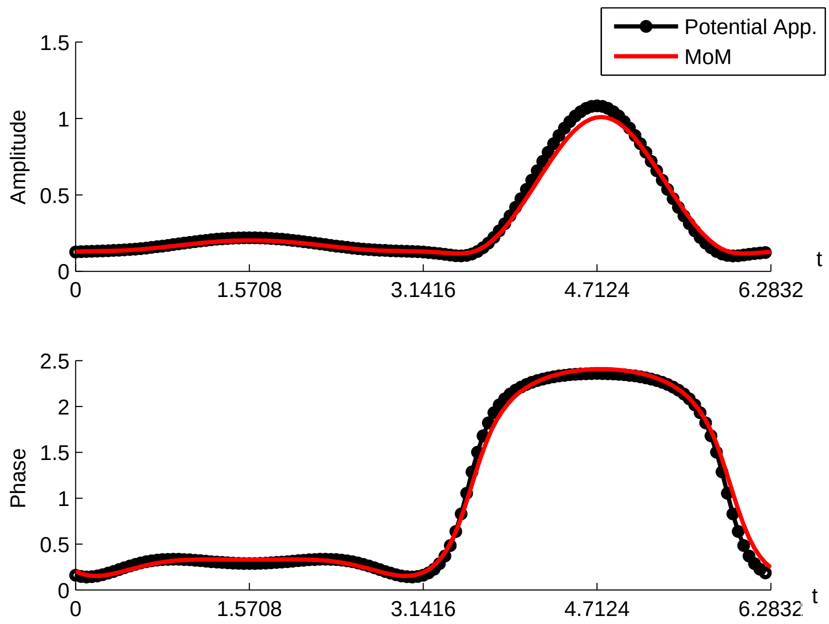

Figure 3.5: Far-fields computed by Potential approach and MoM

As a result it is shown that the near-/far-fields obtained by using two different methods match accurately. However, it is observed that for higher frequencies Nyström method is faster than by the Method of Moments.

We additionally consider the forward problem presented in [82] as another special case of our direct problem when $k_0 = k_1 = 1$. Therefore we reduce our problem to the refence problem investigated in [82]. Along this line the impedance function over an apple shaped obstacle buried in an elliptic cylinder ($e_0 = 1.2$, $e_1 = 0.8$) is chosen as $\eta(z_0(t)) = \sin^2 t + i\cos t$, $t \in [0, 2\pi]$ see Figure 3.6. As it can be seen from the Figure 3.7 both resultant far fields also agree accurately.

We also check the speed of the convergence of our forward code. To this aim we use various types of boundaries with the parametric representation of the curves given in Table 1 and compute approximate values of the far-field pattern $u_\infty(\boldsymbol{d})$ and $u_\infty(\boldsymbol{-d})$ in the forward direction $\boldsymbol{d}$ and the backscattering direction $\boldsymbol{-d}$ obtained through evaluating (2.64) by the trapezoidal rule for the solution to the system of integral equations (3.12) where the number of quadrature points in the Nyström method is N. The direction $\boldsymbol{d}$ of the incident wave is $\boldsymbol{d} = (-1, 0)$. Here we further test the case by

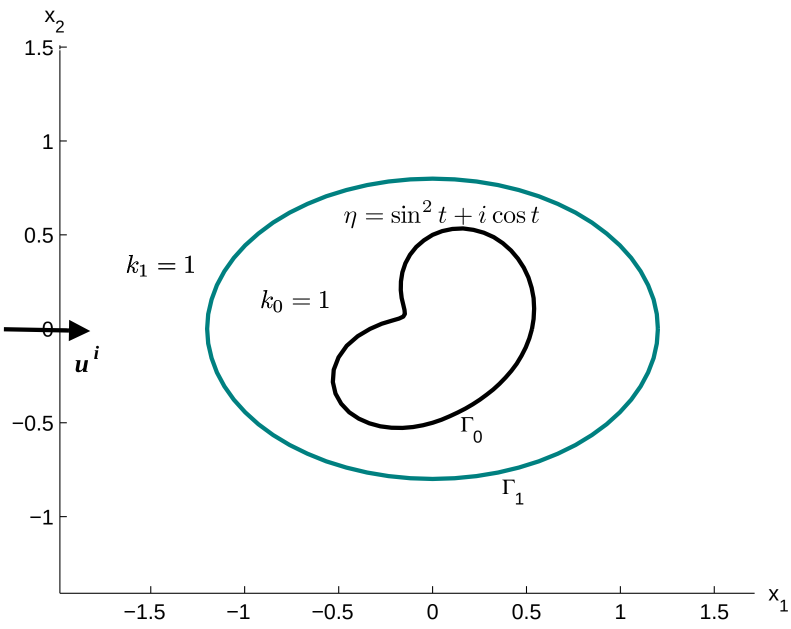

Figure 3.6: Geometry of the problem for Test-3

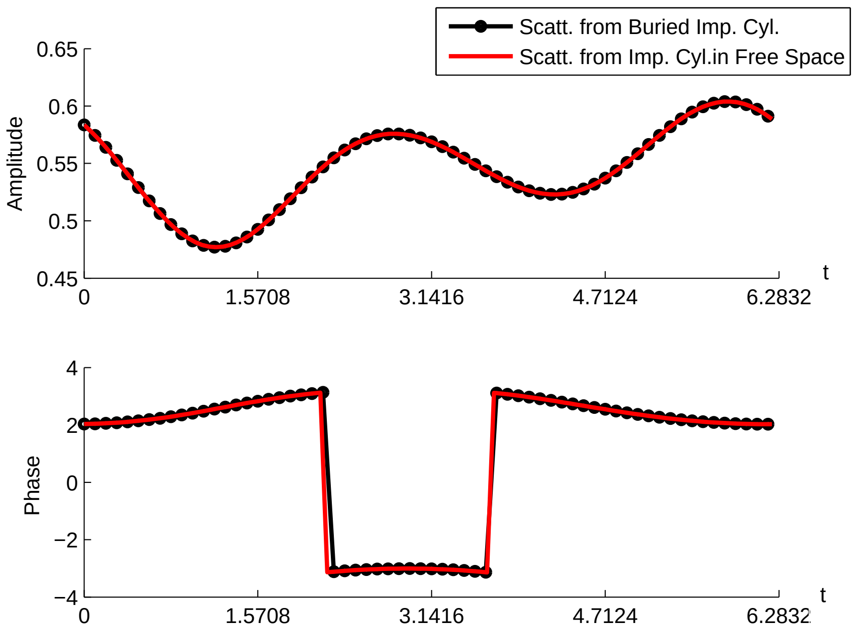

Figure 3.7: Far-Field comparison with the reduced problem in [82]

choosing non-analytical impedance functions as given η_2 in Table 1 and obtained slower convergence speed than analytical impedance functions.
The impedance functions used in the four examples for $t \in [0, 2\pi]$ are,

$$\eta_1(z_0(t)) = \sin^2 t + i\cos^2 t \ , \quad \eta_2(z_0(t)) = e^{-(t-\pi)^2} + i\frac{\sin t}{100} \ ,$$

$$\eta_3(z_0(t)) = \frac{4+\sin t}{5+\cos t} + i\frac{\cos t}{7-\sin t} \ , \quad \eta_4(z_0(t)) = 1.5 + \sin^3 t + i\sin t \ .$$

Table 3.1: Numerical results for the direct buried impedance problem

Parameters:	N	$\mathrm{Re}\, u_\infty(\boldsymbol{d})$	$\mathrm{Im}\, u_\infty(\boldsymbol{d})$	$\mathrm{Re}\, u_\infty(\text{-}\boldsymbol{d})$	$\mathrm{Im}\, u_\infty(\text{-}\boldsymbol{d})$
$\Gamma_0 = \Gamma^{(p)}, \Gamma_1 = \Gamma^{(r)}$	16	0.76469029	0.33025282	-1.83100457	0.96201264
	32	0.76060633	0.34007177	-1.82590173	0.95574934
$\eta = \eta_1$	64	0.76059742	0.34007960	-1.82589332	0.95574400
$k_0 = 1,\ k_1 = 0.5$	128	0.76059742	0.34007960	-1.82589332	0.95574400
$\Gamma_0 = \Gamma^{(c)}, \Gamma_1 = \Gamma^{(e)}$	16	-0.74988421	1.20005719	-2.06346703	0.43885428
$c_0 = 1, e_0 = 3, e_1 = 2$	32	-0.74916948	1.19966827	-2.06251065	0.43973667
$\eta = \eta_2$	64	-0.74916933	1.19966791	-2.06251067	0.43973683
$k_0 = 2,\ k_1 = 0.25$	128	-0.74916930	1.19966781	-2.06251067	0.43973686
$\Gamma_0 = \Gamma^{(k)}, \Gamma_1 = \Gamma^{(t)}$	16	0.27267295	-0.30397367	-1.78884894	0.79839768
	32	0.27742774	-0.24364910	-1.79717617	0.90417055
$\eta = \eta_3$	64	0.27746382	-0.24363491	-1.79721845	0.90418373
$k_0 = 2+2i,\ k_1 = 1$	128	0.27746381	-0.24363491	-1.79721845	0.90418372
$\Gamma_0 = \Gamma^{(p)}, \Gamma_1 = \Gamma^{(s)}$	16	0.18803026	-0.09538729	-2.91692578	2.18850701
	32	0.17698661	0.27437544	-2.70021534	1.86276596
$\eta = \eta_4$	64	0.17707548	0.27432612	-2.70029687	1.86286072
$k_0 = 1,\ k_1 = 2$	128	0.17707548	0.27432612	-2.70029687	1.86286072
$\Gamma_0 = \Gamma^{(e)}, \Gamma_1 = \Gamma^{(a)}$	16	0.02828285	0.21769004	0.13572374	0.46599794
$e_0 = 1.2, e_1 = 0.8$	32	0.01777448	0.23601195	0.13005604	0.48467119
$\eta = 0.2 - i0.3$	64	0.01776323	0.23596266	0.13009672	0.48461955
$k_0 = 3,\ k_1 = 2$	128	0.01776322	0.23596267	0.13009673	0.48461956
$\Gamma_0 = \Gamma^{(k)}, \Gamma_1 = \Gamma^{(c)}$	16	-0.89788315	-0.26054746	-2.74987888	1.53351515
$c_0 = 3$	32	-0.70664878	-0.28046829	-2.68668081	1.50093930
$\eta = 1$	64	-0.70661800	-0.28043077	-2.68620811	1.50115647
$k_0 = 4,\ k_1 = 1$	128	-0.70661800	-0.28043077	-2.68620811	1.50115647

3.3 Inverse Problem

The aim of the inverse scattering problem is to determine the impedance function η from a knowledge of the far-field pattern for one incident wave for the given shapes of the scatterers. This inverse problem is nonlinear in the sense that the scattered wave depends nonlinearly on the impedance η. Furthermore, the inverse problem is ill-posed since the determination of η does not depend continuously on the far-field pattern. We will handle this issue of ill-posedness by employing Tikhonov regularization. Note that the uniqueness result for the solution of the inverse problem is given in [85].

From the given far-field pattern we first reconstruct u^s in D_1 by seeking it in the form of a single-layer potential, see (2.65), which has a far-field pattern given by the equation (2.69). Therefore, given the far-field pattern u_∞, the density $\varphi \in L^2(\Gamma_1)$ is found by solving the integral equation of the first kind

$$S_\infty \varphi = u_\infty \tag{3.14}$$

with the compact operator $S_\infty : L^2(\Gamma_1) \to L^2(\Omega)$ given by

$$S_\infty(\varphi)(\boldsymbol{x}) := \gamma \int_{\Gamma_1} e^{-ik_1 \boldsymbol{x}\cdot\boldsymbol{y}}\, \varphi(\boldsymbol{y})\, ds(\boldsymbol{y}), \quad \boldsymbol{x} \in \Omega. \tag{3.15}$$

where $\gamma = e^{i\pi/4}/\sqrt{8\pi k_1}$. Due to the analytic kernel of S_∞, the integral equation (3.14) is severely ill-posed. For a stable numerical solution of (3.14) Tikhonov regularization can be applied, that is, the ill-posed equation (3.14) is replaced by

$$\alpha_1 \varphi + S_\infty^* S_\infty \varphi = S_\infty^* u_\infty \tag{3.16}$$

with some positive regularization parameter α_1 and the adjoint $S_\infty^* : L^2(\Omega) \to L^2(\Gamma_1)$ of S_∞. Once we have determined φ, and consequently u_1 via (2.65), we seek u_0 as a single-layer potential (2.66).

Given u^s it is an immediate consequence of the jump relations that the field (2.66) satisfies the transmission conditions (3.1) and (3.2) provided the densities ψ and χ solve the system of integral equations

$$\begin{aligned} &S_{11,0}\psi + S_{01,0}\chi = 2u^i|_{\Gamma_1} + S_{11,1}\varphi \\ &K'_{11,0}\psi + \psi + K'_{01,0}\chi = 2\, \frac{\partial u^i}{\partial \boldsymbol{\nu}_1}\bigg|_{\Gamma_1} + K'_{11,1}\varphi - \varphi \end{aligned} \tag{3.17}$$

If k_0^2 is not a Dirichlet eigenvalue for the interior of Γ_1, then the inverse operator $(I + K'_{11,0})^{-1} : L^2(\Gamma_1) \to L^2(\Gamma_1)$ exists (see Theorem 3.17 in [98]). Now we continue our investigation by expressing $\psi \in L^2(\Gamma_1)$ through $\chi \in L^2(\Gamma_0)$ from the second equation of (3.17),

$$\psi = (I + K'_{11,0})^{-1} \left\{ \left(2\, \frac{\partial u^i}{\partial \boldsymbol{\nu}_1} + K'_{11,1}\varphi - \varphi \right) - K'_{01,0}\chi \right\}. \tag{3.18}$$

Straightforwardly substituting ψ into the first equation we obtain

$$B\chi = g\,, \tag{3.19}$$

with the compact operator $B : L^2(\Gamma_0) \to L^2(\Gamma_1)$, see [85], given by

$$B := S_{01,0} - S_{11,0}(I + K'_{11,0})^{-1} K'_{01,0}$$

and the right-hand side

$$g := 2u^i + S_{11,1}\varphi - S_{11,0}(I + K'_{11,0})^{-1}\left(2\,\frac{\partial u^i}{\partial \boldsymbol{\nu}_1} + K'_{11,1}\varphi - \varphi\right).$$

Then we applied the second Tikhonov regularization to regularize the eliminated version (3.19)

$$\alpha_2\chi + B^*B\chi = B^*g \tag{3.20}$$

where B^* is the adjoint of B. When the density χ is determined through Tikhonov regularization one can compute the density ψ from the equation (3.18). Once the unknown densities are found one can compute

$$u_0 = \frac{1}{2}\left(S_{10,0}\psi + S_{00,0}\chi\right) \quad \text{and} \quad \frac{\partial u_0}{\partial \boldsymbol{\nu}_0} = \frac{1}{2}\left(K'_{10,0}\psi + K'_{00,0}\chi - \chi\right) \quad \text{on } \Gamma_0. \tag{3.21}$$

Afterwards, in principle, for each point $x \in \Gamma_0$ we finally can read off the impedance function from (3.3) as

$$\eta = -ik_0\,\frac{u_0}{\partial u_0/\partial \boldsymbol{\nu}_0} \quad \text{on } \Gamma_0. \tag{3.22}$$

However, the reconstruction of the impedance from the equation (3.22) will be sensitive to errors in the normal derivative of u_0 in the vicinity of zero. To obtain more stable solutions, we express the unknown impedance function in terms of some basis functions κ_r, $r = 0, \pm 1, \pm 2, \ldots, \pm R$, as a linear combination

$$\eta = \sum_{r=-R}^{R} \tau_r \kappa_r \quad \text{on } \Gamma_0. \tag{3.23}$$

Then we satisfy (3.3) in a least squares sense, that is, we determine the coefficients $\tau_{-R}, \ldots, \tau_R$ in (3.23) such that for a set of grid points $\boldsymbol{x}_1, \ldots, \boldsymbol{x}_N$ on Γ_0 the least squares sum

$$\sum_{n=1}^{N} \left| u_0(\boldsymbol{x}_n) + \frac{1}{ik_0} \sum_{r=-R}^{R} \tau_r \kappa_r(\boldsymbol{x}_n)\,\frac{\partial u_0}{\partial \boldsymbol{\nu}_0}(\boldsymbol{x}_n) \right|^2 \tag{3.24}$$

is minimized. Here N is the discretization number and the number of basis functions R in (3.23) can be considered as some kind of additional regularization parameter where we use trigonometric functions of degree equal to R for the approximation of the impedance in (3.23).

We define a percentage error to demonstrate precisely the difference between the actual impedance functions and reconstructions as

$$ERR^{\eta} = 100\,\frac{\|\eta - \eta^{\star}\|}{\|\eta\|}\,, \tag{3.25}$$

where $\eta^{\star}$ denotes the reconstructed impedance function and η is the exact function.

3.4 Numerical Results

This section is devoted to the applicability of the reconstruction algorithm both for noisy and exact full/limited aperture, near-/far-field data by presenting some illustrative examples. In these examples, the integral equation systems are solved through the Nyström method with a discretization number $N = 64$. The integrals occuring in the near-field expression (2.59) and in the far-field expression (2.64) are evaluated numerically by using the trapezoidal rule. In all examples the regularization parameters α_1, α_2 and R are chosen by trial and error and to obtain noisy far-field $\tilde{u}_{\infty}$ equation (2.71) is used. Moreover we put tilde sign to the parameters obtained for noisy data.

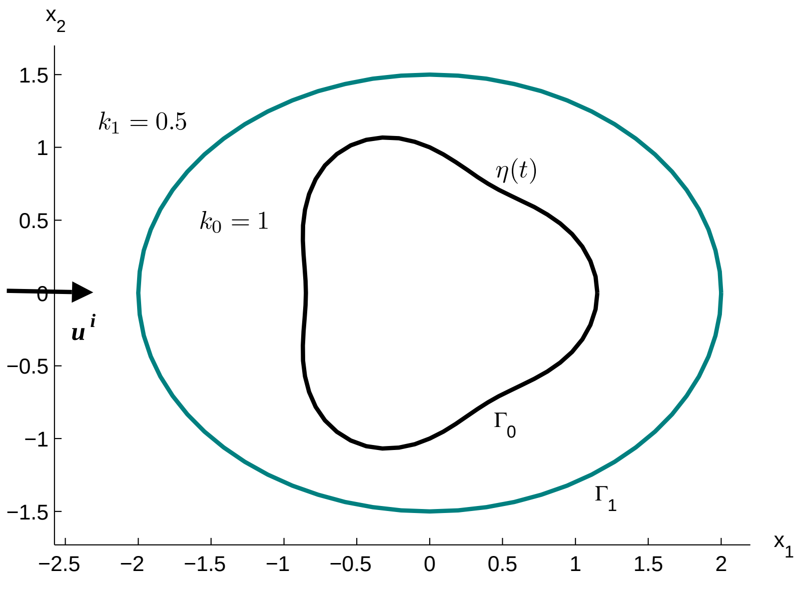

Figure 3.8: Rounded triangle – ellipse geometry

Experiment 1: In the first example, the shape of the impedance cylinder is chosen as a rounded triangular shaped scatterer $\Gamma_0 = 1/2\Gamma^{(t)}$, whereas the dielectric cylinder is an elliptic cylinder $\Gamma_1 = \Gamma^{(e)}$ with $e_0 = 2$, $e_1 = 1.5$. The wave numbers are chosen as $k_0 = 1$ and $k_1 = 0.5$ and the illumination angle is $\phi_0 = 0^\circ$ for both exact and noisy far-field data, see Figure 3.8. The noise ratio in the equation (2.71) is chosen $\delta = 0.03$. The impedance function over the boundary Γ_0 given as

$$\eta(z_0(t)) = \sin^4 \frac{t}{2} + i\cos^4 \frac{t}{2}, \quad t \in [0, 2\pi]. \tag{3.26}$$

For the exact data Tikhonov parameters are $\alpha_1 = 10^{-14}$, $\alpha_2 = 10^{-4}$ and for the noisy case, $\widetilde{\alpha}_1 = 10^{-3}$, $\widetilde{\alpha}_2 = 10^{-2}$ are chosen. The degree of the polynomial is $R = \widetilde{R} = 2$ both for the exact and noisy cases. We obtain $ERR^\eta \approx 1.117$ for the exact data and $\widetilde{ERR}^\eta \approx 11.571$ for the noisy data, see Figure 3.9.

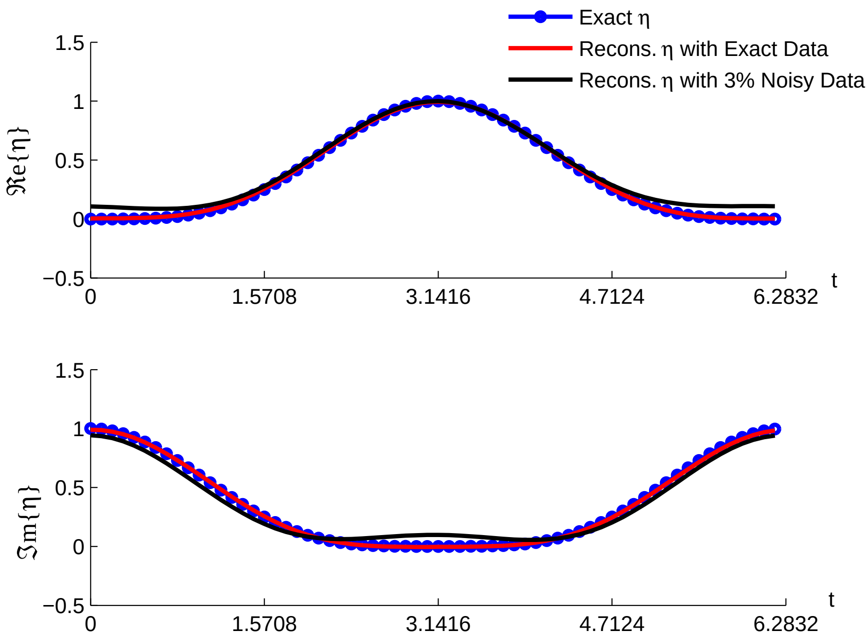

Figure 3.9: Reconstruction of the impedance (3.26) for a rounded triangular – ellipse geometry with full far-field data

Experiment 2: The second investigation of the problem configuration given in Figure 3.8 is the reconstruction of the impedance function (3.26) in the limited aperture case with far-field data given in the range of angle π. To this aim the far-field data is collected on 64 equidistant points over a semi circle Ω^m for $\phi \in [0, \pi]$. To obtain 3% noise level in data, $\delta = 0.03$ is chosen in the equation (2.71). Tikhonov parameters are chosen as $\alpha_1 = 10^{-12}$, $\alpha_2 = 10^{-4}$ and the degree of the polynomial is $R = 2$ for the exact data. In the noisy data case $\widetilde{\alpha}_1 = 10^{-4}$, $\widetilde{\alpha}_2 = 10^{-2}$ and the degree of the polynomial is $\widetilde{R} = 2$. We obtain $ERR^{\eta} \approx 3.167$ and $\widetilde{ERR}^{\eta} \approx 15.827$ with exact and noisy data, respectively, see Figure 3.10.

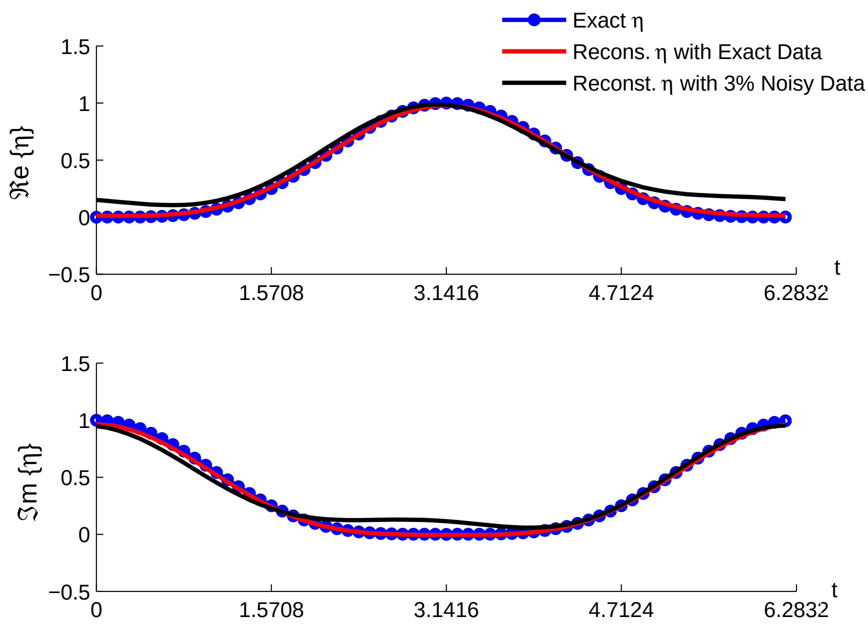

Figure 3.10: Reconstruction of the impedance (3.26) for a rounded triangular–ellipse geometry with far-field data given in the range of angle π

Experiment 3: In the following experiment we want to investigate the effect of the wave numbers on the reconstructions using the configuration in Figure 3.8 with full far-field data. We add complex contribution to the wave number $k_0 = 1 + i$ and keep $k_1 = 0.5$. Afterwards we reconstruct the impedance function with the regularization parameters $\alpha_1 = 10^{-12}$, $\alpha_2 = 10^{-4}$, $R = 2$ and obtain $ERR^{\eta} \approx 0.498$ for exact data. Then from the knowledge of 3% noisy data we choose $\widetilde{\alpha}_1 = 10^{-4}$, $\widetilde{\alpha}_2 = 10^{-2}$, $\widetilde{R} = 2$ and find the percentage error $\widetilde{ERR}^{\eta} \approx 26.317$, see Figure 3.11.

Experiment 4: Now we test the quality of the reconstructions on the upper approximate limits of the resonance region with exact full far-field data. Hence, real wave numbers are chosen as $k_0 = 5$, $k_1 = 4$ in the problem given in Figure 3.8. The regularization parameters $\alpha_1 = 10^{-14}$, $\alpha_2 = 10^{-8}$, $R = 2$ are chosen to reconstruct the impedance function. We obtain the percentage error as $ERR^{\eta} \approx 3.541$. As in the previous experiment we exchange the values of the wave numbers as $k_0 = 4$, $k_1 = 5$ and use the same regularization parameters. After that we obtain percentage error as $ERR^{\eta} \approx 6.686$, see Figure 3.12.

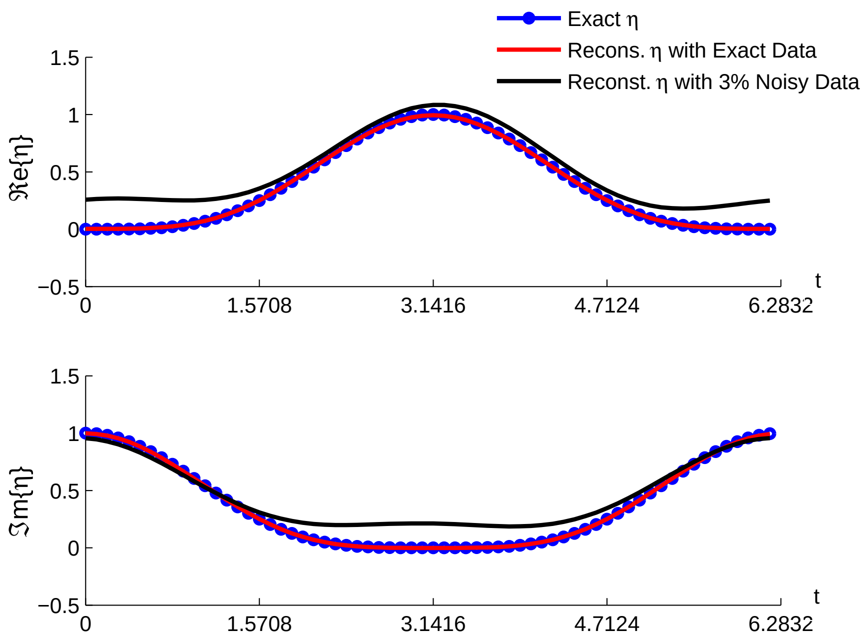

Figure 3.11: Reconstruction of the impedance (3.26) for a rounded triangular – ellipse geometry with full far-field exact data for complex valued k_0

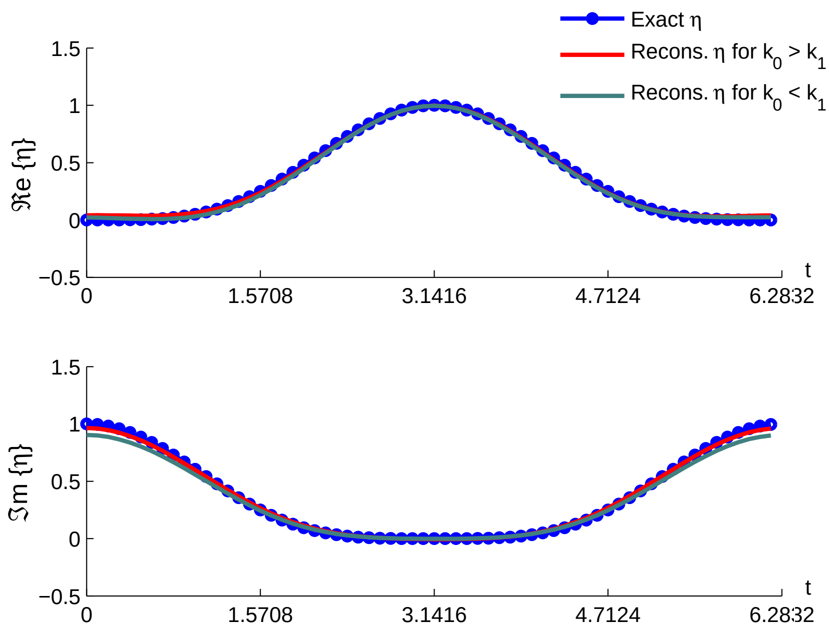

Figure 3.12: Reconstruction of the impedance (3.26) for a rounded triangular – ellipse geometry with full far-field exact data for high wave numbers

Experiment 5: The following experiment is performed by using the same problem configuration given in Figure 3.8 for observing the effect of the impedance function and the least squares regularization on the quality of the reconstructions by changing the impedance function as

$$\eta(z_0(t)) = \frac{8+2\sin t}{5+\cos t} + i\,\frac{4\cos t}{7-\sin t}, \qquad t \in [0, 2\pi]. \tag{3.27}$$

The parameters are $\alpha_1 = 10^{-12}$, $\alpha_2 = 10^{-4}$, $R = 2$ for exact far-field data and $\widetilde{\alpha}_1 = 10^{-3}$ $\widetilde{\alpha}_2 = 10^{-2}$, $\widetilde{R} = 1$ for noisy far-field data. We obtained $ERR^{\eta} \approx 1.277$ in exact data case and $\widetilde{ERR}^{\eta} \approx 5.061$ in noisy data case, see Figure 3.13.

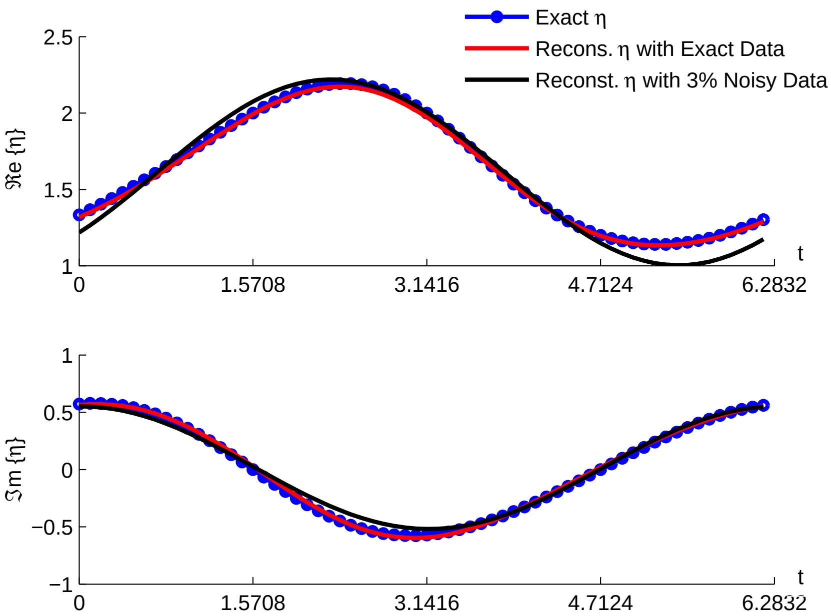

Figure 3.13: Reconstruction of the impedance (3.27) for a rounded triangular – ellipse geometry with full far-field data

Experiment 6: This experiment is devoted to compare the effect of the exterior cylinder's shape Γ_1, on the reconstructions. To this aim instead of ellipse in Figure 3.8 we use the dielectric medium bounded by a rounded rectangular contour $\Gamma_1 = 2\Gamma^{(r)}$ as given in Figure 3.14. The other parameters of the problem such as wave numbers k_0 and k_1, the impedance function η, the illumination angle ϕ_0 are taken the same as in the first example of this section. Here for the noisy far-field data case also 3% noise level is used. In the exact data case $\alpha_1 = 10^{-14}$, $\alpha_2 = 10^{-3}$, $R = 2$ and in the noisy data case $\widetilde{\alpha}_1 = 10^{-3}$, $\widetilde{\alpha}_2 = 10^{-2}$, and $\widetilde{R} = 1$ are chosen. Percentage errors obtained as $ERR^{\eta} \approx 6.448$ and $\widetilde{ERR}^{\eta} \approx 24.667$ for the exact and noisy cases, respectively, see Figure 3.15.

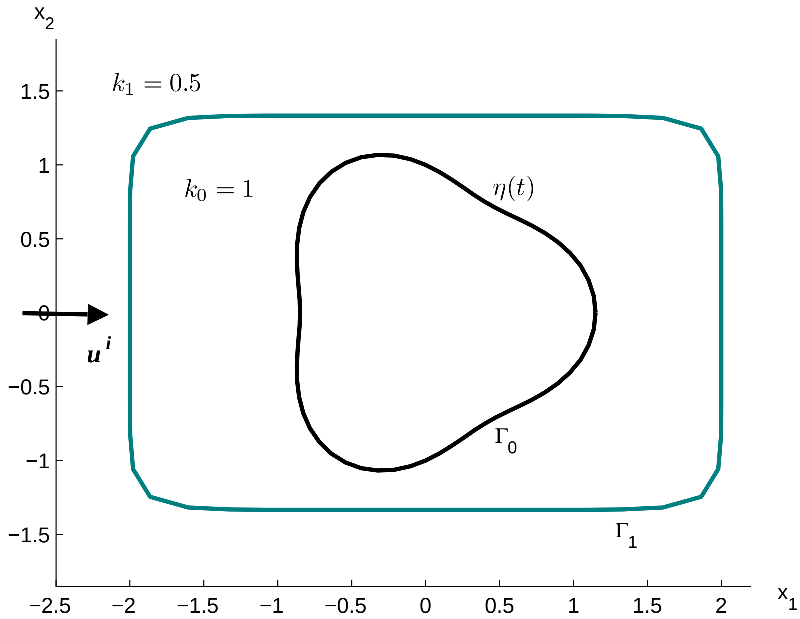

Figure 3.14: Rounded triangular – rounded rectangular geometry

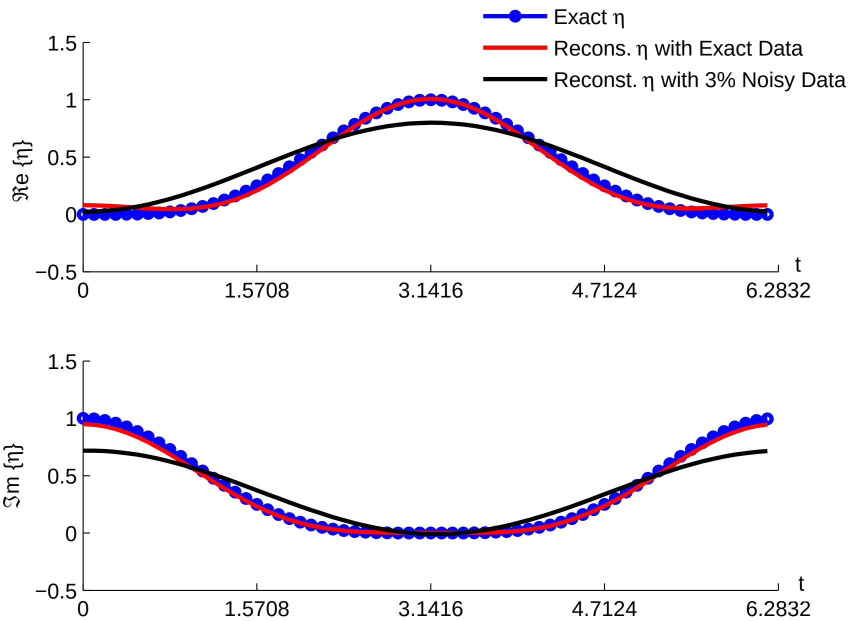

Figure 3.15: Reconstruction of the impedance (3.26) for a rounded triangle – rounded rectangle geometry with full far-field data

Experiment 7: For this experiment unlike the problem configuration in Figure 3.8 we replace the rounded triangular shaped buried obstacle by a circular object $\Gamma_0 = \Gamma^{(c)}$ having radius a $c_0 = 0.6$, see Figure 3.16. The aim of this replacement is to investigate the effect of the shape of the buried obstacle on the quality of the reconstructions. The unmentioned other parameters of the problem such as the wave numbers, the impedance function, the illumination angle etc. are chosen the same as in the previous experiment. The exact scattered full far-field is computed in 64 collocation points. The noisy far-field is obtained by adding 3% random noise to the exact far-field data.

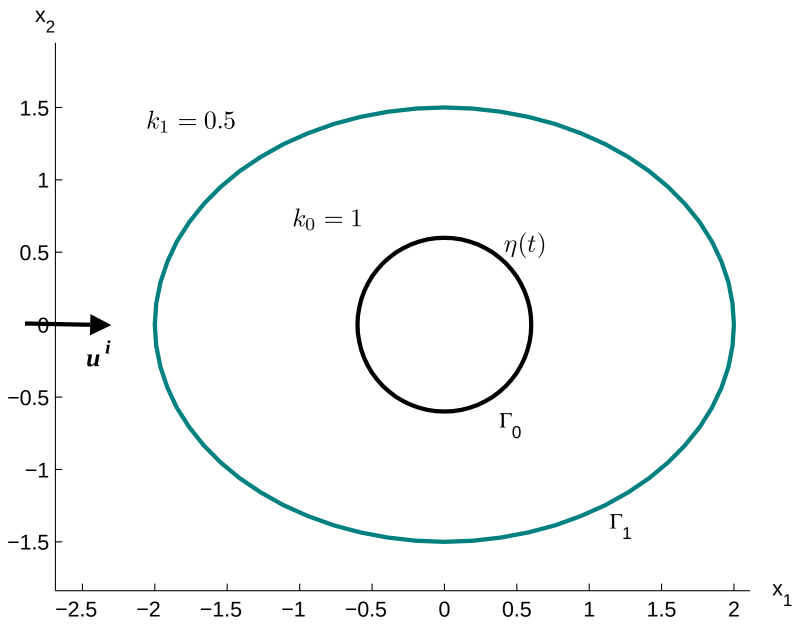

Figure 3.16: Ellipse – circle geometry

In order to find reasonable reconstructions Tikhonov regularization parameters are chosen as $\alpha_1 = 10^{-12}$, $\alpha_2 = 10^{-6}$ and $\widetilde{\alpha}_1 = \widetilde{\alpha}_2 = 10^{-3}$ for exact data and noisy data cases, respectively where the degree of the polynomial is $R = \widetilde{R} = 2$ for both cases. Percentage error in the exact data case $ERR^{\eta} \approx 1.486$ and in the noisy case is $\widetilde{ERR}^{\eta} \approx 7.071$ are obtained, see Figure 3.17.

We further shift the center coordinates of the Γ_0 to $O(0.5, 0.5)$ for testing the algorihtm when the impedance cylinder is not located at the center of the dielectric cylider. In the noise free case by choosing the parameters $\alpha_1 = 10^{-14}$, $\alpha_2 = 10^{-3}$, $R = 2$ we obtain $ERR^{\eta} \approx 8.093$ and for the noisy case we obtain $\widetilde{ERR}^{\eta} \approx 10.954$ percentage error with the regularization parameters $\widetilde{\alpha}_1 = 10^{-5}$, $\widetilde{\alpha}_2 = 10^{-2}$, $\widetilde{R} = 2$.

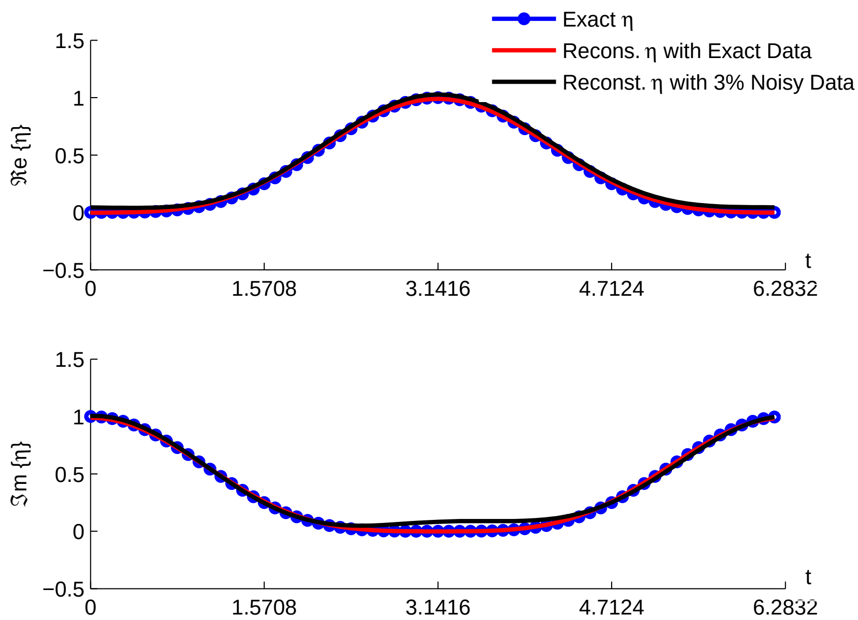

Figure 3.17: Reconstruction of the impedance (3.26) for a circle – ellipse geometry with full far-field data

Experiment 8: Now, we consider a peanut-shaped curve – ellipse geometry as given in Figure 3.18. The semi axes of the ellipse are $e_0 = 1.4$ and $e_1 = 1$. The wave number

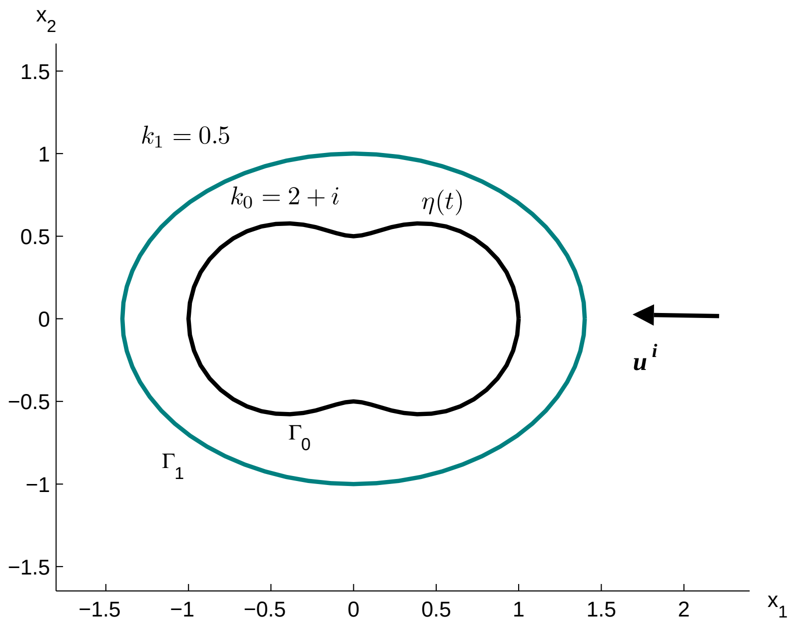

Figure 3.18: Peanut shaped – Ellipse geometry

of the domain D_0 is $k_0 = 2 + i$ and for the domain D_1 is $k_1 = 0.5$. The illumination angle is taken as $\phi_0 = 180°$. The inhomogeneous impedance function defined on Γ_0

has a rapidly varying real part and slowly varying imaginary part such that

$$\eta(z_0(t)) = 1.5 + \sin^3 t + i \sin t\,, \quad t \in [0, 2\pi]. \tag{3.28}$$

In the exact far-field data case regularization parameters are $\alpha_1 = 10^{-11}$, $\alpha_2 = 10^{-7}$ and in the noisy far-field data case $\widetilde{\alpha}_1 = 10^{-3}$, $\widetilde{\alpha}_2 = 10^{-3}$. Degree of the polynomials $R = \widetilde{R} = 3$ is chosen in both cases. Percentage errors are obtained as $ERR^{\eta} \approx 4.568$ and $\widetilde{ERR}^{\eta} \approx 26.200$ for the exact and the noisy cases, respectively, see Figure 3.19.

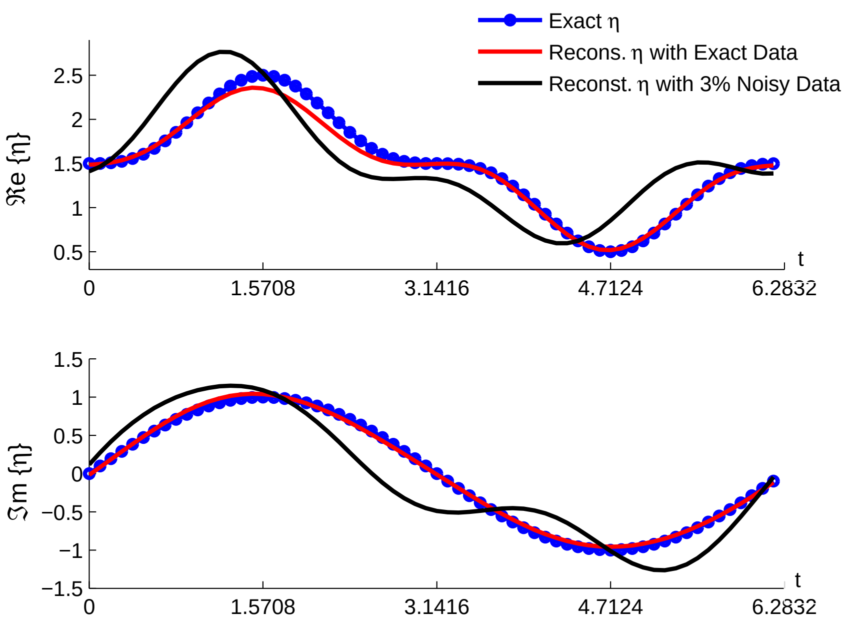

Figure 3.19: Reconstruction of the impedance (3.28) for a peanut-shaped curve – ellipse geometry with full far-field data

Experiment 9: In order to reconstruct the impedance function given in (3.28) more accurately using the problem configuration given in Figure 3.18 we apply full near-field data. To this aim the scattered field given with the integral representation in (2.59) is computed on a meauserement circle having radius $c_0 = 2$. Then we follow the same reconstruction algorithm described for the far-field in the Section 3.3 just using near-field data instead of far-field. The Tikhonov regularization parameters for the exact data $\alpha_1 = 10^{-9}$, $\alpha_2 = 10^{-10}$ and for the noisy data $\widetilde{\alpha}_1 = \widetilde{\alpha}_2 = 10^{-3}$ are chosen. Degrees of the polynomials are chosen $R = \widetilde{R} = 3$ for both exact and noisy data cases. We obtain percentage errors $ERR^{\eta} \approx 0.544$ and $\widetilde{ERR}^{\eta} \approx 23.852$ for exact and noisy cases, see Figure 3.20.

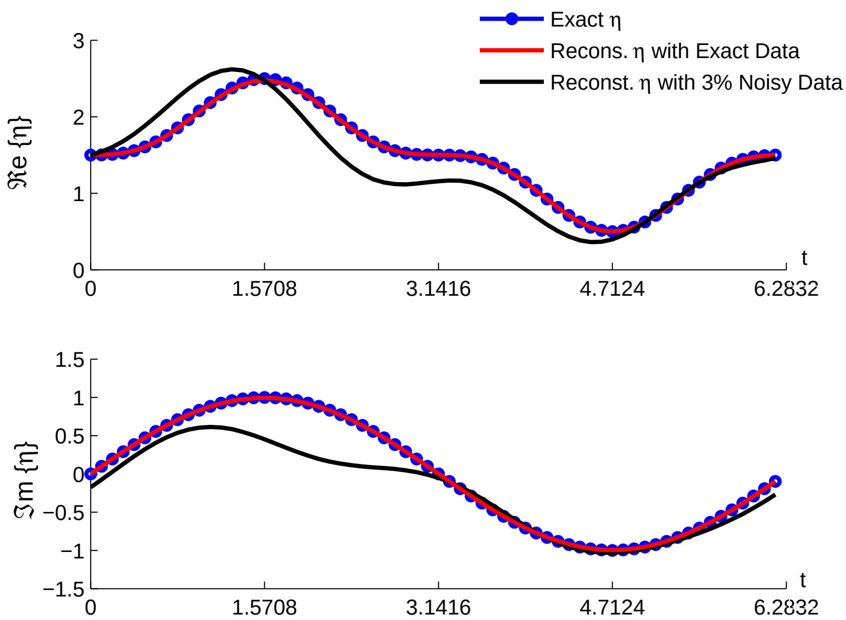

Figure 3.20: Reconstruction of the impedance (3.28) for a peanut-shaped curve – ellipse geometry with full near-field data

Experiment 10: In the final example we force the proposed method for the reconstruction of the impedance function

$$\eta(z_0(t)) = 1.5 - \cos t + 0.5\sin 2t + i\frac{\cos t}{3 - 2\cos t}, \quad t \in [0, 2\pi], \tag{3.29}$$

from the full near-field measurements choosing some complex shaped cylinders. To

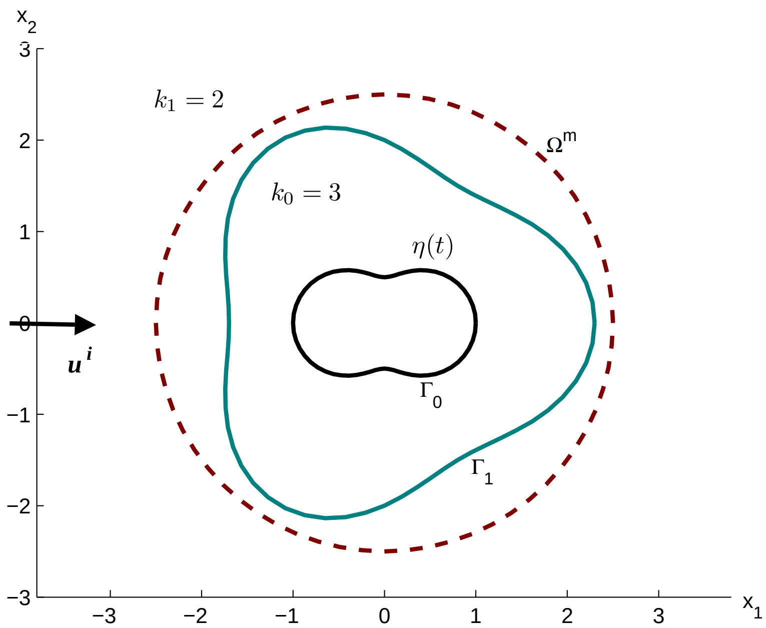

Figure 3.21: Rounded triangle – peanut-shaped curve geometry

this aim we choose $\Gamma_0 = \Gamma^{(p)}$ and $\Gamma_1 = \Gamma^{(t)}$ with the wave numbers $k_0 = 3$ and $k_1 = 2$. As it can be seen from the Figure 3.21 scatterers are illuminated by a plane wave with the incident angle $\phi_0 = 0$. The near-field is computed on a measurement circle Ω^m with a radius $c_0 = 2.5$.

In this experiment Tikhonov regularization parameters are chosen as $\alpha_1 = 10^{-9}$, $\alpha_2 = 10^{-5}$ for the exact data, $\widetilde{\alpha}_1 = 10^{-6}$, $\widetilde{\alpha}_2 = 10^{-2}$ for noisy data computations. For both cases $R = \widetilde{R} = 2$. The percentage error for the exact data case is $ERR^{\eta} \approx 5.666$ and for the noisy data case $\widetilde{ERR}^{\eta} \approx 28.516$, see Figure 3.22.

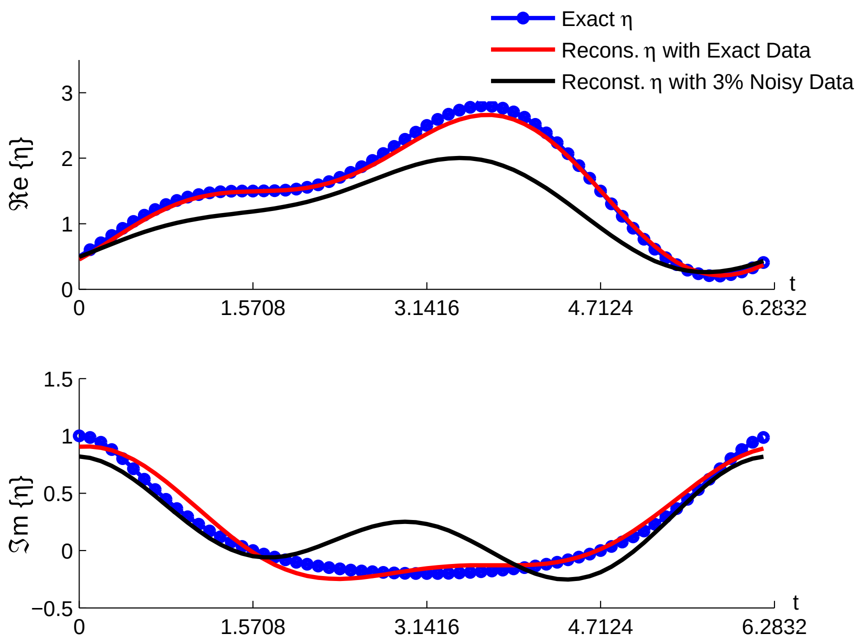

Figure 3.22: Reconstruction of the impedance (3.29) for a rounded triangle–peanut shaped geometry with full near-field data

3.5 Comments on Numerical Results

The applicability and the effectiveness of our method is supported by the numerical results given in the Section 3.4. In this part we summarize our experiences from numerical experiments. We should note that due to the ill-posedness of the problem some difficulties appear to generalize our results for all cases.

As to be expected, full exact data yield better reconstructions than limited aperture exact data or full noisy data. And we observed that if the noise level exceeds 3%–4% for full far-field data then the reconstructions start to deteriorate.

We can reconstruct the impedance function in the limited aperture case with exact/noisy data given in the range of angle π but we do not have an unique result on which measurement region (shadowed or illuminated) always gives the best reconstructions. However we have an opinion that when the scattered field is collected on the shadow region one can generally obtain more accurate reconstructions.

Additionally, for the exact data we need smaller Tikhonov regularization parameters however for the noisy case we need stronger regularization parameters, [85]. The degrees of the polynomials are generally higher or at least equal to the degrees of the polynomials appearing in noisy data case. We also observed that in order to reconstruct rapidly varying impedance functions one has to choose higher degree of the polynomials. Furthermore, accurate reconstructions can be obtained for the impedance functions that can be expressed by terms of proper basis functions.

We also observed that in the noise free case we can reconstruct the impedance function for smooth boundaries very accurately however non-smooth parts of the boundaries cause oscillations in the scattered field and this mechanism deteriorates the reconstructions especially in the noisy case. Moreover for noisy data a small perturbation on the shape of the dielectric cylinder effects the accuracy of the reconstruction significantly. On the other hand, the shape of the impedance cylinder does not effect the reconstructions as much as the shape of the dielectric cylinder. It is obvious that the illumination angle also effects the reconstructions depending on the geometry of the scatterers and the type of impedance functions.

Concerning the influence of the wave numbers the quality of the reconstructions deteriorated when k_0 and k_1 were increased simultaneously since in such case they also caused rapid oscillations in the scattered field. Roughly speaking for real valued wave numbers the sum $k_0 + k_1$ should not exceed a certain threshold, for example 12 to obtain satisfactory reconstructions. Furthermore, we observed that increasing k_1 had stronger effect on the reconstructions than increasing k_0. We can also reconstruct both for $|k_0| > k_1$ and $|k_0| < k_1$, and there is no any general rule for every case which condition yields better results.

4. LOCATION AND SHAPE RECONSTRUCTIONS

In this chapter, an integral equation based method for the solutions of two-dimensional location and shape reconstruction problems of perfectly electric conductors buried in arbitrarily shaped dielectric cylinders is presented, [89]. This investigation is an extension study of [56] which was devoted for the shape reconstructions of acoustically sound-soft obstacles in free space by Kress in 2003. Generalized version of the buried shape reconstruction problem was studied by Yaman and Yapar in 2008 for the sound-soft obstacles located in penetrable cylinders having conductive boundary condition on their surface, see [88].

4.1 Statement of the Direct Problem

Here, the direct problem is to obtain the scattered near-/far-field when the configuration given in Figure 4.1 is illuminated by a single time-harmonic electromagnetic plane wave. As it is mentioned in Chapter 2, the total fields (u_0, u_1) satisfy the homogeneous Helmholtz equation and additionally for this problem it is considered that u_0 and u_1

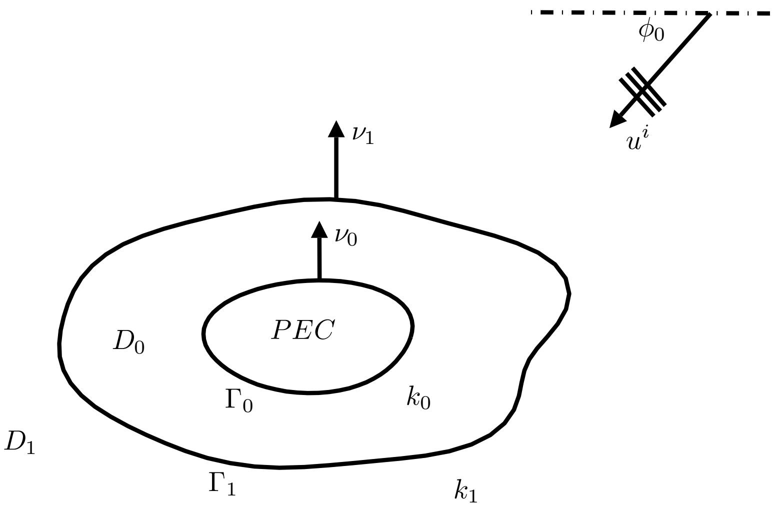

PEC : Perfectly electric conductor

Figure 4.1: Geometry of the buried location and shape reconstruction problem

have to satisfy the transmission conditions

$$u_0 = u_1 \qquad \text{on} \quad \Gamma_1\,, \tag{4.1}$$

$$\frac{\partial u_1}{\partial \boldsymbol{\nu}_1} = \frac{\partial u_0}{\partial \boldsymbol{\nu}_1} \qquad \text{on} \quad \Gamma_1\,, \tag{4.2}$$

and the Dirichlet boundary condition

$$u_0 = 0 \quad \text{on}\, \Gamma_0\,. \tag{4.3}$$

We use the same integral representations of the scattered field u^s (2.59), and the interior total field u_0 (2.60), in order to follow the proposed potential approach for the solution of the direct problems in the thesis. Afterwards, one can derive the following integral equation system (4.4)-(4.6) in the operator form by substituting resultant expressions (3.6)-(3.10) of the fields u^s and u_0 and their normal derivatives $\partial u^s/\partial \boldsymbol{\nu}_1$ and $\partial u_0/\partial \boldsymbol{\nu}_j$ $(j = 0,1)$ on the boundaries Γ_1 and Γ_0 to the transmission and the Dirichlet conditions under the jump relations [43] for the densities ψ, $\varphi \in C(\Gamma_1)$ and $\chi \in C^{0,\beta}(\Gamma_0)$:

$$2\psi + K_{11,1}\psi - K_{11,0}\psi + S_{11,1}\varphi - S_{11,0}\varphi - S_{01,0}\chi = -2u^i|_{\Gamma_1}\,, \tag{4.4}$$

$$2\varphi - T_{11,1}\psi + T_{11,0}\psi - K^{'}_{11,1}\varphi + K^{'}_{11,0}\varphi + K^{'}_{01,0}\chi = 2\frac{\partial u^i}{\partial \boldsymbol{\nu}_1}|_{\Gamma_1}\,, \tag{4.5}$$

$$K_{10,0}\psi + S_{10,0}\varphi + S_{00,0}\chi = 0\,. \tag{4.6}$$

To write the integral equation system in a shorter form we introduce the operator A_2 as,

$$A_2 := \begin{pmatrix} K_{11,1} - K_{11,0} & S_{11,1} - S_{11,0} & -S_{01,0} \\ -T_{11,1} + T_{11,0} & -K^{'}_{11,1} + K^{'}_{11,0} & K^{'}_{01,0} \\ K_{10,0} & S_{10,0} & 0 \end{pmatrix}, \tag{4.7}$$

which is compact from $C(\Gamma_1) \times C(\Gamma_1) \times C^{0,\beta}(\Gamma_0)$ into $C(\Gamma_1) \times C(\Gamma_1) \times C^{1,\beta}(\Gamma_0)$. Finally, one can obtain straightforwardly

$$(E_2 + A_2)\begin{pmatrix} \psi \\ \varphi \\ \chi \end{pmatrix} = 2\begin{pmatrix} -u^i|_{\Gamma_1} \\ \partial u^i/\partial \boldsymbol{\nu}_1|_{\Gamma_1} \\ 0 \end{pmatrix}. \tag{4.8}$$

Here, $E_2 = \begin{pmatrix} 2I & 0 & 0 \\ 0 & 2I & 0 \\ 0 & 0 & S_{00,0} \end{pmatrix}$ and I is the identity operator.

Provided k_0^2 is not a Dirichlet eigenvalue for the negative Laplacian for the interior of Γ_0 the operator $E_2 : C(\Gamma_1) \times C(\Gamma_1) \times C^{0,\beta}(\Gamma_0) \to C(\Gamma_1) \times C(\Gamma_1) \times C^{1,\beta}(\Gamma_0)$ is boundedly invertible, see [43, 89, 98]. In this context, for the solution of the direct scattering problem one can obtain values of ψ, φ and χ solving the system given (4.8) by using parametrized forms of the operators as defined in (2.22) - (2.25). Then we substitute values of the corresponding densities ψ and φ to the near- (2.61) or far-field expressions (2.64).

4.2 Numerical Examples for the Direct Problem

As a first task, we check our numerical results with the results published in Chapter 3.5 of the book [43] obtained for the direct scattering problems for sound-soft kite-shaped obstacle in free space. To this aim in order to reduce our buried problem to the free

Table 4.1: Comparison of the far fields for kite-shaped object

k = 1	$Re\, u_\infty(\boldsymbol{d})$	$Im\, u_\infty(\boldsymbol{d})$	$Re\, u_\infty(\boldsymbol{-d})$	$Im\, u_\infty(\boldsymbol{-d})$
$N = 16$	-1.62642413	0.60292714	1.39015283	0.09425130
	-1.62747117	**0.60232982**	**1.3973655**	**0.09444753**
$N = 32$	-1.62745909	0.60222343	1.39696610	0.09499454
	-1.62745744	**0.60222583**	**1.39694464**	**0.09499722**
$N = 64$	-1.62745750	0.60222591	1.39694488	0.09499635
	-1.62745750	**0.60222591**	**1.39694488**	**0.09499635**
$N = 128$	-1.62745750	0.60222591	1.39694488	0.09499635
	-1.62745750	**0.60222591**	**1.39694488**	**0.09499635**
k = 5				
$N = 16$	-2.30969119	1.52696566	-0.30941096	0.11503232
	-5.19698108	**-0.64126716**	**2.15189340**	**9.75100510**
$N = 32$	-2.46524869	1.67777368	-0.19932343	0.006213859
	-2.43899238	**1.68880724**	**-2.23630143**	**1.61986696**
$N = 64$	-2.47554379	1.68747937	-0.19945788	0.06015893
	-2.47554379	**1.68747937**	**-0.19945787**	**0.06015893**
$N = 128$	-2.47554380	1.68747937	-0.19945787	0.06015893
	-2.47554380	**1.68747937**	**-0.19945787**	**0.06015893**

space scattering problem interior and exterior media's wave numbers are chosen equal to each other, $k_0 = k_1$. In Table 4.1, first results are taken from the reference book and second results (with bold text) are the results of our reduced problem. Note that, the same notation with the Table 3.1 was used for filling in the Table 4.1.

We also checked the speed of convergence for the direct problem of the buried location and shape reconstruction problem and as to be expected we obtained exponential convergence as illustrated in Table 4.2

Table 4.2: Numerical example for the direct problem of the buried location and shape reconstruction problem

Parameters:	N	$Re\,u_\infty(\boldsymbol{d})$	$Im\,u_\infty(\boldsymbol{d})$	$Re\,u_\infty(\boldsymbol{-d})$	$Im\,u_\infty(\boldsymbol{-d})$
$\Gamma_0 = \Gamma^{(k)}, \Gamma_1 = \Gamma^{(t)}$	16	-0.53619473	0.73675149	-1.42210259	0.27093718
	32	-0.53132059	0.74263838	-1.42129139	0.27069367
$k_0 = 1$	64	-0.53135246	0.74267923	-1.42130750	0.27069526
$k_1 = 0.5$	128	-0.53135246	0.74267923	-1.42130750	0.27069526
$\Gamma_0 = \Gamma^{(a)}, \Gamma_1 = \Gamma^{(e)}$	16	0.21775559	-1.37160049	-1.09666475	0.87098060
$(e_0 = 2, e_1 = 1)$	32	0.21591560	-1.36906355	-1.09534860	0.87212500
$k_0 = 2$	64	0.21590728	-1.36906771	-1.09534764	0.87213129
$k_1 = 1$	128	0.21590728	-1.36906771	-1.09534764	0.87213129
$\Gamma_0 = \Gamma^{(c)}, \Gamma_1 = \Gamma^{(s)}$	16	2.78840272	0.13660773	-2.84918578	3.90003567
$(c_0 = 1)$	32	1.05153369	-0.18440367	-1.21793150	2.70373056
$k_0 = 3$	64	1.05334053	-0.18258264	-1.22653632	2.69742747
$k_1 = 2.5$	128	1.05334053	-0.18258264	-1.22653632	2.69742747
$\Gamma_0 = \Gamma^{(e)}, \Gamma_1 = \Gamma^{(p)}$	16	0.10110573	0.30673926	-0.51244663	0.11644543
$(e_0 = 0.6, e_1 = 0.2)$	32	0.10161683	0.30681371	-0.51241822	0.11628211
$k_0 = 4$	64	0.10161687	0.30681372	-0.51241815	0.11628214
$k_1 = 3$	128	0.10161687	0.30681372	-0.51241815	0.11628214
$\Gamma_0 = \Gamma^{(a)}, \Gamma_1 = \Gamma^{(t)}$	16	0.27371664	-0.32228414	-1.78527484	0.81115483
	32	0.27809585	-0.26053866	-1.79632363	0.91924869
$k_0 = 2+2i$	64	0.27806917	-0.26055399	-1.79634711	0.91925606
$k_1 = 1$	128	0.27806917	- 0.26055399	-1.79634711	0.91925606
$\Gamma_0 = \Gamma^{(p)}, \Gamma_1 = \Gamma^{(c)}$	16	0.40933655	2.13452599	-1.49884641	0.54799403
$(c_0 = 2)$	32	0.40935359	2.13448292	-1.49884226	0.54800297
$k_0 = 1+i$	64	0.40935359	2.13448292	-1.49884226	0.54800297
$k_1 = 0.5+0.5i$	128	0.40935359	2.13448292	-1.498842266	0.54800297

Finally we compare our results with Method of Moments (MoM) as mentioned in Section 3.2 via omitting the buried PEC scatterer from the problem configuration in Figure 4.1.

Moreover, assuming $\eta = 0$ for the buried impedance problem investigated in Chapter 3 and the problem considered here yields the same results for the same ϕ_0, k_0, k_1 and Γ_0, Γ_1 since the integral representation of the fields and the solution methodology are the same both for two problems.

4.3 Inverse Problem

The aim of the inverse problem is to find the shape as well as the location of the buried scatterer from the limited/full far-field measurements via linearized Newton iterations. For this, we propose a new reconstruction algorithm to recover 2-D shape and location of a PEC obstacle which is buried in an arbitrarily shaped dielectric cylinder.

Our method consists of two main iterative parts and the aim of the first part is the reconstruction of the location of the buried object. Then by using this location information we focus on the shape reconstruction which is based on the minimization of a spatial difference between exact and updated shapes by least squares approximation. Therefore we choose an initially guessed boundary in the interior domain of the penetrable cylinder and define a density on it. The two additional densities stay on the boundary of the exterior cylinder. The scattered and the interior total fields are represented by using single-layer potentials the density which stays over the penetrable layer is reconstructed from the solution of the first kind integral equation for the given far-field via Tikhonov regularization. The values of the other two unknown densities are calculated by applying second Tikhonov regularization to the equation obtained from transmission conditions which ensure the continuity of the total fields and their derivatives across the boundary. Once all the density functions are known, one can compute the total fields in every region. It is already known from the definition of the problem that the buried obstacle is perfect electric conductor therefore the interior total field has to satisfy the Dirichlet boundary condition on the boundary of the obstacle. We use this condition for finding iteratively a new update of the location of the buried obstacle.

For the shape reconstruction we employ first degree Taylor expansion of the interior field over the updated boundary and compute an update function where it remains analytic for analytic boundaries [61]. This function is used for the correction of the updated boundary and iterations are continued until the defined stopping-criteria's are fulfilled.

Firstly, an arbitrarily shaped smooth boundary $\Gamma^{(0)}$ in the domain D_0 with the center coordinates $d_1^{(0)}$ and $d_2^{(0)}$ is considered as an initial guess having a star-like parametrization such that

$$\Gamma^{(0)} = \left\{ z^{(0)}(t) = (d_1^{(0)} + r(t)\cos t, d_2^{(0)} + r(t)\sin t) : t \in [0, 2\pi] \right\}, \qquad \textbf{(4.9)}$$

where r is a smooth 2π-periodic function. Then, we set $j = 0$ in the first iteration and in order to avoid an inverse crime we represent the fields by using only single-layer potentials as

$$u^s(\boldsymbol{x}) = \int_{\Gamma_1} \Phi_1(\boldsymbol{x},\boldsymbol{y})\,\varphi(\boldsymbol{y})\,ds(\boldsymbol{y}), \quad \boldsymbol{x} \in D_1, \tag{4.10}$$

$$u_0^{(j)}(\boldsymbol{x}) = \int_{\Gamma_1} \Phi_0(\boldsymbol{x},\boldsymbol{y})\,\psi^{(j)}(\boldsymbol{y})\,ds(\boldsymbol{y}) + \int_{\Gamma^{(j)}} \Phi_0(\boldsymbol{x},z)\,\chi^{(j)}(z)\,ds^{(j)}(z), \quad \boldsymbol{x} \in D_0. \tag{4.11}$$

At this point, to express the asymptotic behavior of the single layer potential, the far-field operator is introduced by $S_\infty : L^2(\Gamma_1) \to L^2(\Omega)$

$$(S_\infty \varphi)(\boldsymbol{x}) := \gamma \int_{\Gamma_1} e^{-ik_1 \boldsymbol{x}\cdot\boldsymbol{y}}\,\varphi(\boldsymbol{y})\,ds(\boldsymbol{y}), \qquad \boldsymbol{x} \in \Omega, \tag{4.12}$$

where $\gamma = e^{i\pi/4}/\sqrt{8\pi k_1}$. We observe that the far-field pattern for the solution of the inverse scattering problem is

$$u_\infty = S_\infty \varphi, \tag{4.13}$$

and the operator in this equation has an analytic kernel therefore it is severely ill-posed. Hence a regularization technique has to be applied to get a stable solution for the density $\varphi \in L^2(\Gamma_1)$. Along the line we apply the Tikhonov regularization as given in (3.16) in chapter 3 with a positive parameter α_1. Construction of the density φ allows us to compute the scattered field u^s in (4.10) and for a given scattered field the total field $u_0^{(j)}$ in (4.11) which satisfies transmission conditions (4.1) on Γ_1 via jump relations provided that the densities solve the system of integral equations

$$\begin{aligned} &S_{11,0}\psi^{(j)} + S_{(j)1,0}\chi^{(j)} = 2u^i|_{\Gamma_1} + S_{11,1}\varphi \\ &K'_{11,0}\psi^{(j)} + \psi^{(j)} + K'_{(j)1,0}\chi^{(j)} = 2\frac{\partial u^i}{\partial \boldsymbol{\nu}_1}\Big|_{\Gamma_1} + K'_{11,1}\varphi - \varphi. \end{aligned} \tag{4.14}$$

In the resultant equation system we eliminate the density $\psi^{(j)}$ from (4.14) to get

$$B^{(j)}\chi^{(j)} = g, \tag{4.15}$$

with the compact operator $B^{(j)} : L^2(\Gamma^{(j)}) \to L^2(\Gamma_1)$ given by

$$B^{(j)} := (I + K'_{11,0})\,S_{11,0}^{-1}S_{(j)1,0} - K'_{(j)1,0}$$

and the right-hand side

$$g := (I + K'_{11,0})\,S_{11,0}^{-1}(2u^i + S_{11,1}\varphi) - \left\{ 2\frac{\partial u^i}{\partial \boldsymbol{\nu}_1}\Big|_{\Gamma_1} + (K'_{11,1} - I)\varphi \right\}.$$

Here, we interpret the operator $S_{11,0}$ as a bounded operator from $L^2(\Gamma_1)$ into the Sobolev space $H^1(\Gamma_1)$ that has a bounded inverse provided k_0^2 is not a Dirichlet eigenvalue for the negative Laplacian for the interior of Γ_1 (see Theorem 3.6 in [43]). The equation system (4.15) is ill-posed and as a remedy we employ Tikhonov regularization using the following approximate equation

$$\alpha_2 \chi^{(j)} + B^{*(j)} B^{(j)} \chi^{(j)} = B^{*(j)} g, \tag{4.16}$$

instead of (4.15). Here α_2 is a positive parameter and $B^{*(j)} : L^2(\Gamma_1) \to L^2(\Gamma^{(j)})$ is the adjoint of $B^{(j)}$. Then substituting the density $\chi^{(j)}$ in the equation,

$$\psi^{(j)} = S_{11,0}^{-1}(2u^i + S_{11,1}\varphi - S_{(j)1,0}\chi^{(j)}), \tag{4.17}$$

one can obtain the density $\psi^{(j)}$ straightforwardly.

As the next step the interior total field and its normal derivative on the boundary $\Gamma^{(j)}$ can be computed through the jump relations by using the values of the densities $\psi^{(j)}$ and $\chi^{(j)}$, i.e.

$$u_0^{(j)}(\boldsymbol{x}) = \int_{\Gamma_1} \Phi_0(\boldsymbol{x},\boldsymbol{y})\, \psi^{(j)}(\boldsymbol{y})\, ds(\boldsymbol{y}) + \int_{\Gamma^{(j)}} \Phi_0(\boldsymbol{x},z)\, \chi^{(j)}(z)\, ds^{(j)}(z), \quad \boldsymbol{x} \in \Gamma^{(j)}, \tag{4.18}$$

and

$$\begin{aligned} \frac{\partial u_0^{(j)}}{\partial \boldsymbol{\nu}^{(j)}}(\boldsymbol{x}) &= \int_{\Gamma_1} \frac{\partial \Phi_0(\boldsymbol{x},\boldsymbol{y})}{\partial \boldsymbol{\nu}_1(\boldsymbol{x})}\, \psi^{(j)}(\boldsymbol{y})\, ds(\boldsymbol{y}) + \\ &+ \int_{\Gamma^{(j)}} \frac{\partial \Phi_0(\boldsymbol{x},z)}{\partial \boldsymbol{\nu}^{(j)}(\boldsymbol{x})}\, \chi^{(j)}(z)\, ds^{(j)}(z) - \frac{1}{2}\chi^{(j)}(\boldsymbol{x}), \quad \boldsymbol{x} \in \Gamma^{(j)}. \end{aligned} \tag{4.19}$$

We are now in a position to introduce the location identification parameters $\ell_1^{(j)}$ and $\ell_2^{(j)}$ for finding the actual location of the buried obstacle by updating the initially guessed center coordinates $(d_1^{(0)}, d_2^{(0)})$ in the form of

$$d_q^{(j+1)} = d_q^{(j)} + \ell_q^{(j)}, \quad q = 1,2. \tag{4.20}$$

These parameters can be obtained iteratively from the equation arising from the Dirichlet boundary condition,

$$u_0^{(j)} \circ \boldsymbol{z}^{(j)} + \sum_{q=1}^{2} \left\{ \operatorname{grad} u_0^{(j)} \circ \boldsymbol{z}^{(j)} \cdot \boldsymbol{e}_q \right\} \ell_q^{(j)} = 0 \quad \text{on} \quad \Gamma^{(j)}, \quad j = 0,1,\ldots,J_1, \tag{4.21}$$

where $\boldsymbol{e}_1 = (1,0), \boldsymbol{e}_2 = (0,1)$ are global unit vectors and the gradient of the interior total field is computed as the summation of the partial derivatives of $u_0^{(j)}$ along the normal and the tangential directions, to $\Gamma^{(j)}$ such that

$$\operatorname{grad} u_0^{(j)} \circ \boldsymbol{z}^{(j)} = \frac{\partial u_0^{(j)}}{\partial \boldsymbol{\nu}^{(j)}} \boldsymbol{\nu}^{(j)} \circ \boldsymbol{z}^{(j)} + \frac{\partial u_0^{(j)}}{\partial \boldsymbol{\tau}^{(j)}} \boldsymbol{\tau}^{(j)} \circ \boldsymbol{z}^{(j)} . \tag{4.22}$$

The new derivative expression appears in the right hand side of (4.22) is computed through the approximation [44]

$$\frac{\partial u_0^{(j)}}{\partial \boldsymbol{\tau}^{(j)}} (\boldsymbol{z}^{(j)}(t)) = \sum_{m=0}^{N} u_0^{(j)} (\boldsymbol{z}^{(j)}(t)) \, L_m'(t) , \quad t \in [0, 2\pi] , \tag{4.23}$$

where

$$L_m'(t) = \frac{1}{2m} \left\{ m \cos m(t - t_m) \cot \left(\frac{t - t_m}{2} \right) - \frac{\frac{1}{2} \sin m \, (t - t_m)}{\sin^2 \left(\frac{t - t_m}{2} \right)} \right\} .$$

The $(j+1)^{th}$ iteration starts by solving (4.16) with the updated location parameters and the last iteration J_1 will be obtained when a defined stopping criteria (SC_1)

$$SC_1 = \sum_{q=1}^{2} |d_q^{(j)} - d_q^{(j-1)}| < \bar{\varepsilon}_1 , \tag{4.24}$$

is fulfilled by choosing $\bar{\varepsilon}_1$ sufficiently small. As a first result we obtain shifted form of the initially guessed boundary $\Gamma^{(0)}$ to the approximate center coordinates of the buried obstacle such that

$$\Gamma^{(J_1)} = \left\{ \boldsymbol{z}^{(J_1)}(t) = (d_1^{(J_1)} + r(t) \cos t, \, d_2^{(J_1)} + r(t) \sin t) : t \in [0, 2\pi] \right\} . \tag{4.25}$$

We carry on the inversion algorithm with the solution of an equation which can be considered as a Taylor expansion of the $u_0^{(j)}$ over the boundary $\Gamma^{(j)}$ given as

$$u_0^{(j)} \circ \boldsymbol{z}^{(j)} + \left\{ \operatorname{grad} u_0^{(j)} \circ \boldsymbol{z}^{(j)} \cdot \boldsymbol{e} \right\} h^{(j)} = 0 \quad \text{on} \quad \Gamma^{(j)} , \quad j = J_1, J_1 + 1, \ldots, J_2 . \tag{4.26}$$

Here a new update function $h^{(j)}$ is defined to correct the initial guessed curve in every iteration via

$$\Gamma^{(j+1)} = \left\{ \boldsymbol{z}^{(j+1)}(t) = \boldsymbol{z}^{(j)}(t) + h^{(j)}(t) \boldsymbol{e}(t) : t \in [0, 2\pi] \right\} , \tag{4.27}$$

where $e(t) = (\cos t, \sin t)$ denotes the unit normal vector to the initial guess chosen as a circle and h is a sufficiently small 2π-periodic function.

As to be expected, the reconstruction of the update function with the equation (4.26) will be sensitive to errors in the term

$$\left\{ \operatorname{grad} u_0^{(j)} \circ \boldsymbol{z}^{(j)} \cdot \boldsymbol{e} \right\}$$

in the vicinity of zeros. To obtain more stable solutions we express the unknown update function in terms of trigonometric polynomials

$$h^{(j)}(t) = \sum_{m=0}^{M} a_m^{(j)} \cos mt + b_m^{(j)} \sin mt \,, \quad t \in [0, 2\pi] \,. \tag{4.28}$$

Then we satisfy the equation (4.26) in the least squares sense, that is, we determine the coefficients $(a_m^{(j)}, b_m^{(j)})$ in (4.28) such that for N collocation points $t_1, t_2, t_3, \cdots, t_N$ the least squares sum

$$\sum_{n=1}^{N} \left| u_0^{(j)}(\boldsymbol{z}^{(j)}(t_n)) + \left\{ (\operatorname{grad} u_0^{(j)} \circ \boldsymbol{z}^{(j)})(t_n) \cdot \boldsymbol{e}(t_n) \right\} \sum_{m=0}^{M} (a_m^{(j)} \cos mt_n + b_m^{(j)} \sin mt_n) \right|^2 \tag{4.29}$$

is minimized. Here $t_n = 2n\pi/N$ and $n = 1, 2, 3, \cdots, N$. The number of basis functions M in (4.29) can be considered as a kind of a regularization parameter.

In the next iteration we solve the regularized equation given in (4.16) for the updated boundary $\Gamma^{(j+1)}$ and follow the same procedure up to this point by skipping the evaluations of the equations (4.20) and (4.21) in order to reconstruct only the shape of the obstacle. Iterations continue until a desired stopping criteria (SC_2)

$$SC_2 = \sum_{m=0}^{M} \frac{|a_m^{(j)} - a_m^{(j-1)}|}{M+1} + \sum_{m=1}^{M} \frac{|b_m^{(j)} - b_m^{(j-1)}|}{M} < \bar{\varepsilon}_2 \,, \tag{4.30}$$

is satisfied for sufficiently small $\bar{\varepsilon}_2$.

4.4 Numerical Results

In this section we test the proposed reconstruction method with exact and noisy data for single plane wave illumination in the resonance region. For numerical applications arbitrarily shaped smooth cylinders from Table 1 are used. Tikhonov regularization parameters are chosen by trial error and they are denoted by α_1 and α_2 for the equations (3.16) and (4.16), respectively. Furthermore we use $j_L = J_1$ and $j_S = J_2 - J_1$ for the number of iterations for only the location and shape reconstruction, respectively. Note that we put tilde sign to the parameters obtained by noisy data.

In order to identify the effects of the desired parameters clearly we used some limitations in all numerical examples as listed below,

1. integral equation systems are solved by the Nyström method with a discretization number $N = 64$,
2. the initial shapes $\Gamma^{(0)}$ are chosen as circles with radius $c_0 = 0.2$,
3. the degree of the polynomials are chosen $M = 4$ for the exact data case and $\widetilde{M} = 3$ for noisy data case,
4. parameters in the stopping criterias are chosen $\bar{\varepsilon}_1 = \bar{\varepsilon}_2 = 10^{-4}$,
5. $\delta = 0.03$ used in equation (2.71) to obtain 3% noisy data.

It is noted that above considerations do not guarantee the best reconstructions for all cases. However for our numerical examples these parameters provide acceptable reconstructions. Along this line to introduce the performance of the proposed method accurately a percentage error is defined as

$$ERR^{\Gamma_0} = 100 \frac{\|r - r^{\star}\|}{\|r\|}. \tag{4.31}$$

Here r is the radius function of the star-like parametrized exact curve and $r^{\star}$ denotes the radius function of the reconstructed curve after transforming to the same parametrization form. Additionally, we compute the absolute difference between the center coordinates of the exact $C(d_1, d_2)$ and reconstructed shapes $C^*(d_1^*, d_2^*)$ as

$$C^{|d|} = |C - C^*|. \tag{4.32}$$

Experiment 1: As a first experiment, we choose an apple shaped $\Gamma_0 = \Gamma^{(a)}$ obstacle buried in a rounded triangular $\Gamma_1 = 3/4\Gamma^{(t)}$ cylinder as illustrated in Figure 4.2. The incident angle is $\phi_0 = 0^\circ$ and the wave numbers of the corresponding media are $k_0 = 1.5$, $k_1 = 1$. Reconstructions are obtained from the full near-field data computed by the equation (2.59) over a measurement circle Ω^m, having the radius $c_0 = 2$. We follow the same steps of the inversion algorithm using the near-field data instead of far-field. The reconstruction algorithm needs $j_L = 16$, $j_S = 9$ iterations for exact data

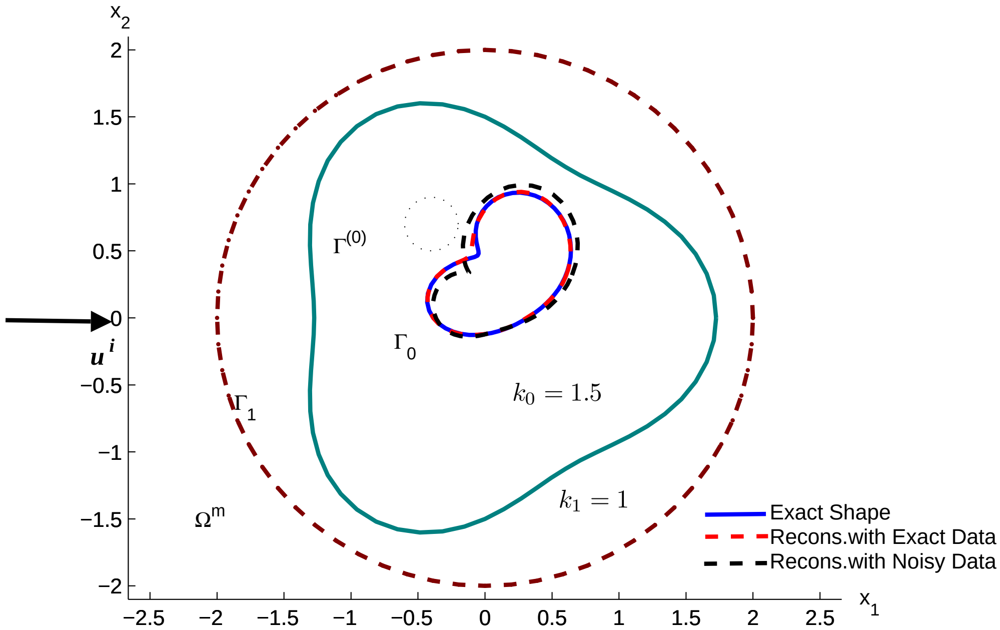

Figure 4.2: Reconstruction of an apple shaped PEC object buried in a rounded triangular shaped dielectric cylinder from full near-field data

and $\widetilde{j}_L = 10$, $\widetilde{j}_S = 12$ for noisy data to reconstruct the location and the shape. We obtain $ERR^{\Gamma_0} \approx 2.781$ percentage error and $C^{|d|} \approx 0.093$ by choosing the parameters $\alpha_1 = 10^{-12}$, $\alpha_2 = 10^{-5}$ for the exact data and $\widetilde{ERR}^{\Gamma_0} \approx 13.807$ error and $\widetilde{C}^{|d|} \approx 0.205$ with the parameters $\widetilde{\alpha}_1 = 10^{-4}$, $\widetilde{\alpha}_2 = 10^{-3}$ for noisy data. In this experiment we choose the cylinders having complex geometries and locate the initial guess in the illuminated part of the scatterers. As to be expected choosing the location of the initial guess has a major effect both for the location and the shape reconstruction of the buried obstacle. However, in the case of choosing a good initial guess we obtain impressive reconstructions especially from the exact data and less than 3% noisy data. On the other hand by choosing a bad initial guess location reconstruction step does not converge and in such cases either location or the shape of cannot be reconstructed. Therefore, in practical applications, in order to be sure for the position and the shape of the inaccessible obstacle it can be recommended to run the reconstruction algorithm several times since it takes only few minutes.

Experiment 2: In the second experiment we find reconstructions by using two illuminations $\phi_0 = 0^\circ$ and $\phi_0 = 180^\circ$ for the same problem configuration with the first experiment. The regularization parameters are chosen such that $\alpha_1 = 10^{-12}$, $\alpha_2 = 10^{-5}$ and $\widetilde{\alpha}_1 = 10^{-4}$, $\widetilde{\alpha}_2 = 2 \times 10^{-4}$ for exact and noisy data, respectively. For

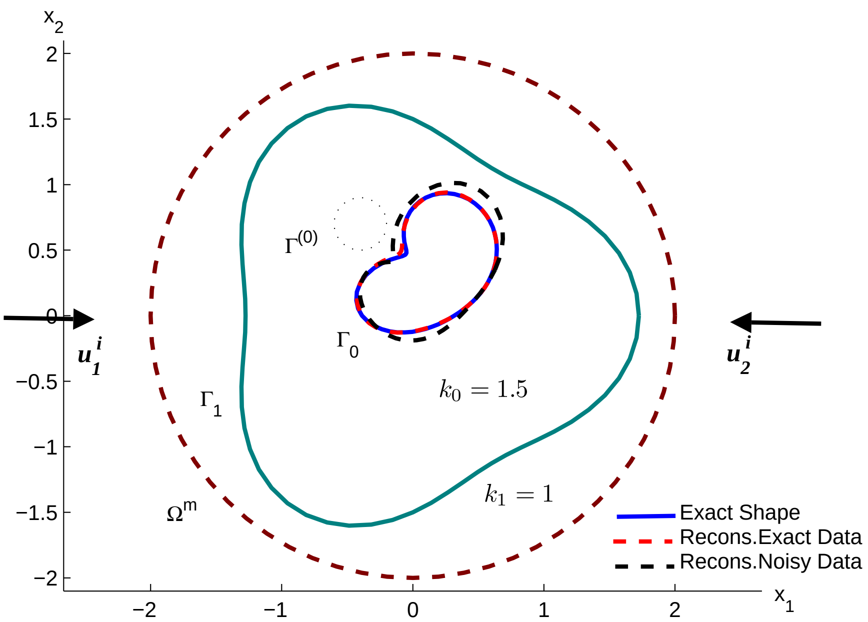

Figure 4.3: Reconstruction of an apple shaped PEC object buried in a rounded triangular shaped dielectric cylinder from full near-field data with two illuminations

the exact data we obtain $j_L = 34$, $j_S = 8$, $ERR^{\Gamma_0} \approx 2.704$, $C^{|d|} \approx 0.047$ and for the noisy data $\widetilde{j}_L = 20$, $\widetilde{j}_S = 11$. $\widetilde{ERR}^{\Gamma_0} \approx 11.419$, $\widetilde{C}^{|d|} \approx 0.184$. From this application we observe that using two illuminations provides insignificantly small change to the error and the rate of error level does not decrease linearly as parallel with the results published in [37]. Therefore for the rest of the experiments only single plane wave illuminations are used.

Experiment 3: In the third example, we test success of the reconstructions under in the limited aperture case with far-field data given in the range of angle π by choosing a peanut shaped buried scatterer $\Gamma_0 = \Gamma^{(p)}$ and a simple shaped penetrable cylinder as a circle $\Gamma_1 = \Gamma^{(c)}$ with radius $c_0 = 2$. This configuration is illuminated from the direction $d = (1,0)$ and the far-field data are collected in 64 equidistant points on the semi circle $\phi \in [\pi/2, 3\pi/2]$ which is called as Ω^m in the figure. Wave numbers for corresponding media are $k_0 = 1$, $k_1 = 0.5$. After $j_L = 33$, $j_S = 10$ iterations for the exact data and $\widetilde{j}_L = 34$, $\widetilde{j}_S = 14$ for noisy data we obtain $ERR^{\Gamma_0} \approx 4.934$, $C^{|d|} \approx 0.338$ and $\widetilde{ERR}^{\Gamma_0} \approx 18.592$, $\widetilde{C}^{|d|} \approx 0.320$ with exact and noisy data, respectively. We choose the parameters $\alpha_1 = 10^{-13}$, $\alpha_2 = 10^{-4}$ for the exact data and $\widetilde{\alpha}_1 = 10^{-5}$, $\widetilde{\alpha}_2 = 10^{-2}$ for noisy data. Our primary experience for this example shows that although the initial guess is located in the shadow region of the buried obstacle we can still find acceptable

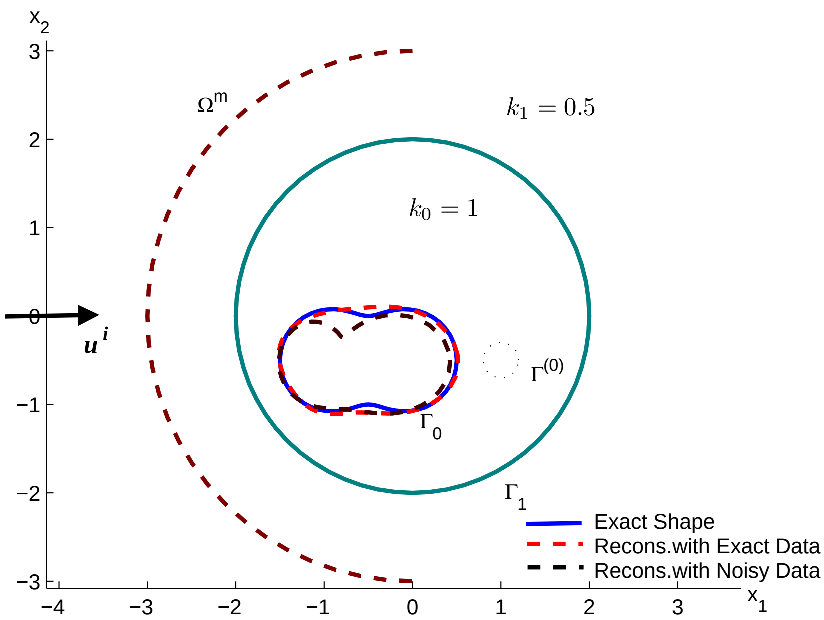

Figure 4.4: Reconstruction of a peanut shaped PEC object buried in a circular cylinder from far-field data given in the range of angle π

reconstruction with limited data. Furthermore the range and the angular position of Ω^m effects strongly. We conclude that in order to find acceptable reconstructions with the proposed method far-field data should be collected at least on a semi-circle. The accuracy of the reconstructions increases when the limited far-field data is constructed from the mildly varying part of u_∞ or $\tilde{u}_\infty$. These data correspond to the scattered field measurements from the smooth parts of the objects. Moreover, the shape of the exterior cylinder Γ_1, effects the reconstructions more than the shape of unknown obstacle itself.

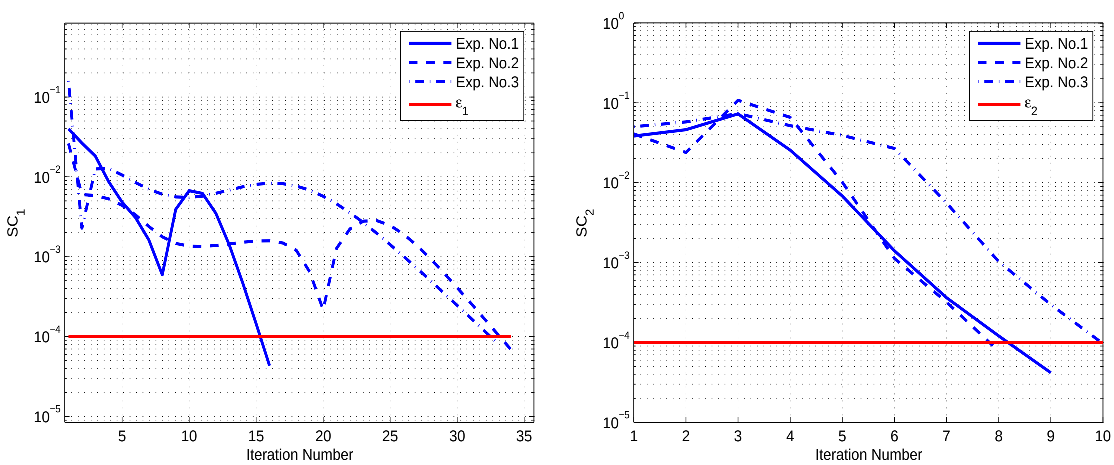

Figure 4.5: Convergence speed of the cost function for the location (left) and shape (right)

Figure 4.5 is given for the experiments 1-3 to show the convergence speed of the location and shape reconstruction algorithms using exact field data. From the mentioned figure it can clearly be concluded that shape reconstruction algorithm has more regular convergence variation than location reconstruction algorithm.

The rest of the numerical experiments from this point are devoted to investigate the behavior of only the shape reconstruction algorithm according to different problem configurations.

Experiment 4: In this example, we choose a peanut shaped $\Gamma_0 = \Gamma^{(p)}$ obstacle buried in a rounded triangular $\Gamma_1 = \Gamma^{(t)}$ cylinder. The incident angle is $\phi_0 = 0°$ and the wave numbers of the corresponding media are $k_0 = 3$, $k_1 = 2$. Reconstructions are obtained as illustrated in Figure 4.6 from the full far-field pattern after $j_S = 12$ iterations with $ERR^{\Gamma_0} \approx 1.781$ percentage error for the exact data choosing the parameters $\alpha_1 = 10^{-15}$, $\alpha_2 = 10^{-3}$ and after $\widetilde{j_S} = 20$ iterations having $\widetilde{ERR}^{\Gamma_0} \approx 5.121$ error for the noisy data with $\widetilde{\alpha}_1 = 10^{-5}$, $\widetilde{\alpha}_2 = 10^{-2}$.

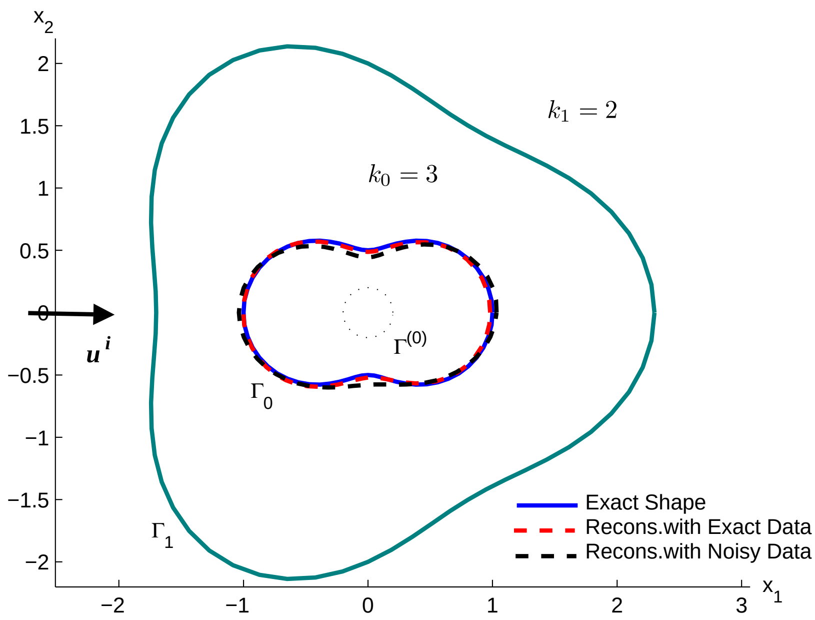

Figure 4.6: Reconstruction of a peanut shaped PEC object buried in a rounded triangular shaped dielectric cylinder from full far-field data

Experiment 5: In the next investigation we want to observe the quality of the reconstructions using wave numbers that satisfy the condition $k_0 < k_1$. This condition physically states that the obstacle is buried in a cylinder having more dense medium than itself. To this aim we just reverse the values of the wave numbers such as

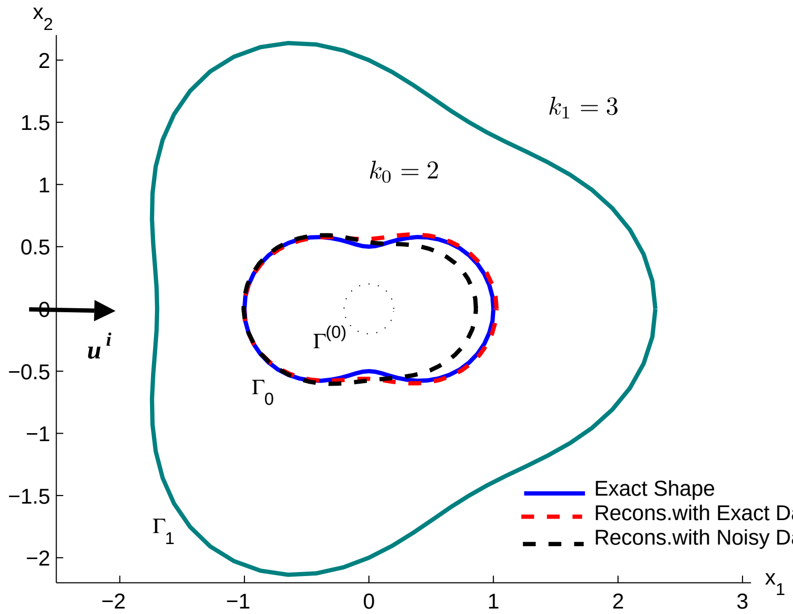

Figure 4.7: Reconstruction of a peanut shaped PEC object buried in a rounded triangular shaped dielectric cylinder from full far-field data

$k_0 = 2$, $k_1 = 3$ and set the rest of the problem configuration the same as given in the first experiment and use full far-field pattern. We obtain the reconstruction for the parameters $\alpha_1 = 10^{-13}$, $\alpha_2 = 10^{-3}$ after $j_S = 23$ iterations in exact data case with $ERR^{\Gamma_0} \approx 3.766$. However, $\widetilde{ERR}^{\Gamma_0} \approx 9.359$ error is observed in the reconstruction obtain from the noisy data with $\widetilde{j_S} = 12$ iterations for the regularization parameters $\widetilde{\alpha}_1 = 10^{-4}$, $\widetilde{\alpha}_2 = 10^{-2}$, see Figure 4.7.

Experiment 6: This experiment as illustrated in Figure 4.8 is devoted to test the method with full near-field data. We use the problem configuration given in the first experiment but here we collect the scattered field on a measurement circle Ω^m having a radius $c_0 = 3$. As to be expected, using near-field data provides more accurate reconstructions than far-field data since it is observed $ERR^{\Gamma_0} \approx 0.454$ percentage error after $j_S = 11$ using exact data and $\widetilde{ERR}^{\Gamma_0} \approx 4.917$ after $\widetilde{j_S} = 21$ iterations using noisy data. Tikhonov regularization parameters are chosen for exact data as $\alpha_1 = 10^{-14}$, $\alpha_2 = 10^{-4}$ and for noisy data $\widetilde{\alpha}_1 = 10^{-5}$, $\widetilde{\alpha}_2 = 10^{-2}$.

Experiment 7: The aim of this application is to observe the error variation in the case of an anti-symmetric and more complex obstacle than a peanut, e.g. such as an apple $\Gamma_0 = 2\Gamma^{(a)}$ located inside of the penetrable cylinder $\Gamma_1 = \Gamma^{(t)}$, see Figure 4.9. We reconstruct the shape of the buried obstacle from the full far-field data and in order to

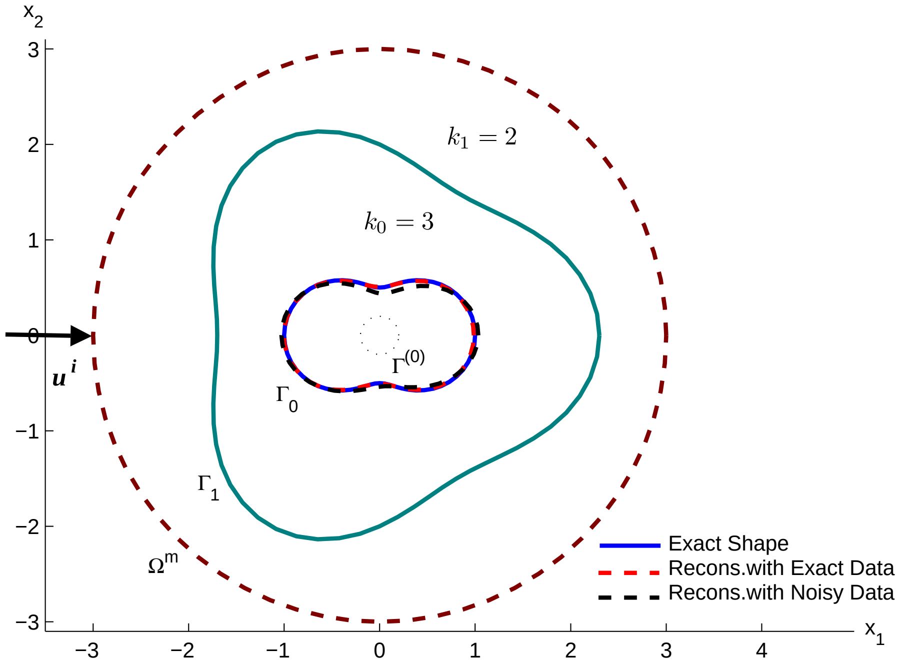

Figure 4.8: Reconstruction of a peanut shaped PEC object buried in a rounded triangular shaped dielectric cylinder from full near-field data

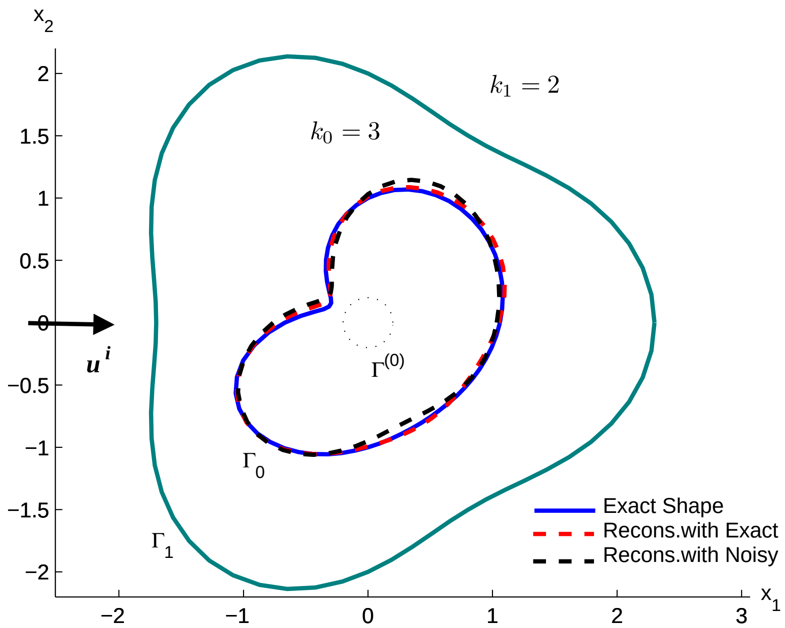

Figure 4.9: Reconstruction of an apple shaped PEC object buried in a rounded triangular shaped dielectric cylinder from full far-field data

compare the results of this experiment with some of others we used the wave numbers and the angle of incidence $(k_0 = 3, k_1 = 2)$ and $\phi_0 = 0°$, respectively. In the exact data case $ERR^{\Gamma_0} \approx 2.757$ is obtained with $j_S = 12$ for the parameters $\alpha_1 = 10^{-15}$, $\alpha_2 = 10^{-3}$ and using noisy data after $\widetilde{j_S} = 17$ iterations error level raised to $\widetilde{ERR}^{\Gamma_0} \approx 5.540$ for the regularization parameters $\widetilde{\alpha}_1 = 10^{-5}$, $\widetilde{\alpha}_2 = 10^{-2}$.

Experiment 8: Here, in order to observe the effect of the exterior cylinder's geometry to the quality of the reconstructions we just replace the rounded triangular shaped cylinder with a circular cylinder having a radius $c_0 = 2$ and kept the rest of the parameters the same as in the previous example. We obtain reconstructions from the full exact far-field data after $j_S = 12$ iterations and from noisy data after $\widetilde{j_S} = 13$ iterations as illustrated in Figure 4.10 having errors $ERR^{\Gamma_0} \approx 2.316$ and $\widetilde{ERR}^{\Gamma_0} \approx 5.305$ for exact and noisy data, respectively. Tikhonov regularization parameters are chosen $\alpha_1 = 10^{-15}$, $\alpha_2 = 10^{-3}$ in exact data case and $\widetilde{\alpha}_1 = \widetilde{\alpha}_2 = 10^{-3}$ in noisy data case.

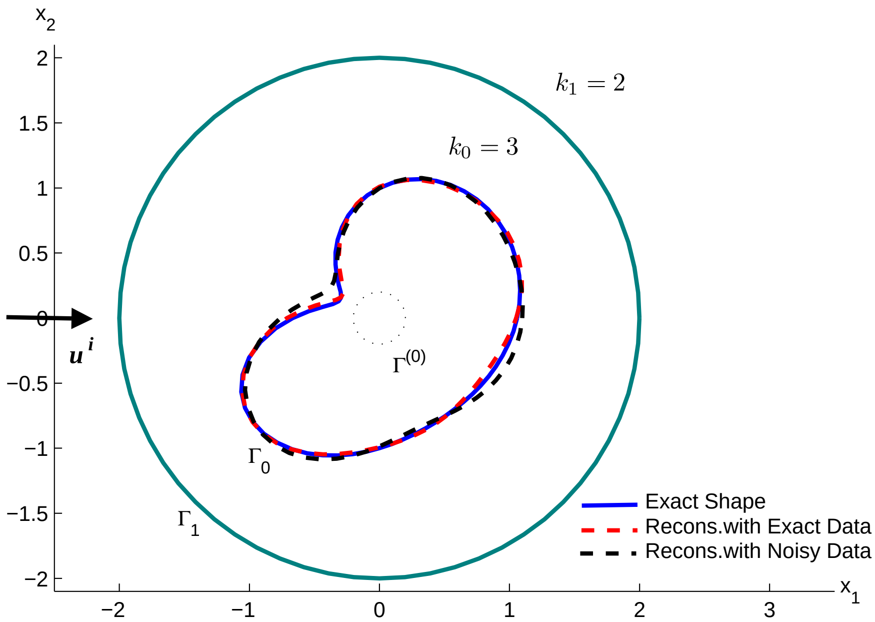

Figure 4.10: Reconstruction of an apple shaped PEC object buried in a circular cylinder shaped dielectric cylinder from full far-field data

Experiment 9: As we noted in the introduction part of Chapter 2 reconstruction method gives accurate results in resonance region. Along this line we considered to reduce the size of the scatterers by choosing $\Gamma_0 = 1/2\Gamma^{(a)}$ and $\Gamma_1 = \Gamma^{(c)}$ with $c_0 = 1$ to study on the close neighborhood of the resonance region for the experiment illustrated in Figure 4.11. Using exact full far-field pattern we observe $ERR^{\Gamma_0} \approx 2.056$ percentage

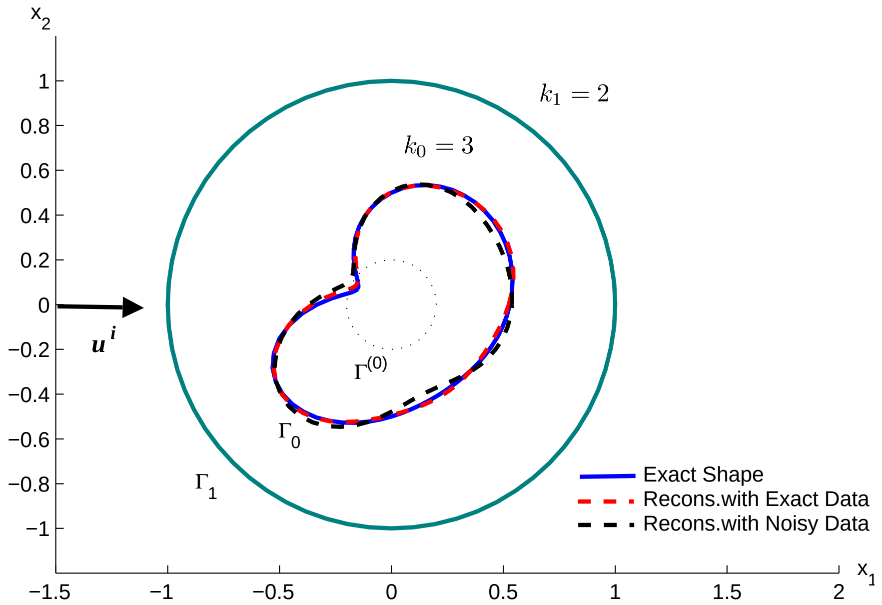

Figure 4.11: Reconstruction of an apple shaped PEC object buried in a circular cylinder shaped dielectric cylinder from full far-field data

error after $j_S = 10$ iterations with the regularization parameters $\alpha_1 = 10^{-12}$, $\alpha_2 = 10^{-6}$. For the noisy data case the error is computed as $\widetilde{ERR}^{\Gamma_0} \approx 5.174$ for $\widetilde{j}_S = 8$, $\widetilde{\alpha}_1 = 10^{-4}$ and $\widetilde{\alpha}_2 = 10^{-3}$.

Experiment 10: In the following example we investigate the effect of the illumination

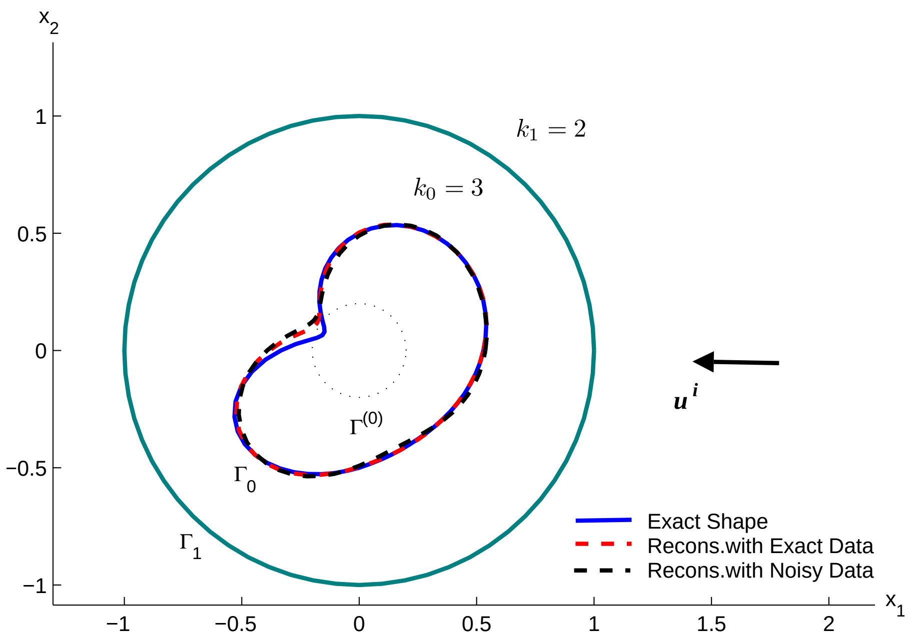

Figure 4.12: Reconstruction of an apple shaped PEC object buried in a circular cylinder shaped dielectric cylinder from full far-field data

angle on the reconstructions. Therefore, only the illumination angle of the problem configuration given in Figure 4.11 is changed by choosing the angle of the plane wave incidence as $\phi_0 = 180°$, see Figure 4.12. We obtain reconstructions for the exact far-field data after $j_S = 17$ iterations and for the noisy data after $\widetilde{j_S} = 11$ iterations from the far-field pattern. In the noise free case regularization parameters are chosen $\alpha_1 = 10^{-14}$, $\alpha_2 = 10^{-6}$ and observed $ERR^{\Gamma_0} \approx 4.089$ percentage error. However, in order to obtain reasonable reconstructions from the noisy data such as having $\widetilde{ERR}^{\Gamma_0} \approx 5.852$ percentage error the regularization parameters are chosen $\widetilde{\alpha}_1 = 10^{-4}$, $\widetilde{\alpha}_2 = 10^{-3}$.

Experiment 11: In this experiment we wanted to shift our problem's domain to the

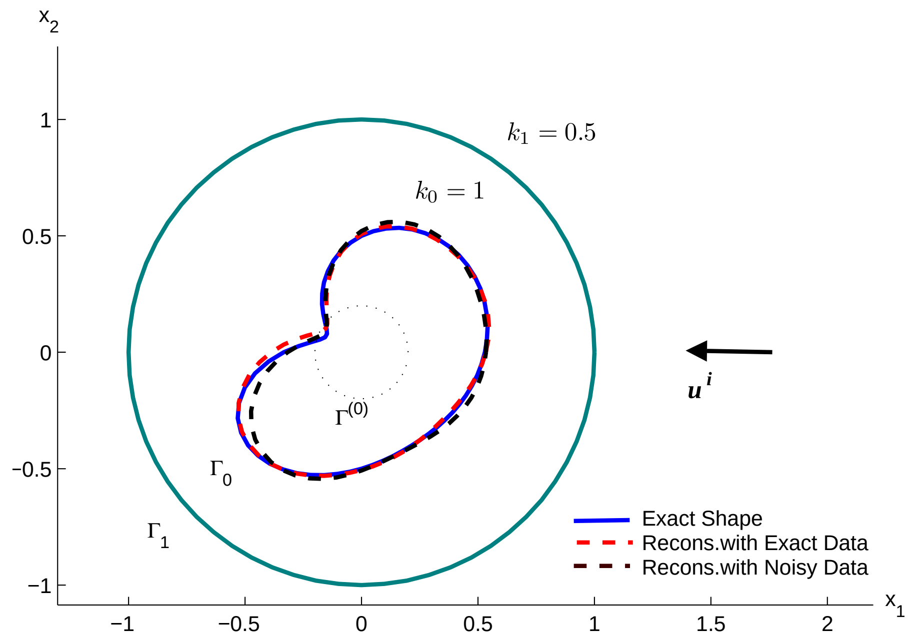

Figure 4.13: Reconstruction of an apple shaped PEC object buried in a circular cylinder shaped dielectric cylinder from full far-field data

closer neighborhood of the resonance region. Therefore we used lower wave numbers such as $k_0 = 1$ for the interior medium of the dielectric cylinder and $k_1 = 0.5$ for the background medium. The geometry of the PEC obstacle is chosen like an apple shaped object $\Gamma_0 = \Gamma^{(a)}$ and the exterior cylinder is a circular cylinder $\Gamma_1 = \Gamma^{(c)}$ with the radius $c_0 = 1$ where the configuration is illuminated by a plane wave with the angle of incidence $\phi_0 = 180°$ as in the previous experiment. The reconstructions illustrated in Figure 4.13 is obtained from full far-field data by choosing Tikhonov regularization parameters $\alpha_1 = 10^{-7}$, $\alpha_2 = 10^{-4}$ for exact field values with $j_S = 6$ and $\widetilde{\alpha}_1 = \widetilde{\alpha}_2 =$

10^{-3} with $\widetilde{j_S} = 9$ for noisy far-field. It is observed $ERR^{\Gamma_0} \approx 3.984$ and $\widetilde{ERR}^{\Gamma_0} \approx 4.914$ percentage error for exact and noisy data cases, respectively.

Experiment 12: Here we still want to clarify the effect of the wave numbers on to the reconstructions with the proposed method. For this we borrowed the problem configuration from the previous experiment and changed the wave numbers by adding complex valued contributions to obtain $k_0 = 1+i$ and $k_1 = 0.5+0.5i$. We reconstructed the shape of buried PEC obstacle as illustrated in Figure 4.14 from full exact far-field for the parameters $j_S = 7$, $\alpha_1 = 10^{-12}$, $\alpha_2 = 10^{-4}$ and from full noisy far-field for the parameters $\widetilde{j_S} = 11$, $\widetilde{\alpha}_1 = 10^{-3}$, $\widetilde{\alpha}_2 = 10^{-2}$. The method provides the reconstructions with $ERR^{\Gamma_0} \approx 6.077$ error in exact data case and $\widetilde{ERR}^{\Gamma_0} \approx 10.574$ in the noisy data case.

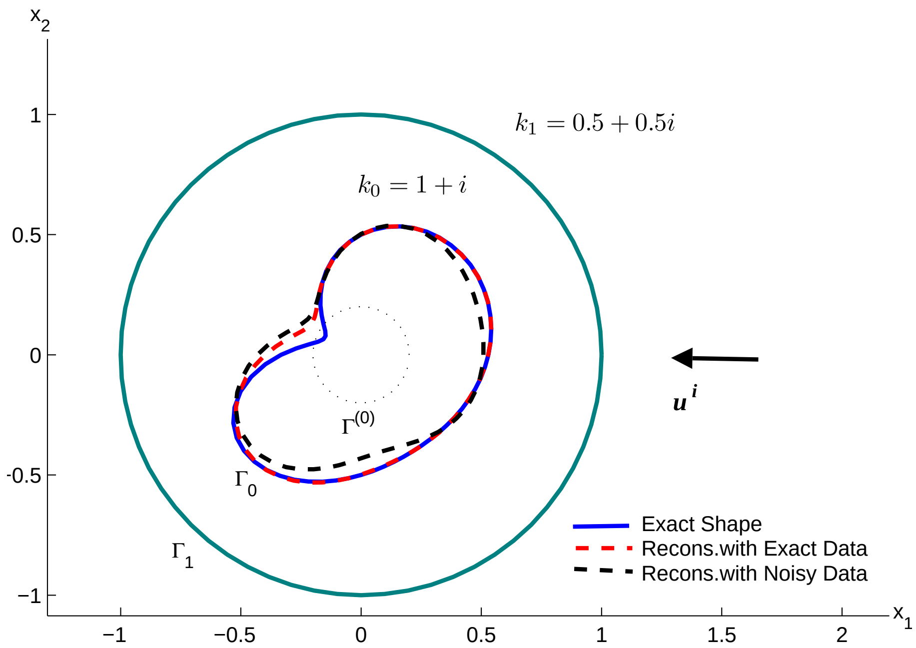

Figure 4.14: Reconstruction of an apple shaped PEC object buried in a circular cylinder shaped dielectric cylinder from full far-field data

Experiment 13: Then we test the success of the method under limited far-field data for the geometry defined in Figure 4.13. For this the far-field data are collected in 64 equidistant points on the semi circle $\phi \in [\pi/2, 3\pi/2]$ which is called as Ω^m in the figures. In the exact data case we found a reasonable reconstruction after $j_S = 7$ iterations with the error $ERR^{\Gamma_0} \approx 4.185$ for the parameters $\alpha_1 = 10^{-12}$ and $\alpha_2 = 10^{-5}$. For the noisy data we obtained $\widetilde{ERR}^{\Gamma_0} \approx 17.306$ for the parameters $\widetilde{j_S} = 6$, $\widetilde{\alpha}_1 = 10^{-3}$, $\widetilde{\alpha}_2 = 5 \times 10^{-5}$, see Figure 4.15. We also tried to obtain reconstructions using exact

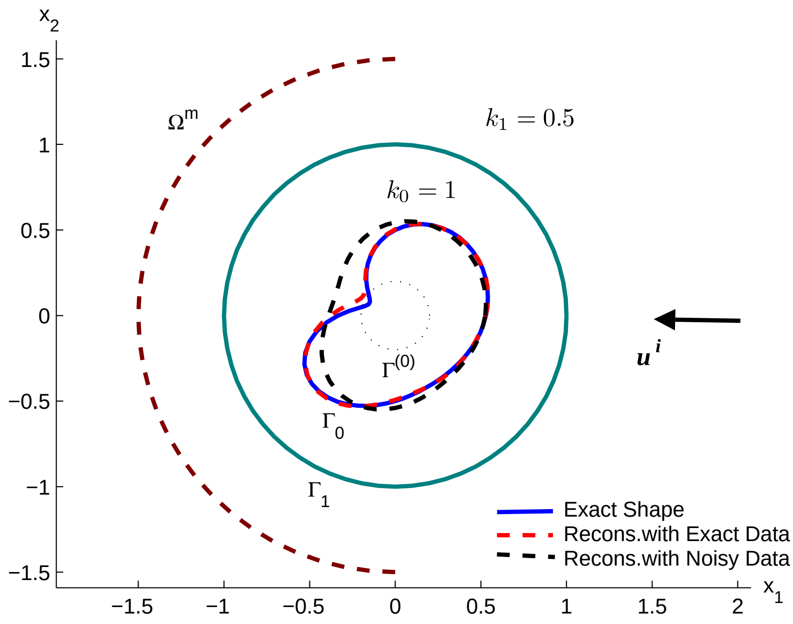

Figure 4.15: Reconstruction of an apple shaped PEC object buried in a circular cylinder shaped dielectric cylinder from far-field data given in the range of angles $\phi \in [\pi/2, 3\pi/2]$

near-field data collected on a measurement circle in the range of angles $\phi \in [\pi/2, 3\pi/2]$ with a radius $c_0 = 3$. As to be expected near-field data provided less error such as $ERR^{\Gamma_0} \approx 3.580$ for $j = 10$ iterations.

Experiment 14: Now we force the method using complex shaped scatterers and the limited far-field data over the curve Ω^m for $\phi \in [0, \pi]$, see Figure 4.16. The perfectly conducting obstacle is chosen as a kite-shaped scatterer $\Gamma_0 = \Gamma^{(k)}$ and the dielectric cylinder was a rounded and rotated square $\Gamma_1 = \Gamma^{(s)}$. The incident angle is $\phi_0 = 180°$ and the wave numbers are considered as $k_0 = 1$, $k_1 = 0.5$. The parameters $j_S = 17$, $\alpha_1 = 10^{-13}$, $\alpha_2 = 10^{-3}$ are used for the noise free case and $\widetilde{j_S} = 20$, $\widetilde{\alpha}_1 = 5 \times 10^{-4}$, $\widetilde{\alpha}_2 = 8 \times 10^{-3}$ for the noisy case. Here, since the buried object has non star-like parametrization we can not compute the error numerically. On the other hand, accuracy of the result due to the complexities of the scatterers can be considered as acceptable for this example.

Experiment 15: The last example is devoted to investigate the effect of the initial guess on the reconstructions by choosing the dimensions of both scatterers relatively larger than the initial guess. That is the buried obstacle considered as a rounded triangular-shaped scatterer $\Gamma_0 = \Gamma^{(t)}$ and the penetrable cylinder is an ellipse $\Gamma_1 = \Gamma^{(e)}$ with constant parameters $e_0 = 5, e_1 = 3$ see Figure 4.17. The angle of the incoming wave is $\phi_0 = 180°$, the wave numbers $k_0 = 1$, $k_1 = 1/\sqrt{2}$ are chosen and the whole

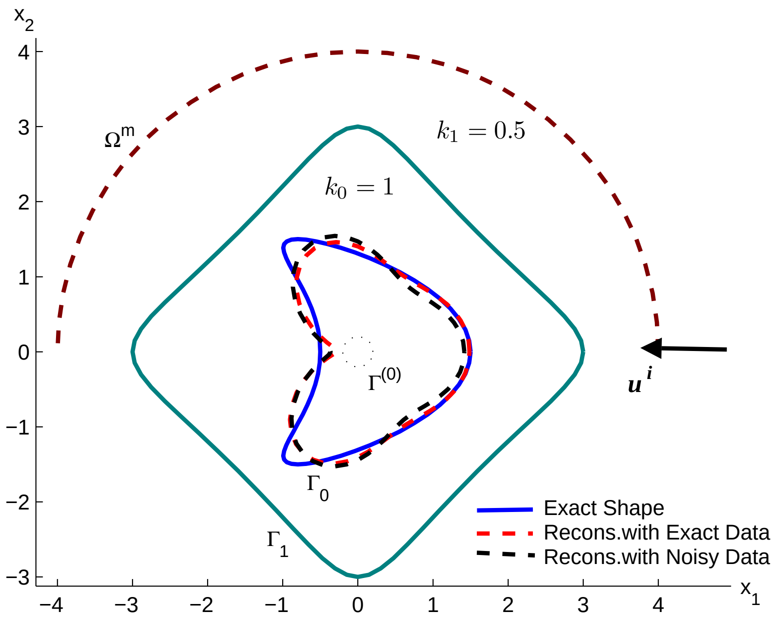

Figure 4.16: Reconstruction of a kite shaped PEC object buried in a rounded square shaped dielectric cylinder from far-field measurements given in the range of angle π

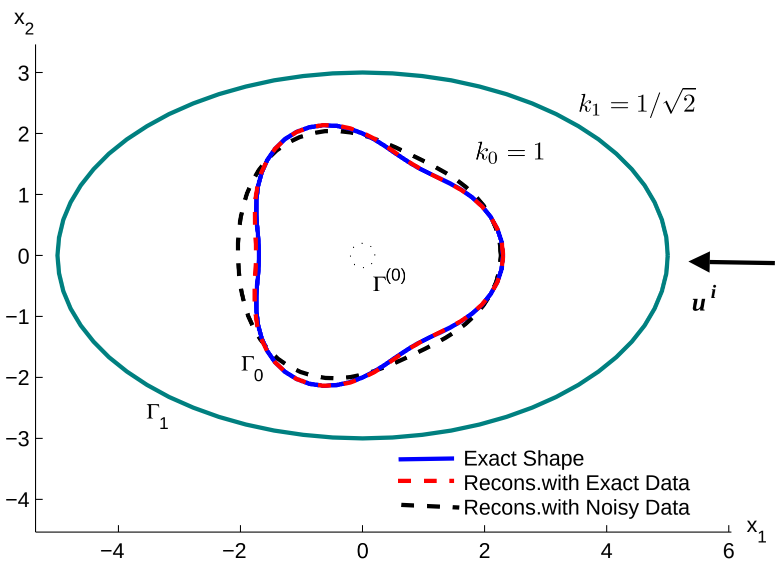

Figure 4.17: Reconstruction of a rounded triangular-shaped PEC object buried in an elliptic cylinder shaped dielectric cylinder from full far-field data

far-field data $\phi \in [0,2\pi]$ is used. In the exact data case $ERR^{\Gamma_0} \approx 0.838$ obtained after $j_S = 35$ iterations for the Tikhonov regularization parameters $\alpha_1 = 10^{-12}$, $\alpha_2 = 10^{-4}$ and for the noisy data $\widetilde{ERR}^{\Gamma_0} \approx 6.931$ obtained for the parameters $\widetilde{j_S} = 13$, $\widetilde{\alpha}_1 = 10^{-1}$, $\widetilde{\alpha}_2 = 10^{-2}$. As it can be seen from the reconstructions especially in the noisy data case the method has difficulties to reconstruct the non-convex parts of the rounded triangular obstacle with such a small initially guessed circle.

4.5 Comments on Numerical Results

In this chapter the applicability of an integral equation based method whose aim is to reconstruct the shape and the location of PEC obstacles buried in arbitrarily shaped dielectric cylinders is investigated. The numerical applications supports that the location and the shape of a buried object can be determined under $(3\% - 4\%)$ level of noise with limited aperture scattered field in the resonance region.

First of all, it should be concluded that using simple shaped scatterers and choosing a good initially guessed boundary with exact full near-/far-field data provide very accurate reconstructions and fast convergence (less iterations). Furthermore, the location and the size of the initial guess effects the success of the results. Indeed, there is a direct proportion with the number of iterations and the spatial difference of the initially guessed boundary from the exact shape.

As to be expected the quality of the reconstructions obtained from near-field measurements are higher. However, using near-field data do not guarantee less iteration numbers than using far-field data in every application. In the near-field applications we also observe that when the radius of the measurement circle increases we need smaller Tikhonov regularization parameters and taking the measurement circle very close to the exterior cylinder do not provide the most accurate reconstructions.

Moreover, in the exact data case we need small Tikhonov regularization parameters and higher degree of polynomials, however for the noisy data we need stronger regularization parameters and lower degree of polynomials. The latter result is same as obtained in [85, 89, 94].

In our numerical experiments, although we set the iteration and the discretization numbers the same for all examples, by increasing their values we can obtain feasible reconstructions for complex shaped objects having smooth corners.

According to our experience in order to obtain accurate reconstruction, the direction of the illumination should be chosen optimally due to the geometry of the scatterers. In all cases illuminated part of the buried object is reconstructed more accurately as compare to the other parts of the obstacle. From this condition we conclude that for the reconstruction of the convex parts of the obstacles precisely, we assume that it is necessary to illuminate these regions directly.

We observed in all numerical applications when the contrast of the real wave numbers k_0 and k_1 is large such that $k_0 > k_1$ we get more accurate reconstructions. However for high wave numbers our reconstructions deteriorates since the scattered wave contains rapid oscillations. We also showed that acceptable reconstructions can be obtained for the wave numbers that have imaginary parts. But generally the quality of the reconstructions obtained for real valued wave numbers are more accurate than for complex wave number cases.

Moreover the range and the angular position of Ω^m has a major effect in the limited data case. We conclude that in order to find acceptable reconstructions with the proposed method near-/far-field data should be collected at least on a semi-circle. Additionally, the accuracy of the reconstructions increases when the limited field data constructed from the mildly varying part of u_∞ or u_1. These data correspond to the scattered field measurements from the smooth parts of the objects since irregular parts generate oscillating fields. Especially, the concave or convex parts of the dielectric cylinder has a major effect on generating fast varying scattered field.

5. CONDUCTIVITY FUNCTION AND SHAPE RECONSTRUCTIONS

In this chapter we combine the reconstruction methods proposed in the thesis for the solution of a problem whose aim is to recover a specific real valued function defined over the surface of the exterior cylinder and the shape of a buried obstacle having Dirichlet boundary condition on its surface.

Electromagnetic waves cannot penetrate into the bounded domain D_0, in the case of using impedance boundary condition on the surface of the exterior cylinder, Γ_1. Therefore in this problem we use conductive boundary condition (CBC) for the outer cylinder. Mathematically, this type of a boundary condition can be considered as a generalization of classical transmission conditions with the impedance boundary condition.

Along this line, we first present a method to construct the conductivity function defined over an arbitrarily shaped unburied cylinder introduced by Yaman in 2008 [94] which is an extention of the approach proposed by Akduman and Kress in 2003 [82]. The other algorithm was proposed by Yaman and Yapar in 2008 [88] for the reconstructions of the sound-soft obstacles buried in arbitrarily shaped cylinders for known inhomogeneous conductivity functions on their surface. Then we combine two reconstruction algorithms in order to find the conductivity function and the shape of buried PEC obstacles, simultaneously by solving two inverse problems in each iteration step.

5.1 Statement of the Direct Problem

In this subsection we consider the problem geometry in Figure 5.1 and derive a numerical solution of a direct scattering problem for a given arbitrarily shaped cylinder Γ_1, with conductive boundary condition on its surface. Let $D_0 \subset \mathbb{R}^2$ be a bounded domain with connected analytic boundary Γ_1 to the unbounded domain D_1, and $\boldsymbol{\nu}_1$ the unit normal of the boundary directed into the exterior of D_0. Furthermore, the complex

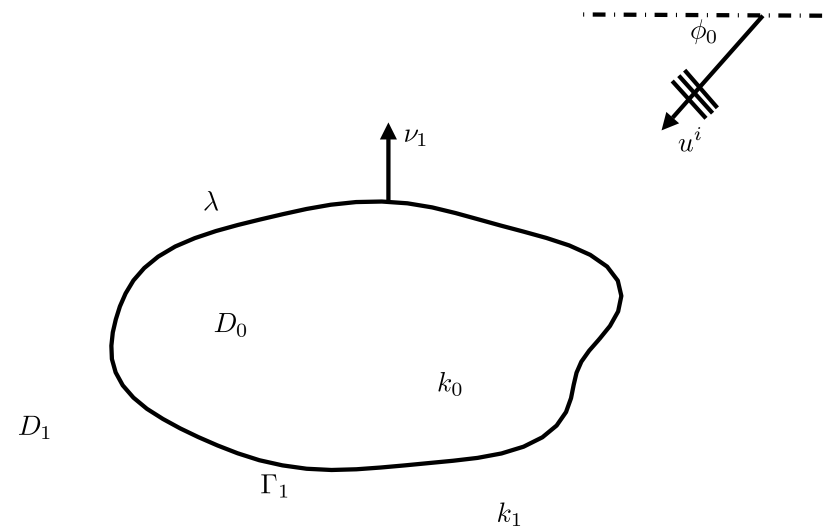

λ : Inhomogeneous conductivity function

Figure 5.1: Geometry of the conductivity function reconstruction problem

valued continuous conductivity function λ is given by,

$$\lambda(\boldsymbol{x}) = i\mu_1\omega\xi(\boldsymbol{x}), \qquad \boldsymbol{x} \in \Gamma_1 . \tag{5.1}$$

The parameter ξ, appearing in the equation (5.1) is the so-called integrated conductivity, see [90]. It is also assumed that $\operatorname{Im}\lambda \leq 0$ on Γ_1, see [92].

In this configuration, an arbitrarily shaped cylinder is illuminated by a plane wave u^i defined in (2.1) whose electric field vector is polarized parallel to the x_3-axis. Due to the symmetry and homogeneity along the x_3-axis the total electric field vector will be polarized both inside and outside of the cylinder parallel to the x_3-axis, that is, $\boldsymbol{E}_0 = (0,0,u_0)$ and $\boldsymbol{E}_1 = (0,0,u_1)$, respectively.

Then the problem is reduced to a scalar one in terms of total fields u_0 and u_1 which can be decomposed as $u_1 = u^i + u^s$ have to satisfy the homogeneous Helmholtz equations

$$\triangle u_j + k_j^2 u_j = 0 \quad \text{in} \quad D_j, \qquad j = 0,1 , \tag{5.2}$$

with the conductive boundary condition

$$\begin{aligned} & u_0 = u_1 \\ & \frac{\partial u_1}{\partial \boldsymbol{\nu}_1} - \frac{\partial u_0}{\partial \boldsymbol{\nu}_1} = \lambda u_1 \end{aligned} \qquad \text{on} \quad \Gamma_1 . \tag{5.3}$$

At infinity the Sommerfeld radiation condition is imposed that the scattered wave u^s is outgoing, see the statement (2.6).

We follow the existence and the uniqueness theorems in [92] omitting the technical details and use the same integral representation of the fields under the assumptions of the referred paper. Therefore we represent the scattered and interior total fields as a combination of single- and double- layer potentials

$$u^s(\boldsymbol{x}) = \int_{\Gamma_1} \left\{ \frac{\partial \Phi_1(\boldsymbol{x},\boldsymbol{y})}{\partial \boldsymbol{\nu}_1(\boldsymbol{y})} \psi(\boldsymbol{y}) + \Phi_1(\boldsymbol{x},\boldsymbol{y})\varphi(\boldsymbol{y}) \right\} ds(\boldsymbol{y}), \quad \boldsymbol{x} \in D_1, \tag{5.4}$$

$$u_0(\boldsymbol{x}) = \int_{\Gamma_1} \left\{ \frac{\partial \Phi_0(\boldsymbol{x},\boldsymbol{y})}{\partial \boldsymbol{\nu}_1(\boldsymbol{y})} \psi(\boldsymbol{y}) + \Phi_0(\boldsymbol{x},\boldsymbol{y})\varphi(\boldsymbol{y}) \right\} ds(\boldsymbol{y}), \quad \boldsymbol{x} \in D_0. \tag{5.5}$$

Then we can write the integral equation system in an abbreviated form as

$$(E_3 + A_3) \begin{pmatrix} \psi \\ \varphi \end{pmatrix} = -2 \begin{pmatrix} u^i|_{\Gamma_1} \\ \lambda u^i - \left.\dfrac{\partial u^i}{\partial \boldsymbol{\nu}_1}\right|_{\Gamma_1} \end{pmatrix}, \tag{5.6}$$

where I is the identity operator.

It is noted again that to solve the system numerically we use parametrized forms of the operators as defined in (2.22) - (2.25) and evaluate singular and regular parts of the parametrized operators, separately. Then the operator $A_3 : C(\Gamma_1) \times C(\Gamma_1) \to C(\Gamma_1) \times C(\Gamma_1)$ is defined by

$$A_3 := \begin{pmatrix} K_{11,1} - K_{11,0} & S_{11,1} - S_{11,0} \\ -T_{11,1} + T_{11,0} + \lambda K_{11,1} & -K'_{11,1} + K'_{11,0} + \lambda S_{11,1} \end{pmatrix}. \tag{5.7}$$

Following the same argument as explained for the operator A_1 in chapter 3 it suffices to consider the operators A_3 and E_3 on the spaces of continuous functions. Since the operator $E_3 : C(\Gamma_1) \times C(\Gamma_1) \to C(\Gamma_1) \times C(\Gamma_1)$ given by the matrix

$$E_3 := \begin{pmatrix} 2I & 0 \\ \lambda I & 2I \end{pmatrix}, \tag{5.8}$$

has a bounded inverse and $(E_3 + A_3)^{-1}$ exists and is bounded, see [92]. The unknown densities $\psi \in C(\Gamma_1)$ and $\varphi \in C(\Gamma_1)$ can be computed numerically from the equation (5.6). Then substituting the density functions ψ and φ to the equations (2.61) and (2.64) one can obtain the near-field and the far-field, respectively.

5.2 Numerical Examples for the Direct Problem

The conductive boundary value problem is reduced to the well-known transmission problem by choosing $\lambda = 0$ and to the scattering problem for perfect electric conductors (PEC) via $\lambda \gg 0$. In order to test the reduced problem we solve the transmission problem via a potential approach where the definition and the investigation of the problem is described in Chapter 3.8 of the book [98]. For the solution of the PEC scattering problem Chapter 3.5 of [98] is followed. We observed that in each comparison case both numerical results match accurately.

Moreover to illustrate the exponential convergence of the direct problem clearly Table 5.1 gives values of the far-field pattern $u_\infty(\boldsymbol{d})$ and $u_\infty(\boldsymbol{-d})$ in the forward direction $\boldsymbol{d}$ and the backscattering direction $\boldsymbol{-d}$ where the direction $\boldsymbol{d}$ of the incident wave is $\boldsymbol{d} = (-1, 0)$.

Table 5.1: Numerical example for the direct scattering problem with CBC

Wave numbers:	N	$Re\,u_\infty(\boldsymbol{d})$	$Im\,u_\infty(\boldsymbol{d})$	$Re\,u_\infty(\boldsymbol{-d})$	$Im\,u_\infty(\boldsymbol{-d})$
$k_0 = 2$	16	-0.17036760	0.48298333	-0.92747133	0.87803942
	32	-0.17036758	0.48296969	-0.92744230	0.87805487
$k_1 = 1$	64	-0.17036758	0.48296970	-0.92744233	0.87805485
	128	-0.17036758	0.48296970	-0.92744233	0.87805485
$k_0 = 1+i$	16	-0.84938970	0.94141239	-1.40799611	0.42745603
	32	-0.84939076	0.94141434	-1.40797352	0.42745599
$k_1 = 0.5+i0.5$	64	-0.84939075	0.94141434	-1.40797354	0.42745598
	128	-0.84939075	0.94141434	-1.40797354	0.42745598
$k_0 = 5+i$	16	1.47319387	- 1.70565385	-2.15261113	0.72987802
	32	1.47316833	- 1.70571814	-2.15560981	0.73398480
$k_1 = 2+i$	64	1.47316833	- 1.70571814	-2.15560983	0.73398478
	128	1.47316833	- 1.70571814	-2.15560983	0.73398478

We choose the shape of the scatterer as the following kite-shaped scatterer,

$$\Gamma_1 = \left\{(\cos t + 1.3\cos^2 t - 1.3, 1.5\sin t) : t \in [0, 2\pi]\right\} \tag{5.9}$$

and a continuous conductivity function such that,

$$\lambda(z_1(t)) = 1 + \sin^3 t + i(\sin t - 1), \quad t \in [0, 2\pi]. \tag{5.10}$$

5.3 Inverse Problem

The inverse scattering problem considered here is the reconstruction of the conductivity function from the near- or far-field pattern for one incident wave, assuming that the shape of scatterer is known. We further assume that the wave number

k_0^2 is not a Dirichlet eigenvalue for the negative Laplacian in the interior of Γ_1 and the boundary curve Γ_1 is analytic.

In our approach we first construct the total fields u_1 and u_0 from the given near-/far-field pattern. Then we determine the unknown function λ from the conductive boundary condition,

$$\frac{\partial u_1}{\partial \boldsymbol{\nu}_1} - \frac{\partial u_0}{\partial \boldsymbol{\nu}_1} = \lambda u_1 \quad \text{on } \Gamma_1 \, . \tag{5.11}$$

Here, we seek the fields in the form of single-layer potentials,

$$u^s(\boldsymbol{x}) = \int_{\Gamma_1} \Phi_1(\boldsymbol{x},\boldsymbol{y})\phi(\boldsymbol{y})\, ds(\boldsymbol{y}) \, , \qquad \boldsymbol{x} \in D_1 \, , \tag{5.12}$$

$$u_0(\boldsymbol{x}) = \int_{\Gamma_1} \Phi_0(\boldsymbol{x},\boldsymbol{y})\chi(\boldsymbol{y})\, ds(\boldsymbol{y}) \, , \qquad \boldsymbol{x} \in D_0 \, . \tag{5.13}$$

By the first CBC, namely, $u_0 = u_1$ on Γ_1 the densities ϕ and χ are coupled by the integral equation

$$S_{11,1}\phi - S_{11,0}\chi = -2u^i \, . \tag{5.14}$$

The density ϕ is determined from the far-field pattern of the scattered field which is obtained by using the asymptotic behaviour of the Hankel function as

$$u_\infty(\boldsymbol{x}) = \frac{e^{-i\pi/4}}{\sqrt{8\pi k_1}} \int_{\Gamma_1} e^{-ik_1 \boldsymbol{x}\cdot\boldsymbol{y}}\, \phi(\boldsymbol{y})\, ds(\boldsymbol{y}) \, , \qquad \boldsymbol{x} \in \Omega \, , \tag{5.15}$$

for the observation direction $\boldsymbol{x}$, where $\Omega = \{(cos\,\theta, sin\,\theta) : \theta \in [0,2\pi]\}$. Hence, given the far-field pattern u_∞, the integral equation of the first kind has to be solved,

$$S_\infty \phi = u_\infty \, . \tag{5.16}$$

The integral operator $S_\infty : L^2(\Gamma_1) \to L^2(\Omega)$ is given by

$$(S_\infty \phi)(\boldsymbol{x}) := \frac{e^{-i\pi/4}}{\sqrt{8\pi k_1}} \int_{\Gamma_1} e^{-ik_1 \boldsymbol{x}\cdot\boldsymbol{y}}\, \phi(\boldsymbol{y})\, ds(\boldsymbol{y}) \, , \qquad \boldsymbol{x} \in \Omega \, . \tag{5.17}$$

The operator S_∞ has an analytic kernel, therefore the equation (5.16) is severely ill-posed. For this reason some kind of stabilization such as Tikhonov regularization has to be applied. For a regularized solution in the sense of Tikhonov the equation is solved as

$$\alpha\phi + S_\infty^* S_\infty \phi = S_\infty^* u_\infty \tag{5.18}$$

with a regularization parameter $\alpha > 0$ and the adjoint $S_\infty^* : L^2(\Omega) \to L^2(\Gamma_1)$ of S_∞ is given by

$$(S_\infty^* \zeta)(\boldsymbol{y}) = \frac{e^{i\pi/4}}{\sqrt{8\pi k_1}} \int_\Omega e^{ik_1 \boldsymbol{x}\cdot\boldsymbol{y}} \zeta(\boldsymbol{x})\, ds(\boldsymbol{x}), \qquad \boldsymbol{y} \in \Gamma_1 . \tag{5.19}$$

Once the density ϕ is known from the equation (5.18), one can compute the density χ by using the integral equation (5.14).

Finally, to reconstruct the conductivity function λ, with the equation (5.11), the total field expressions over the boundary Γ_1 are given under the jump conditions as

$$u_1(\boldsymbol{x}) = u^i(\boldsymbol{x}) + \int_{\Gamma_1} \Phi_1(\boldsymbol{x},\boldsymbol{y})\, \phi(\boldsymbol{y})\, ds(\boldsymbol{y}), \qquad \boldsymbol{x} \in \Gamma_1, \tag{5.20}$$

$$\frac{\partial u_1}{\partial \boldsymbol{\nu}_1}(\boldsymbol{x}) = \frac{\partial u^i}{\partial \boldsymbol{\nu}_1}(\boldsymbol{x}) + \int_{\Gamma_1} \frac{\partial \Phi_1(\boldsymbol{x},\boldsymbol{y})}{\partial \boldsymbol{\nu}_1(\boldsymbol{x})} \phi(\boldsymbol{y})\, ds(\boldsymbol{y}) - \frac{1}{2}\phi(\boldsymbol{x}), \qquad \boldsymbol{x} \in \Gamma_1, \tag{5.21}$$

$$\frac{\partial u_0}{\partial \boldsymbol{\nu}_1}(\boldsymbol{x}) = \int_{\Gamma_1} \frac{\partial \Phi_0(\boldsymbol{x},\boldsymbol{y})}{\partial \boldsymbol{\nu}_1(\boldsymbol{x})} \chi(\boldsymbol{y})\, ds(\boldsymbol{y}) + \frac{1}{2}\chi(\boldsymbol{x}), \qquad \boldsymbol{x} \in \Gamma_1 . \tag{5.22}$$

The reconstruction of the λ will be sensitive to errors in u_1 in the vicinity of zero. To obtain a more stable solution, we express the unknown function λ in terms of trigonometric basis functions such that

$$\kappa_r(z_1(t)) = e^{irt}, \quad r = 0, \pm 1, \pm 2, \ldots, \pm R, \quad t \in [0, 2\pi], \tag{5.23}$$

as a linear combination

$$\lambda = \sum_{n=-R}^{R} \tau_r \kappa_r \qquad \text{on } \Gamma_1 . \tag{5.24}$$

Then equation (5.11) has to be satisfied in the least squares sense, that is, the coefficients $\tau_{-R}, \ldots, \tau_R$ in (5.24) are determined when for a set of grid points $\boldsymbol{x}_1, \boldsymbol{x}_2, \ldots, \boldsymbol{x}_N$ on Γ_1 the least squares sum

$$\sum_{n=1}^{N} \left| \left\{ \frac{\partial u_1}{\partial \boldsymbol{\nu}_1}(\boldsymbol{x}_n) - \frac{\partial u_0}{\partial \boldsymbol{\nu}_1}(\boldsymbol{x}_n) \right\} - \sum_{r=-R}^{R} \tau_r \kappa_r(\boldsymbol{x}_n)\, u_1(\boldsymbol{x}_n) \right|^2 \tag{5.25}$$

is minimized. The number of basis functions R in (5.24) can be considered as some kind of an additional regularization parameter.

5.4 Numerical Results for Conductivity Function Reconstructions

In this section we describe the details of the numerical implementation of the method and show the applicability of the reconstruction algorithm both for noisy and exact data case by presenting some illustrative examples. In these examples, the integral equation systems are solved through the Nyström method with a discretization number $N = 64$. In all examples the regularization parameters α and R are chosen by trial and error. In this study, for the following experiments the parameter δ in equation (2.71) is chosen as $\delta = 0.03$ to have a noise level of 3%.

Experiment 1: In the first numerical application, an elliptic scatterer $\Gamma_1 = \Gamma^{(e)}$ with semi-axis $e_0 = 2$ and $e_1 = 1.5$ is considered. The conductivity function over the boundary is given by

$$\lambda(z_1(t)) = \frac{1+\cos t \sin^2 t}{2+\cos t} - i\frac{\cos^2 t}{3-\cos t}, \quad t \in [0, 2\pi]. \tag{5.26}$$

Both for the exact and noisy far-field data cases, the wave numbers and the illumination angle are given by $k_0 = 1+0.25i, k_1 = 0.5$, $\phi_0 = 0°$, respectively. To reconstruct λ with exact data, the regularization parameters are chosen as $\alpha = 10^{-9}$ and $R = 4$ whereas for noisy data $\alpha = 0.2$ and $R = 3$ gives acceptable results. Here, the conductivity function

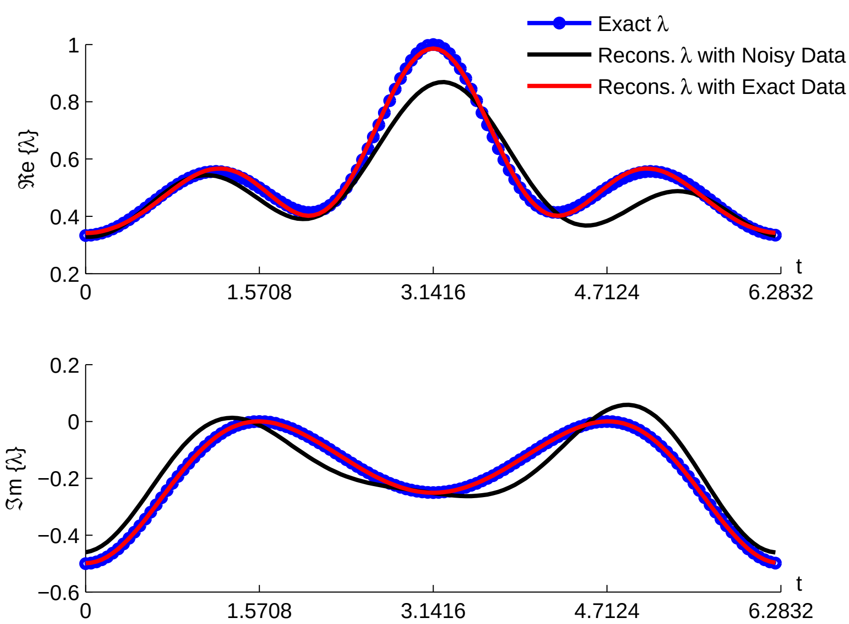

Figure 5.2: Reconstruction of the λ defined over an elliptic cylinder

was chosen as a rational function and representing the conductivity function in terms of exponential basis functions yields poor approximation. Therefore, we could not observe the advantage of solving the equation (5.11) in least squares sense. However, for this example especially the reconstruction with the exact data can be considered rather impressive.

Experiment 2: The second example is devoted to test the method with limited aperture far-field data using complex valued wave numbers both for the interior and the exterior mediums. To this aim, a rounded triangular shaped cylinder with the plane wave incidence of $\phi_0 = 0^\circ$ is chosen and the far-field data are collected in 64 equidistant points on the semi circle $\phi \in [0, \pi]$. The wave numbers of the background media are given as $k_0 = 2 + 0.5i$ and $k_1 = 0.5 + 1.5i$ and the conductivity function is

$$\lambda(z_1(t)) = \sin^2 \frac{t}{2} + i\left(\cos^2 \frac{t}{2} - 1\right), \quad t \in [0, 2\pi]. \tag{5.27}$$

The Tikhonov regularization parameters and the degree of the polynomials are chosen for exact data as $\alpha = 10^{-12}$, $R = 2$ and for noisy data as $\alpha = 10^{-2}$, $R = 1$. It is

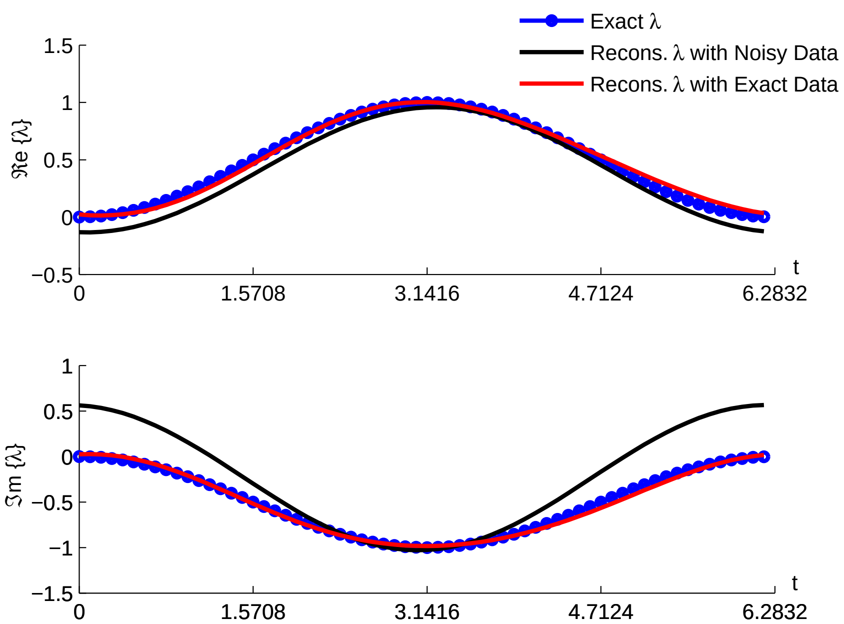

Figure 5.3: Reconstruction of the λ defined over a rounded triangular shaped cylinder

observed that the treatment of the reconstructions do not change significantly using the far-field data given in the range of angle π. Moreover, choosing exponential basis functions in the least square regularization provides a major advantage on the quality of the reconstructions when the conductivity function has a nature of trigonometric polynomials.

Experiment 3: In the third application, we want to observe the quality of the reconstructions using real valued wave numbers that satisfy the condition $k_0 < k_1$. This condition physically states the obstacle is buried in a more dense medium than itself. For this a rounded rectangular shaped scatterer having wave number $k_0 = 2$ and conductivity function

$$\lambda(z_1(t)) = 1.5 - \cos t + 0.5\sin 2t - i(2 + 0.5(\cos t + \sin t)), \quad t \in [0, 2\pi], \qquad \textbf{(5.28)}$$

is buried in an infinite background medium $k_1 = 3$, and illuminated by a plane wave with an incident angle $\phi_0 = 0°$. We used far-field in this experiment and for the exact data the regularization parameters $\alpha = 10^{-12}, R = 4$ and for the noisy data $\alpha = 10^{-5}, R = 2$ are chosen. Here, the main difference of the treatment of the inversion

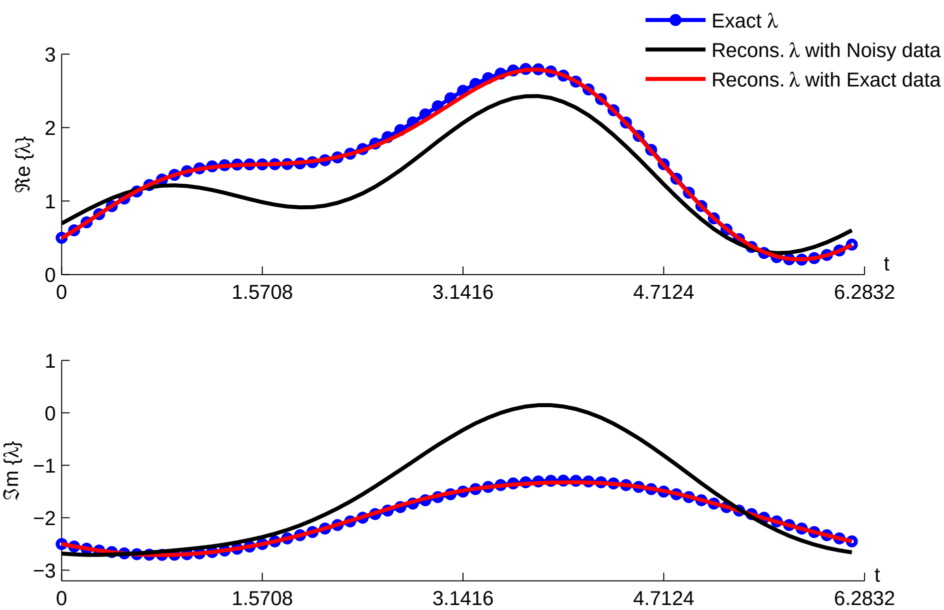

Figure 5.4: Reconstruction of the λ defined over an rounded rectangular shaped cylinder

algortihm as compare to previous two experiments is that one needs smaller Tikhonov regularization parameters in order to get acceptable reconstructions. Moreover, the quality of the reconstructions are highly sensitive on the selection of noise ratio.

As it is mentioned in the introduction of this chapter we are now in a position to combine the proposed algorithm for the reconstructions of the conductivity functions with the algorithm for the reconstructions of arbitrarily shaped perfectly electric conductors buried in cylinders having CBC satisfied on their surface see [88].

5.5 Statement of the Direct Problem

The aim of the direct problem is to compute the scattered near-/far-field, for given shapes Γ_0, Γ_1 and conductivity function λ in the case of a single time-harmonic electromagnetic plane wave illumination. For this lets consider the geometry of problem as given in Figure 5.5. As parallel to the previous investigations we assume

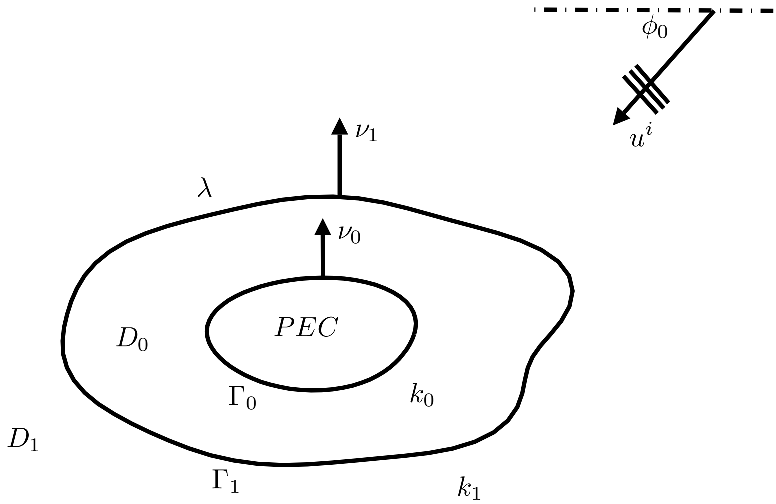

Figure 5.5: Geometry of the conductivity function and buried shape reconstruction problem

that infinitely long cylinders under TM-polarized electromagnetic wave illumination. Hence the problem is reduced to a scalar one in terms of the interior total field u_0 and the exterior total field u_1 that have to satisfy the Helmholtz equations for the corresponding background media

$$\triangle u_j + k_j^2 u_j = 0 \quad \text{in} \quad D_j \qquad j = 0, 1\,, \tag{5.29}$$

where k_j is the wave number of the corresponding medium. We further assume that the conductive boundary condition is satisfied over Γ_1 and the Dirichlet boundary condition is satisfied over Γ_0 such that

$$u_1 = u_0 \quad \text{and} \quad \frac{\partial u_1}{\partial \boldsymbol{\nu}_1} - \frac{\partial u_0}{\partial \boldsymbol{\nu}_1} = \lambda u_1 \quad \text{on}\,\Gamma_1\,, \tag{5.30}$$

$$u_0 = 0 \quad \text{on}\,\Gamma_0\,, \tag{5.31}$$

where λ is a real valued function defined on Γ_1.

We use the same integral representations of the scattered field u^s, and the interior total field u_0, as given in (2.59) and (2.60), respectively. Then by omitting the details for the derivation of the following integral equation system which are analogous to the chapter 3 we propose it as

$$2\psi + K_{11,1}\psi - K_{11,0}\psi + S_{11,1}\varphi - S_{11,0}\varphi - S_{01,0}\chi = -2u^i|_{\Gamma_1}\,, \tag{5.32}$$

$$\begin{aligned} \lambda\psi - T_{11,1}\psi + T_{11,0}\psi + \lambda K_{11,0}\psi + 2\varphi - K^{'}_{11,1}\varphi + K^{'}_{11,0}\varphi + \lambda S_{11,1}\varphi + \\ + K^{'}_{01,0}\chi = 2\frac{\partial u^i}{\partial \boldsymbol{\nu}_1}\bigg|_{\Gamma_1} - 2\lambda u^i|_{\Gamma_1}\,, \end{aligned} \tag{5.33}$$

$$K_{10,0}\psi + S_{10,0}\varphi + S_{00,0}\chi = 0\,. \tag{5.34}$$

This equation system is derived by applying the conductive boundary condition (5.30) and the Dirichlet boundary condition (5.31) to the integral representation of the fields (2.59) and (2.60) via jump relations [43] for the unknown densities $\psi,\varphi \in C(\Gamma_1)$ and $\chi \in C^{0,\beta}(\Gamma_0)$. To write (5.32)-(5.34) in a shorter way we introduce the compact operator A_4 from $C(\Gamma_1)\times C(\Gamma_1)\times C^{0,\beta}(\Gamma_0)$ into $C(\Gamma_1)\times C(\Gamma_1)\times C^{1,\beta}(\Gamma_0)$

$$A_4 := \begin{pmatrix} K_{11,1} - K_{11,0} & S_{11,1} - S_{11,0} & -S_{01,0} \\ -T_{11,1} + T_{11,0} + \lambda K_{11,1} & -K'_{11,1} + K'_{11,0} + \lambda S_{11,1} & K'_{01,0} \\ K_{10,0} & S_{10,0} & 0 \end{pmatrix}, \tag{5.35}$$

and the operator $E_4 : C(\Gamma_1)\times C(\Gamma_1)\times C^{0,\beta}(\Gamma_0) \to C(\Gamma_1)\times C(\Gamma_1)\times C^{1,\beta}(\Gamma_0)$

$$E_4 := \begin{pmatrix} 2I & 0 & 0 \\ \lambda I & 2I & 0 \\ 0 & 0 & S_{00,0} \end{pmatrix}, \tag{5.36}$$

to obtain

$$(E_4 + A_4)\begin{pmatrix} \psi \\ \varphi \\ \chi \end{pmatrix} = -2\begin{pmatrix} u^i|_{\Gamma_1} \\ \lambda u^i|_{\Gamma_1} - \dfrac{\partial u^i}{\partial \boldsymbol{\nu}_1}\bigg|_{\Gamma_1} \\ 0 \end{pmatrix}, \tag{5.37}$$

where I is the identity operator. Now one can find the values of the unknown density functions from the solution of the system given in (5.37) and calculate the near- (2.61) or the far-field expressions (2.64) by substituting values of the corresponding densities ψ and φ.

5.6 Comments on the Numerical Results of the Direct Problem

We check the accuracy of the forward problem code by reducing our problem to the problems investigated in the previous chapters. For instance we choose the conductivity function which vanishes ($\lambda = 0$) on the boundary of the exterior cylinder Γ_1, and then reduce the current direct problem to the problem investigated in chapter 4. Moreover we compare our conductive boundary value problem results by omitting the buried PEC cylinder from the geometry of the problem given in Figure 5.5 with the published results in [94].

For all tests we observe that results of the original problems and our reduced problems match accurately and these two comparison is sufficient to show that the full direct problem solved correctly. And also as to be expected we obtain an exponential convergence of the solution of this direct problem for the analytic curves.

5.7 Inverse Problem

In the inverse problem we want to reconstruct the shape of the buried PEC obstacle Γ_0 and the conductivity function λ from the knowledge of the near-/far-field for given Γ_1 and the corresponding wave numbers k_0 and k_1. For this we first consider a regular parametrization of Γ_1

$$\Gamma_1 = \{\boldsymbol{z}(t) : t \in [0, 2\pi]\}\,, \tag{5.38}$$

then $\lambda^{(0)}$ is also defined on $t \in [0, 2\pi]$ and $\lambda^{(0)} = \lambda(z(t))$ and an arbitrarily shaped smooth boundary $\Gamma^{(0)}$ in the domain D_0 having a star-like parametrization such that

$$\Gamma^{(0)} = \left\{\boldsymbol{z}^{(0)}(t) = r(t)(\cos t, \sin t) : t \in [0, 2\pi]\right\}\,, \tag{5.39}$$

where r is a smooth 2π-periodic function. Then, we set $j = 0$ for the first iteration and represent the fields by using only single-layer potentials in order to avoid an inverse crime

$$u^s(\boldsymbol{x}) = \int_{\Gamma_1} \Phi_1(\boldsymbol{x}, \boldsymbol{y})\, \varphi(\boldsymbol{y})\, ds(\boldsymbol{y}) \quad \text{in} \quad D_1\,, \tag{5.40}$$

$$u_0^{(j)}(\boldsymbol{x}) = \int_{\Gamma_1} \Phi_0(\boldsymbol{x}, \boldsymbol{y})\, \psi^{(j)}(\boldsymbol{y})\, ds(\boldsymbol{y}) + \int_{\Gamma^{(j)}} \Phi_0(\boldsymbol{x}, \boldsymbol{y})\, \chi^{(j)}(\boldsymbol{y})\, ds(\boldsymbol{y}) \quad \text{in} \quad D_0\,. \tag{5.41}$$

At this point the far-field operator is introduced by $S_\infty : L^2(\Gamma_1) \to L^2(\Omega)$

$$(S_\infty \varphi)(\boldsymbol{x}) := \frac{e^{i\pi/4}}{\sqrt{8\pi k_1}} \int_{\Gamma_1} e^{-ik_1 \boldsymbol{x}\cdot\boldsymbol{y}}\, \varphi(\boldsymbol{y})\, ds(\boldsymbol{y})\,, \qquad \boldsymbol{x} \in \Omega\,, \tag{5.42}$$

where Ω is a unit circle. From the asymptotic behavior of the single-layer potential, the far-field pattern for the solution to the inverse scattering problem is given by

$$u_\infty = S_\infty \varphi\,. \tag{5.43}$$

Now, a regularization technique has to be applied to get a stable solution for a density $\varphi \in L^2(\Gamma_1)$. Along this line we used Tikhonov regularization for the equation (5.43), as applied in (5.18) with a positive parameter α. In order to find the two unknown densities $\psi^{(j)}$ and $\chi^{(j)}$ we use the conductive boundary conditions over the boundary Γ_1 such that

$$\left.\begin{array}{l} u_0^{(j)} = u^i + u^s \\ \dfrac{\partial u^i}{\partial \boldsymbol{\nu}_1} + \dfrac{\partial u^s}{\partial \boldsymbol{\nu}_1} - \dfrac{\partial u_0^{(j)}}{\partial \boldsymbol{\nu}_1} = \lambda^{(j)}(u^i + u^s) \end{array}\right., \quad \text{on} \quad \Gamma_1 \tag{5.44}$$

that leads to an integral equation system in the operator form on Γ_1,

$$\begin{array}{l} S_{11,0}\psi^{(j)} + S_{(j)1,0}\chi^{(j)} = 2u^i|_{\Gamma_1} + S_{11,1}\varphi \\ K'_{11,0}\psi^{(j)} + \psi^{(j)} + K'_{(j)1,0}\chi^{(j)} = 2\left.\dfrac{\partial u^i}{\partial \boldsymbol{\nu}_1}\right|_{\Gamma_1} + K'_{11,1}\varphi - \varphi - \lambda^{(j)}\left(2u^i + S_{11,1}\varphi\right) \end{array}. \tag{5.45}$$

We eliminate the density $\psi^{(j)}$ from (5.45) to get

$$B_1^{(j)}\chi^{(j)} = g_1\,, \tag{5.46}$$

where $B_1^{(j)} : L^2(\Gamma^{(j)}) \to L^2(\Gamma_1)$

$$B_1^{(j)} := (I + K'_{11,0})\,S_{11,0}^{-1}S_{(j)1,0} - K'_{j1,0}\,,$$

and the right-hand side

$$g_1 := (I + K'_{11,0})\,S_{11,0}^{-1}(2u^i + S_{11,1}\varphi) - \left\{2\frac{\partial u^i}{\partial \boldsymbol{\nu}_1} + K'_{11,1}\varphi - \varphi - \lambda^{(j)}\left(2u^i + S_{11,1}\varphi\right)\right\}.$$

We consider the operator $S_{11,0}$ as a bounded operator from $L^2(\Gamma_1)$ into the Sobolev space $H^1(\Gamma_1)$ that has a bounded inverse provided k_0^2 is not a Dirichlet eigenvalue for the negative Laplacian for the interior of Γ_0 (see Theorem 3.6 in [43]). Then we applied a regularization in the sense of Tikhonov

$$\beta_1\chi^{(j)} + B_1^{*(j)}B_1^{(j)}\chi^{(j)} = B_1^{*(j)}g_1\,, \tag{5.47}$$

where $B_1^{*(j)} : L^2(\Gamma_1) \to L^2(\Gamma^{(j)})$. Substituting the density $\chi^{(j)}$ to the following equation,

$$\psi^{(j)} = S_{11,0}^{-1}\,(2u^i + S_{11,1}\varphi - S_{(j)1,0}\chi^{(j)})\,, \tag{5.48}$$

one can find $\psi^{(j)}$. Once the densities $\psi^{(j)}$ and $\chi^{(j)}$ are known the interior total field and its normal derivative on the boundary $\Gamma^{(j)}$ can be computed through the jump relations,

$$u_0^{(j)}(\boldsymbol{x}) = \int_{\Gamma_1} \Phi_0(\boldsymbol{x},\boldsymbol{y})\,\psi^{(j)}(\boldsymbol{y})\,ds(\boldsymbol{y}) + \int_{\Gamma^{(j)}} \Phi_0(\boldsymbol{x},\boldsymbol{y})\,\chi^{(j)}(\boldsymbol{y})\,ds(\boldsymbol{y})\,, \quad \boldsymbol{x} \in \Gamma^{(j)}\,, \tag{5.49}$$

and

$$\begin{aligned} \frac{\partial u_0^{(j)}}{\partial \boldsymbol{\nu}^{(j)}}(\boldsymbol{x}) &= \int_{\Gamma_1} \frac{\partial \Phi_0(\boldsymbol{x},\boldsymbol{y})}{\partial \boldsymbol{\nu}_1(\boldsymbol{x})}\,\psi^{(j)}(\boldsymbol{y})\,ds(\boldsymbol{y}) + \\ &+ \int_{\Gamma^{(j)}} \frac{\partial \Phi_0(\boldsymbol{x},\boldsymbol{y})}{\partial \boldsymbol{\nu}^{(j)}(\boldsymbol{x})}\,\chi^{(j)}(\boldsymbol{y})\,ds(\boldsymbol{y}) - \frac{1}{2}\chi^{(j)}(\boldsymbol{x})\,, \quad \boldsymbol{x} \in \Gamma^{(j)}\,. \end{aligned} \tag{5.50}$$

We carry on the inversion algorithm with the solution of an equation which can be considered as a Taylor expansion of $u_0^{(j)}$ over the boundary $\Gamma^{(j)}$ given as

$$u_0^{(j)} \circ \boldsymbol{z}^{(j)} + \left\{ \operatorname{grad} u_0^{(j)} \circ \boldsymbol{z}^{(j)} \cdot \boldsymbol{e} \right\} h^{(j)} = 0 \quad \text{on} \quad \Gamma^{(j)}\,, \quad j = 0, \ldots, J\,. \tag{5.51}$$

Here a new update function $h^{(j)}$ is defined to correct the initial guessed curve in every iteration via

$$\Gamma^{(j+1)} = \left\{ \boldsymbol{z}^{(j+1)}(t) = \boldsymbol{z}^{(j)}(t) + h^{(j)}(t)\,\boldsymbol{e}(t) : t \in [0, 2\pi] \right\}\,, \tag{5.52}$$

where $e(t) = (\cos t, \sin t)$ denotes the unit normal vector to the initial guess and h is a sufficiently small 2π-periodic function. The reconstruction of the update function with the equation (5.51) will be sensitive to errors in

$$\left\{ \operatorname{grad} u_0^{(j)} \circ \boldsymbol{z}^{(j)} \cdot \boldsymbol{e} \right\}$$

in the vicinity of zero. To obtain more stable solutions we express the unknown update function in terms of trigonometric polynomials

$$h^{(j)}(t) = \sum_{m=0}^{M} a_m^{(j)} \cos mt + b_m^{(j)} \sin mt\,, \quad t \in [0, 2\pi]. \tag{5.53}$$

Then we satisfy the equation (5.51) in the least squares sense, that is, we determine the coefficients $(a_m^{(j)}, b_m^{(j)})$ in (5.53) such that for N collocation points $t_1, t_2, t_3, \cdots, t_N$ the least squares sum

$$\sum_{n=1}^{N} \left| u_0^{(j)}(\boldsymbol{z}^{(j)}(t_n)) + \left\{ (\operatorname{grad} u_0^{(j)} \circ \boldsymbol{z}^{(j)})(t_n) \cdot \boldsymbol{e}(t_n) \right\} \sum_{m=0}^{M} (a_m^{(j)} \cos mt_n + b_m^{(j)} \sin mt_n) \right|^2 \tag{5.54}$$

is minimized. Here $t_n = 2n\pi/N$ and $n = 1, 2, 3, \cdots, N$. The number of trigonometric basis functions M in (5.54) can be considered as a kind of regularization parameter.
After the reconstructing the updated boundary $\Gamma^{(j+1)}$ we use it to find the updated value of the conductivity function $\lambda^{(j+1)}$. To this aim we solve the conductivity reconstruction problem for the known boundaries $\Gamma^{(j+1)}$ and Γ_1. In order to use simple notation we define $\ell = j+1$.
Since the density φ is found from the regularized form of the equation (5.43) we do not repeat the same step and continue with the reconstructions of the unknown densities $\psi^{(\ell)}$ and $\chi^{(\ell)}$ from the following integral equation

$$\begin{aligned} u_0^{(\ell)} &= u^i|_{\Gamma_1} + u^s|_{\Gamma_1}, \quad \text{on} \quad \Gamma_1, \\ u_0^{(\ell)} &= 0, \qquad\qquad\qquad \text{on} \quad \Gamma^{(\ell)}, \end{aligned} \tag{5.55}$$

which leads to an integral equation system that has to be solved in the sense of Tikhonov

$$\begin{aligned} &S_{11,0}\psi^{(\ell)} + S_{(\ell)1,0}\chi^{(\ell)} = 2u^i|_{\Gamma_1} + S_{11,1}\varphi, \quad \text{on} \quad \Gamma_1, \\ &S_{1(\ell),0}\psi^{(\ell)} + S_{(\ell)(\ell),0}\chi^{(\ell)} = 0, \quad \text{on} \quad \Gamma^{(\ell)}. \end{aligned} \tag{5.56}$$

Similarly to previous regularization step we write the following integral equation with the operator defined $B_2^{(\ell)} : L^2(\Gamma^{(\ell)}) \to L^2(\Gamma_1)$

$$B_2^{(\ell)}\chi^{(\ell)} = g_2\,. \tag{5.57}$$

Here

$$B_2^{(\ell)} := S_{1(\ell),0} S_{11,0}^{-1} S_{(\ell)1,0} - S_{(\ell)(\ell),0}\,,$$

and

$$g_2 := S_{1(\ell),0} S_{11,0}^{-1} (2u^i + S_{11,1}\varphi)\,.$$

We again interpret the operator $S_{11,0}$ as a bounded operator from $L^2(\Gamma_1)$ into the Sobolev space $H^1(\Gamma_1)$ that has a bounded inverse provided k_0^2 is not a Dirichlet eigenvalue for the negative Laplacian for the interior of Γ_1 (see Theorem 3.6 in [43]). Then we obtain the following equation for the density $\chi^{(\ell)}$.

$$\beta_2 \chi^{(\ell)} + B_2^{*(\ell)} B_2^{(\ell)} \chi^{(\ell)} = B_2^{*(\ell)} g_2 \,. \tag{5.58}$$

By substituting $\chi^{(\ell)}$ to the following equation,

$$\psi^{(\ell)} = S_{11,0}^{-1} (2u^i + S_{11,1}\varphi - S_{(\ell)1,0}\chi^{(\ell)}) \,, \tag{5.59}$$

one can compute the density $\psi^{(\ell)}$, numerically. Finally, to reconstruct the updated conductivity function $\lambda^{(\ell)}$, from the equation (5.30) the total field expressions over the boundary Γ_1 are given under the jump conditions as

$$u_1(\boldsymbol{x}) = u^i(\boldsymbol{x}) + \int_{\Gamma_1} \Phi_1(\boldsymbol{x},\boldsymbol{y})\, \varphi(\boldsymbol{y})\, ds(\boldsymbol{y}) \,, \quad \boldsymbol{x} \in \Gamma_1 \,, \tag{5.60}$$

$$\frac{\partial u_1}{\partial \boldsymbol{\nu}_1}(x) \;=\; \frac{\partial u^i}{\partial \boldsymbol{\nu}_1}(\boldsymbol{x}) + \int_{\Gamma_1} \frac{\partial \Phi_1(\boldsymbol{x},\boldsymbol{y})}{\partial \boldsymbol{\nu}_1(\boldsymbol{x})}\, \varphi(\boldsymbol{y})\, ds(\boldsymbol{y}) - \frac{1}{2}\varphi(\boldsymbol{x}) \,, \quad \boldsymbol{x} \in \Gamma_1 \,, \tag{5.61}$$

$$\begin{aligned} \frac{\partial u_0^{(\ell)}}{\partial \boldsymbol{\nu}^{(\ell)}}(\boldsymbol{x}) &= \int_{\Gamma_1} \frac{\partial \Phi_0(\boldsymbol{x},\boldsymbol{y})}{\partial \nu_1(\boldsymbol{x})}\, \psi^{(\ell)}(\boldsymbol{y})\, ds(\boldsymbol{y}) + \frac{1}{2}\psi^{(\ell)}(\boldsymbol{x}) \\ &+ \int_{\Gamma^{(\ell)}} \frac{\partial \Phi_0(\boldsymbol{x},\boldsymbol{y})}{\partial \boldsymbol{\nu}^{(\ell)}(\boldsymbol{x})}\, \chi^{(\ell)}(\boldsymbol{y})\, ds(\boldsymbol{y}) \,, \quad \boldsymbol{x} \in \Gamma_1 \,. \end{aligned} \tag{5.62}$$

The reconstruction of the $\lambda^{(\ell)}$ will be sensitive to errors in u_1 in the vicinity of zero. To obtain a more stable solution, we express the unknown function $\lambda^{(\ell)}$ in terms of trigonometric basis functions $\kappa_r(t) = e^{irt}$, $r = 0, \pm 1, \pm 2, \ldots, \pm R$, as a linear combination

$$\lambda^{(\ell)} = \sum_{r=-R}^{R} \tau_r \kappa_r \,. \tag{5.63}$$

Then equation (5.30) is satisfied in the least squares sense, that is, the coefficients $\tau_{-R}, \ldots, \tau_R$ in (5.63) are determined when for a set of grid points $t_1, t_2, \ldots, t_N$ on $[0, 2\pi]$ the least squares sum

$$\sum_{n=1}^{N} \left| \left\{ \frac{\partial u_1}{\partial \boldsymbol{\nu}}(z_1(t_n)) - \frac{\partial u_0}{\partial \boldsymbol{\nu}}(z_1(t_n)) \right\} - \sum_{r=-R}^{R} \tau_r \kappa_r(t_n)\, u_1(z_1(t_n)) \right|^2 \tag{5.64}$$

is minimized. The highest degree of basis functions R in (5.63) can be considered as some kind of an additional regularization parameter.

In the next iteration we solve the regularized equation given in (5.47) for the updated conductivity function $\lambda^{(\ell)}$ to obtain $\Gamma^{(j+2)}$ and follow the same procedure up to this point. Iterations continue until desired stopping criterias (SC_1, SC_2) such that

$$SC_1 = \sum_{m=0}^{M} \frac{|a_m^{(j)} - a_m^{(j-1)}|}{M+1} + \sum_{m=1}^{M} \frac{|b_m^{(j)} - b_m^{(j-1)}|}{M} < \bar{\varepsilon}_1 \,, \tag{5.65}$$

and

$$SC_2 = \sum_{r=-R}^{R} \frac{|\lambda^{(\ell)} - \lambda^{(\ell-1)}|}{2R+1} < \bar{\varepsilon}_2 \,, \tag{5.66}$$

are both fullfilled for sufficiently small $\bar{\varepsilon}_1$ and $\bar{\varepsilon}_2$ numbers.

5.8 Numerical Results

In this section we test the proposed reconstruction algorithm. For all numeric applications arbitrarily shaped smooth cylinders from Table 1 and $N = 64$ collocation points are used. Tikhonov regularization parameters are chosen by trial error and they are denoted by α for the regularized form of the equation (5.43) and β_1, β_2 for the equations (5.47) and (5.58) respectively.

The degree of the polynomials for the shape is M and for the conductivity function is R. Furthermore, for the experiments of this problem we only use exact data during our numerical simulations and apply percentage error expressions defined in (3.25) and (4.31) for the conductivity function ERR^{λ} and for the shape ERR^{Γ_0}, respectively.

Except for the first experiment we choose initial guess $\Gamma^{(0)}$ as a circle with radius $c_0 = 0.6$ and $\lambda^{(0)} = 0.5$ as a constant line for the solution of the inverse problem.

Experiment 1: First of all, we want to test the reconstruction algorithm from the knowledge of the far-field by choosing initially guessed boundary $\Gamma^{(0)}$ and the function $\lambda^{(0)}$ the same as actual shape Γ_0 and conductivity function λ in order to observe the convergence and the ill-posedness of the problem. Therefore we run the algorithm up to 200 iterations after choosing a PEC obstacle as a peanut shape scatterer $\Gamma_0 = \Gamma^{(p)}$ buried in a rounded rectangular cylinder $\Gamma_0 = \Gamma^{(r)}$ for the wave numbers $k_0 = 2$, $k_1 = 1.5$ with the illumination angle $\phi_0 = 0^0$.

We use regularization parameters $\alpha = 10^{-14}$, $\beta_1 = 10^{-3}$, $\beta_2 = 10^{-10}$, $M = 3$, $R = 2$. Now we are in a point to introduce Figure 5.6 constructed by the calculations of the expressions (5.65), (5.66) that illustrates the monotonous decreasing absolute

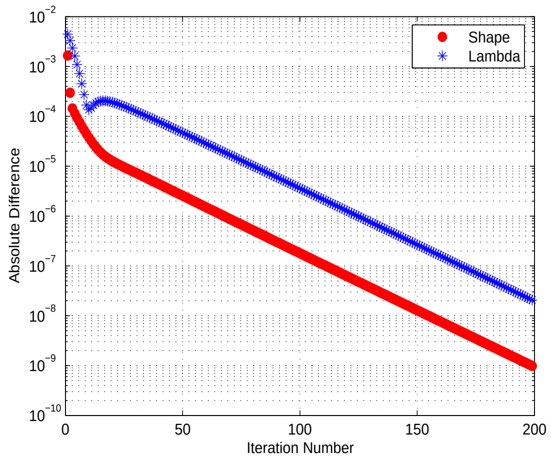

Figure 5.6: Convergence rate of the $\Gamma^{(j)}$ and $\lambda^{(\ell)}$ for the test configuration

difference of the shape update parameters and reconstructed conductivity functions according to number of iterations. In this example, due to the approximations in the

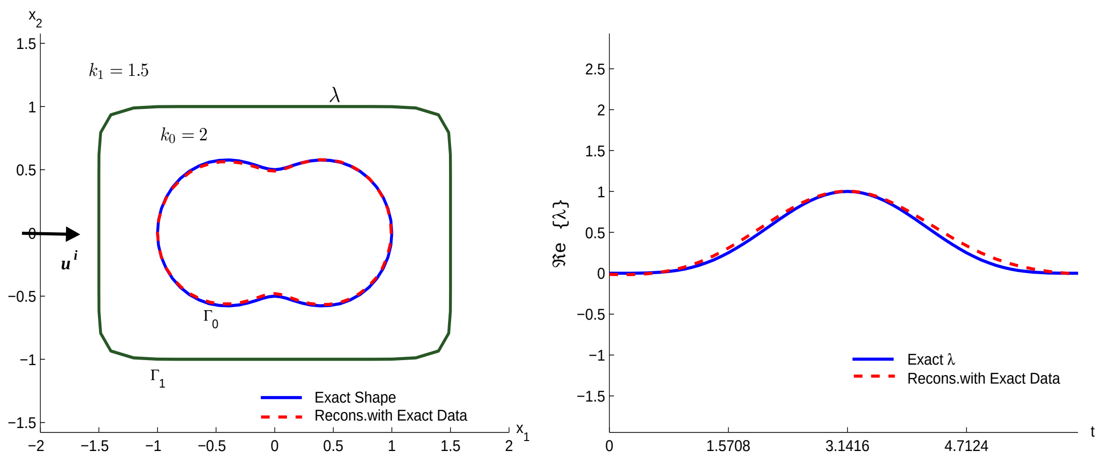

Figure 5.7: Reconstruction of the peanut shaped object buried in a rounded rectangular shaped cylinder for $\lambda(z(t)) = \sin^4(t/2)$ from the far-field

solutions of the ill-posed integral equations we do not find exactly the actual shapes even we choose the initial guesses as exact values of the functions which have to be reconstructed and obtain $ERR^{\Gamma_0} \approx 1.410$, $ERR^{\lambda} \approx 8.910$ percentage errors, see Figure 5.7. However, the reconstructions can be considered stable and acceptable as compare to high ill-posedness of the problem for large number of iterations.

Experiment 2: In the second experiment we test the reconstruction algorithm with simple initial guesses. Therefore we choose initially guessed shape as a circle and $\lambda^{(0)}$ as a line.

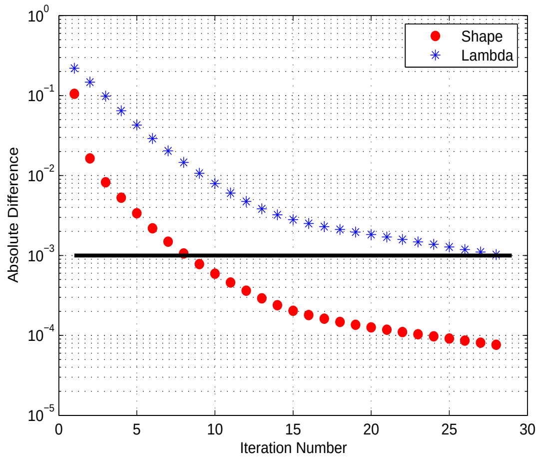

Figure 5.8: Convergence rate of the $\Gamma^{(j)}$ and $\lambda^{(\ell)}$ for experiment-2

The problem configuration parameters are kept the same as defined in the experiment 1, such as $k_0 = 2$, $k_1 = 1.5$, $\phi_0 = 0^0$. For the reconstructions the far-field data is used and stopping criteria bounds $\bar{\varepsilon}_1 = \bar{\varepsilon}_2 = 10^{-3}$ are considered. We choose the regularization

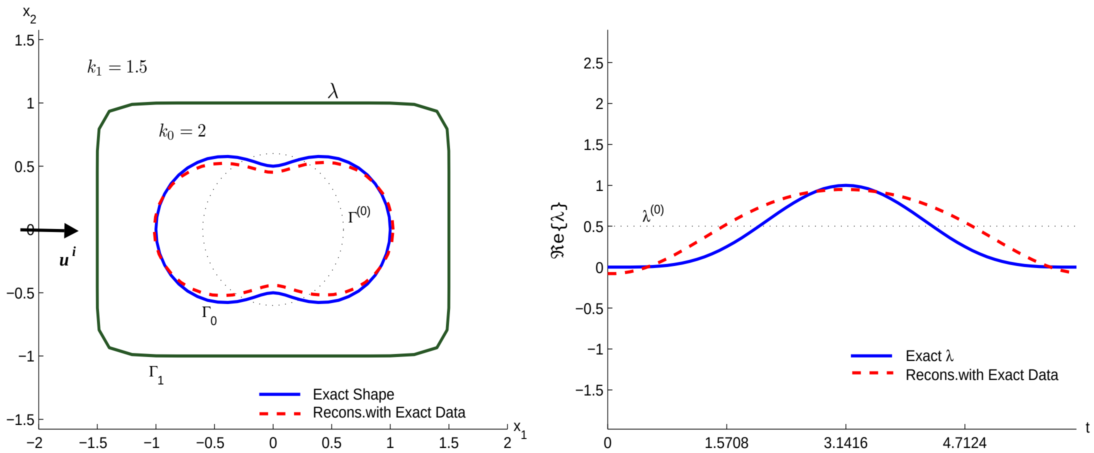

Figure 5.9: Reconstruction of the peanut shaped object buried in a rounded rectangular shaped cylinder for $\lambda(z_1(t)) = \sin^4(t/2)$ from the far-field

parameters $\alpha = 10^{-14}$, $\beta_1 = \beta_2 = 10^{-3}$, $M = 3$, $R = 2$ and obtain after $\ell = 30$ iterations the convergence speed of the reconstructed shapes and conductivity functions as given in Figure 5.8 with the percentage errors $ERR^{\Gamma_0} \approx 6.288$, $ERR^{\lambda} \approx 32.340$, see Figure 5.9.

Experiment 3: In this experiment we use the same problem configuration and the problem parameters as stated in the previous example. The only difference now we compute the scattered field over a measurement circle Ω^m having a radius $c_0 = 3$ and set $\alpha = 10^{-10}$. Under these conditions after $\ell = 25$ iterations results fulfill the desired criteria for $\bar{\varepsilon}_1 = \bar{\varepsilon}_2 = 10^{-3}$, see Figure 5.10. Then we obtain $ERR^{\Gamma_0} \approx 2.408$ and $ERR^{\lambda} \approx 5.861$ as illustrated Figure 5.11.

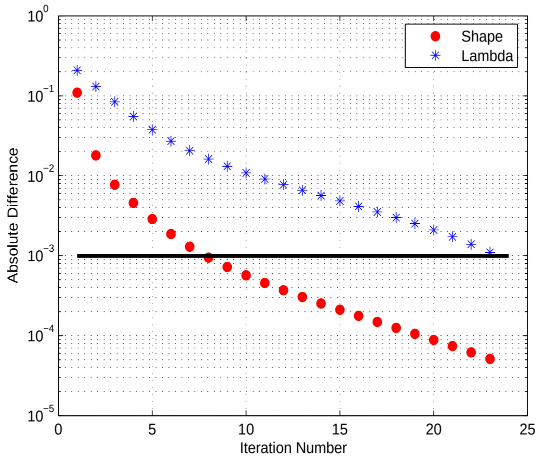

Figure 5.10: Convergence rate of the $\Gamma^{(j)}$ and $\lambda^{(\ell)}$ for experiment-3

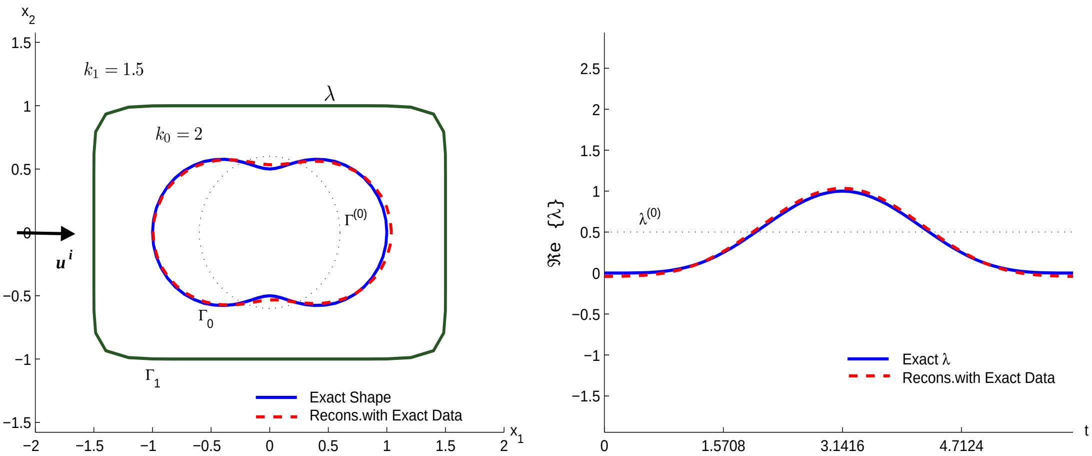

Figure 5.11: Reconstruction of the peanut shaped object buried in a rounded rectangular shaped cylinder for $\lambda(z_1(t)) = \sin^4(t/2)$ from the near-field

Experiment 4: Now, we change the exterior cylinder to a $\Gamma_1 = \Gamma^{(t)}$ rounded triangular shaped object and keep the rest of the problem geometry the same as the experiment 1, with parameters $k_0 = 2$, $k_1 = 1.5$, $\phi_0 = 0^0$. For the reconstructions we use far-field data. Since we set the criterias $\bar{\varepsilon}_1 = \bar{\varepsilon}_2 = 10^{-4}$ the algorithm stops after $\ell = 85$ iterations, see Figure 5.12, for the regularization parameters $\alpha = 10^{-8}$, $\beta_1 = \beta_2 = 10^{-3}$, $M = 4$, $R = 2$. We obtain $ERR^{\Gamma_0} \approx 5.987$ and $ERR^{\lambda} \approx 34.834$ percentage, see Figure 5.13. This example shows that in the case of choosing all parameters optimally according to the problem under investigation the reconstruction algorithm can fulfill the stopping criteria both for the shape and the conductivity function $\bar{\varepsilon}_1 = \bar{\varepsilon}_2 = 10^{-4}$ for complex shapes with a conductivity function having slow variations.

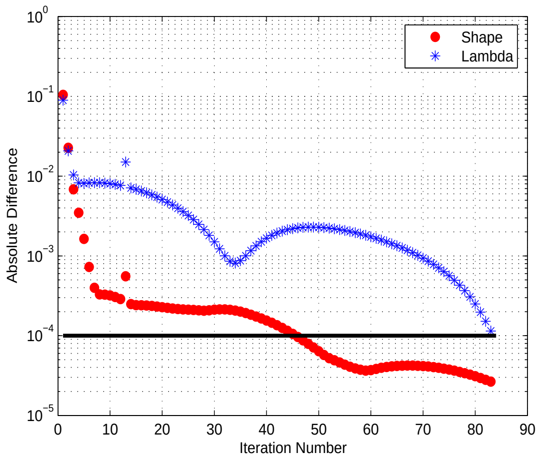

Figure 5.12: Convergence rate of the $\Gamma^{(j)}$ and $\lambda^{(\ell)}$ for experiment-4

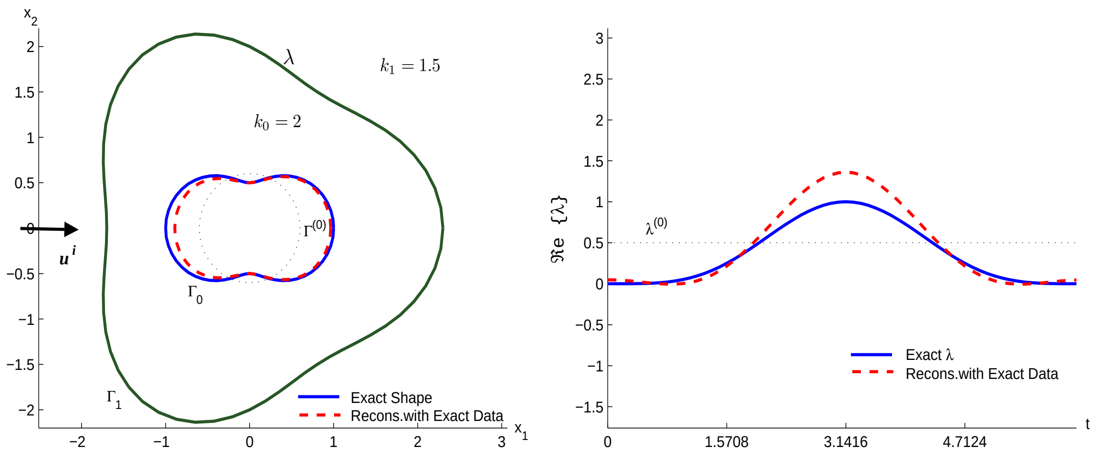

Figure 5.13: Reconstruction of the peanut shaped object buried in a rounded triangular shaped cylinder for $\lambda(z_1(t)) = \sin^4(t/2)$ from far-field

Experiment 5: The final experiment is devoted for the observation of the quality of

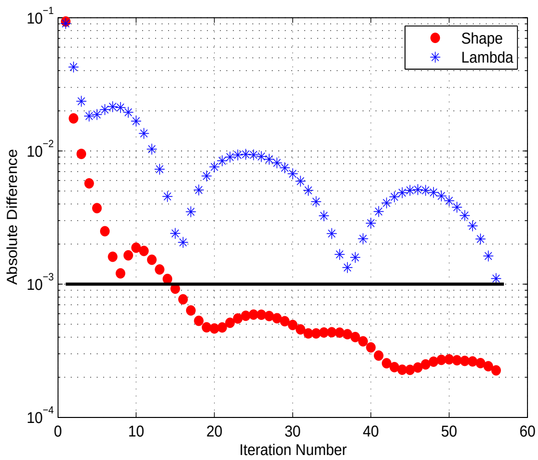

Figure 5.14: Convergence rate of the $\Gamma^{(j)}$ and $\lambda^{(\ell)}$ for experiment-5

the reconstructions in the case of using near-field data for the problem investigated in experiment 4. Therefore we collected the scattered field data on a measurement circle

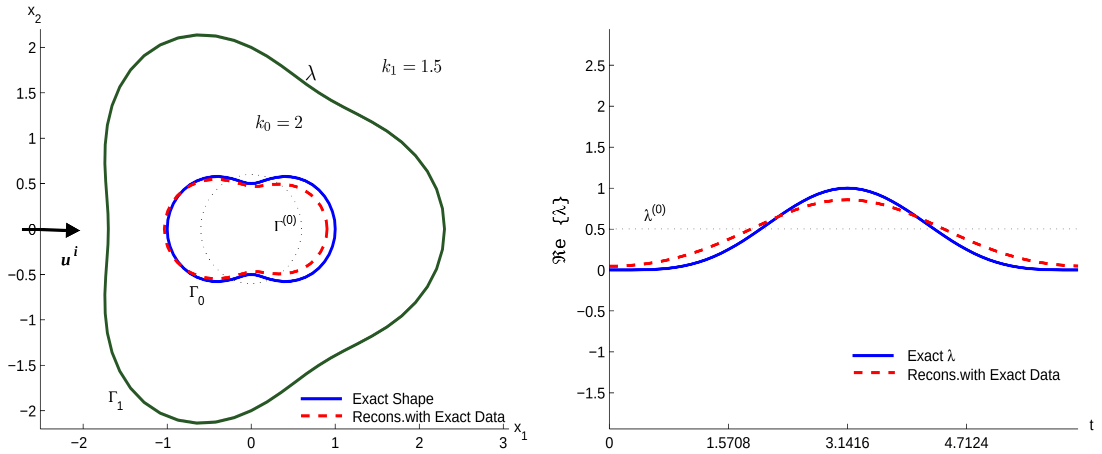

Figure 5.15: Reconstruction of the peanut shaped object buried in a rounded triangular shaped cylinder for $\lambda(z_1(t)) = \sin^4(t/2)$ from near-field

Ω^m with radius $c_0 = 3$ for the wave numbers $k_0 = 2$, $k_1 = 1.5$, with the illumination angle $\phi_0 = 0^0$. We obtain $ERR^{\Gamma_0} \approx 8.698$ and $ERR^{\lambda} \approx 23.472$ percentage errors after $\ell = 58$ iterations for the parameters $\alpha = 10^{-10}$, $\beta_1 = \beta_2 = 10^{-3}$, $M = 4$, $R = 2$.

5.9 Comments on Numerical Results

The main idea of proposing this reconstruction algorithm is to generalize and combine the inversion algorithms given in chapter 3 and chapter 4. However, we do not borrow the location reconstruction algorithm from the chapter 4 and focus on the shape reconstructions of the buried objects having a priori knowledge on the locations of them to reduce the complexity of the main problem. Therefore, the problems studied in the previous mentioned chapters can be considered as special cases of the problem defined here. Moreover the problem is original and some recent publications on similar problems in 2008 [96, 97] shows that it is worthy of investigation.

First of all, it is concluded from the numerical experiments that the proposed reconstruction algorithm works for the exact data and one can obtain stable, convergent and acceptable results via proposed algorithm in the case of using all arbitrarily chosen parameters optimally for an appropriate problem. However, because of the problem contains simultaneous solutions of two ill-posed problems in each iteration the reconstructions are highly dependent on the selection of the parameters. Hence, improving the algorithm and finding reconstructions from noisy data is still in progress.

We observe that in all experiments shape problem has a faster convergence behavior than conductivity function reconstruction problem. This is a result of the success of the shape reconstruction algorithm. Therefore we can reconstruct complex shaped obstacles but we only can find some conductivity functions having slow variations. Along this line, we believe that one of the main contribution to improve the reconstruction algorithm will be defining a direct and efficient relation between the shape function and the conductivity function. This strategy allow us to eliminate the repeating the conductivity reconstruction algorithm in every iteration.

During on the construction of the main algorithm we also tried to change the solution order of the problems such that we first solve the conductivity function reconstruction problem using only initially guessed boundary. In this case, although we do not need to search another good guess for the conductivity function we could not obtain acceptable results.

The other techniques which may increase the quality and the stability of the reconstructions in inverse scattering theory is the employment of the multiple illuminations or obtaining more information from the illuminations via different frequencies. We plan to apply these approaches to the problem considered in this section.

We expect to have more accurate results by using near-field data and this idea is supported by the results in experiment 3. However the results obtained by experiment 5 shows a contradiction since we have less accuracy for the shape reconstruction with near-field data than by using far-field data.

Finally, these numerical investigations illustrate the early results of our studies on this problem but the progress gives enough positive signs to motivate us for spending some more effort on the improvement of the reconstruction algorithm.

6. CONCLUSIONS

In this chapter we summarize the work which has been done, clarify the contributions of the thesis to the literature and point out possible future studies.

In the thesis,

- impedance,
- location,
- shape,
- conductivity function,

reconstruction problems related to arbitrarily shaped obstacles buried in given arbitrarily shaped penetrable cylinders for single plane wave illumination at fixed frequency in the resonance region were investigated. 2-D geometries were considered and it was assumed impedance boundary condition or the Dirichlet boundary condition on the buried obstacle and transmission or conductive boundary condition on the penetrable cylinder depending on the type of the problem. Boundary integral equations via different potential approaches were derived and in order to obtain reconstructions they were solved numerically by the help of effective methods. The numerical applications performed with a standard PC on the level of few minutes. However the programs code can be optimized or can be run in highly developed computers that will provide computational time on the level of seconds which does not belong to the scope of the thesis research. The numerical correctness of the solutions of forward problems is guaranteed by comparing our results with some reduced problem solutions. The reconstructions were obtained by solving the nonlinear and ill-posed integral equations via some regularizations with the parameters chosen by trial and error. Furthermore we provide the papers [85, 92, 94] for theoretical investigations of the impedance and conductivity reconstruction problems.

One of the main contribution of this study is to introduce a new inversion method to reconstruct the total fields in every region for the presented configuration of the scatterers from the far-/near-field for one plane wave illumination. Thus, the knowledge of the fields can be used to find the spatial coordinates or the characteristic(impedance/conductivity) functions defined on the boundary of the scatterers by using Newton iterative methods [56] or recently published algorithms [82, 94]. In this context, we combine the new algorithm with the just referred methods and show that for a new and one typical inverse problem satisfactory reconstructions were obtained with 3% noisy scattered field data.

Further results of the thesis are listed below:

i. Solutions of each forward problem for the considered configuration in the thesis have enough importance to provide synthetic scattered field (far/near) data for researchers.

ii. Generalized versions that includes singular and non-singular forms of the well-known boundary integral operators S, K, K', T are introduced for two boundaries.

iii. Impedance reconstruction problem for the arbitrarily shaped objects buried in dielectric cylinders has been considered in [85] for the first time.

iv. A new algorithm is proposed for the location reconstructions of the PEC obstacles buried in dielectric cylinders [89].

v. There are only few studies both for the location and shape reconstruction problem and they use strong assumptions e.g. multi-illumination, multi-frequency, high conductivity etc. in the literature because of the mathematical and computational complexity. On the other hand our method proposed in chapter 4 yields reasonable results with single illumination at fixed frequency even with scattered field noisy data given in the range of angle π under weaker restrictions mentioned before. We also should point out that in previous studies depending on [56] all the scatterers stay in free-space and the more realistic case of buried objects has been firstly presented by Yaman in 2008 in the Spring Conference Widening Horizons in Acoustic Research [88].

vi. Shape and conductivity function reconstruction problem is introduced firstly in the current study.

It can be concluded from the reported numerical results that proposed methods for each corresponding problem provide accurate reconstructions with the full scattered field data contains up to 3% of random noise. The problems investigated in the thesis are sufficiently good approximate models of practical applications. Therefore it is believed that the presented numerical simulations can also be perform with real scenarios. Another future work which can be considered is to extend the methods presented in the thesis to 3-D geometries or to a larger number of penetrable layers. Furthermore the case when buried obstacles are replaced by cracks will also corresponds to a valuable problem from practical point of view.

REFERENCES

[1] **Groetsch, C.W.**, 1993. *Inverse problems in the mathematical sciences*, Vieweg & Sohn Verlagsgesselschaft mbH, Braunschweig/Wiesbaden.

[2] **Hadamard, J.**, 1923. *Lectures on Cauchy's problem in linear partial differential equations*, Yale Univ. Press, New Haven.

[3] **Groetsch, C.W.** , 2007. Integral equations of the first kind, inverse problems and regularization: a crash course, *Journal of Physics: Conference Series*, **73**, 1–32.

[4] **Newton, R.G.**, 1970. Inverse problems in physics, *SIAM Review*, **12**, 346–356.

[5] **Parker, R.L.**, 1977. Understanding inverse theory, *Annual Review, Earth Planet Sci.*, **5**, 35–64.

[6] **Kirsch A.**, 1996. *An introduction to the mathematical theory of inverse problems*, Springer-Verlag New York, Inc.

[7] **Colton, D.**, 2003. Inverse acoustic and electromagnetic scattering theory, *Inside Out: Inverse Problems and Applications*, **47**, 67–110.

[8] **Boerner W.M.**, **Jordan A.K. and Kay I.W.**, 1981. Introduction to the special issue on inverse methods in electromagnetics, *IEEE Trans. on Antennas and Prop.*, **29**, 185–189.

[9] **Colton, D.**, **Coyle, J. and Monk, P.**, 2000. Recent developments in inverse acoustic scattering theory, *SIAM Review*, **42**, 3, 369–414.

[10] **Kress, R.**, 1997. Numerical methods in inverse obstacle scattering, *Inverse Problems of Wave Propagation and Diffraction*, **486**, 93–106.

[11] **Kress, R.**, 2000. Integral equation methods in inverse obstacle scattering, *Anziam Journal*, **42**, 65-78.

[12] **Kress, R.**, 2000. Numerical methods in inverse obstacle scattering, *Anziam Journal* **42**, C44-C67.

[13] **Kabanikhin, S. I.**, 2003. Definitions and examples of inverse and ill-posed problems, *Jour. of Inv. and Ill-Posed Problems*, **16**, 317–357.

[14] **Colton, D. and Kress, R.**, 2006. Using fundamental solutions in inverse scattering, *Inverse Problems*, **22**, R49–R66.

[15] **Potthast, R.**, 2006. A survey on sampling and probe methods for inverse problems, *Inverse Problems*, **22**, R1–R47.

[16] **Kress, R.**, 2007. Uniqueness and numerical methods in inverse obstacle scattering, *Journal of Physics: Conference Series*, **73**, 1–16.

[17] **Cakoni, F.**, 2007. Recent developments in the qualitative approach to inverse electromagnetic scattering theory, *Journal of Computational and Applied Mathematics*, **204**, 242–255.

[18] **Roger, A.**, 1981. Newton-Kantorovitch algorithm applied to an electromagnetic inverse problem, *IEEE Trans. on Anten. and Prop.*, **29**, 2, 232–238.

[19] **Murch, R. D.**, **Tan, D. G. H. and Wall, D. J. N.**, 1998. Newton-Kantorovich method applied to two-dimensional inverse scattering for an exterior Helmholtz problem, *Inverse Problems*, **4**, 1117–1128.

[20] **Tobocman, W.**, 1989. Inverse acoustic wave scattering in two dimensions from impenetrable targets, *Inverse Problems*, **5**, 1131–1144.

[21] **Wang, S. L.**, **and Chen, Y. M.**, 1991. An efficient numerical method for exterior and interior inverse problems of Helmholtz equation, *Wave Motion*, **13**, 387–399.

[22] **Kirsch, A.**, 1993. The domain derivative and two applications in inverse scattering theory, *Inverse Problems*, **9**, 81–96.

[23] **Kress, R.**, 1994. A Newton method in inverse obstacle scattering, *Inverse Problems in Engineering Mechanics (Bui et al eds.)*, Balkema, Rotterdam 425–432.

[24] **Kress, R. and Rundell, W.**, 1994. A quasi-Newton method in inverse obstacle scattering, *Inverse Problems*, **10**, 1145–1157.

[25] **Kress, R.**, 1995. Integral equation methods in inverse obstacle scattering, *Engineering Anal. with Boundary Elements*, **15**, 171–179.

[26] **Kress, R.**, 1997. Integral equation methods in inverse acoustic and electromagnetic scattering, *Boundary Integral Formulations for Inverse Analysis(Ingham and Wrobel eds)*, Computational Mechanics Publications, Southampton, 67–92.

[27] **Hettlich, F**, 1996 An iterative method for the inverse scattering problem from sound-hard obstacles. *In: Proceedings of the ICIAM 95, Vol II, Applied Analysis (Mahrenholz and Mennicken, eds)* Akademie Verlag, Berlin.

[28] **Mönsch, L.**, 1996. A Newton method for solving the inverse scattering problem for a sound-hard obstacle, *Inverse Problems*, **12**, 309–323.

[29] **Hohage, H.**, 1997. Logarithmic convergence rates of the iteratively regularized Gauss-Newton method for an inverse potential and an inverse scattering problem, *Inverse Problems*, **13**, 1279–1299.

[30] **Kress, R. and Rundell, W.**, 1998. Inverse obstacle scattering using reduced data, *Siam J. Appl. Math.*, **59**, 442–454.

[31] **Hohage, T.**, 1998 Convergence rates of a regularized Newton method in sound-hard inverse scattering, *Siam J. Numer. Analy.*, **36**, 125–142.

[32] **Hohage, T.**, 1999. *Iterative methods in inverse obstacle scattering: regularization theory of linear and nonlinear exponentially ill-posed problems*, Dissertation, Linz 1999.

[33] **Potthast, R.**, 2001. On the convergence of a new Newton-type method in inverse scattering, *Inverse Problems*, **17**, 1419–1434.

[34] **Farhat, C.**, **Tezaur R. and Djellouli, R.**, 2002. On the solution of three-dimensional inverse obstacle acoustic scattering problems by a regularized Newton method, *Inverse Problems*, **18**, 1229–1246.

[35] **Harbrecht, H. and Hohage, T.**, 2007. Fast methods for three-dimensional inverse obstacle scattering problems, *J. Integral Equations Appl.*, **19**, 237–260.

[36] **Kress, R. and Rundell, W.**, 2005. Nonlinear integral equations and the iterative solution for an inverse boundary value problem, *Inverse Problems*, **21**, 1207–1223.

[37] **Ivanyshyn O. and Kress, R.**, 2006. Nonlinear integral equations in inverse obstacle scattering, *In: Mathematical Methods in Scattering Theory and Biomedical Engineering (Fotiatis, Massalas, eds.) World Scientific*, Singapore, 39-50.

[38] **Ivanyshyn, O. and Kress, R.**, 2006. Nonlinear integral equations for solving inverse boundary value problems for inclusions and cracks, *J. Integral Equations Appl.*, **18**, 13–38.

[39] **Ivanyshyn, O. and Johansson, T.**, 2007. Nonlinear integral equation methods for the reconstruction of an acoustically sound-soft obstacle, *J. Integral Equations Appl.*, **19**, 289–308.

[40] **Ivanyshyn, O.**, 2007. Shape reconstruction of acoustic obstacles from the modulus of the far field pattern, *Inverse Problems and Imaging*, **1**, 609–622.

[41] **Ivanyshyn, O.**, 2007. *Nonlinear Boundary Integral Equations in Inverse Scattering,* PhD thesis, University of Göttingen.

[42] **Johansson, T. and Sleeman, B. D.**, 2007. Reconstruction of an acoustically sound-soft obstacle from one incident field and the far-field pattern, *IMA J. of Appl. Math.*, **72**, 96–112.

[43] **Colton, D. and Kress, R.**, 1998. *Inverse acoustic and electromagnetic scattering theory, 2nd. ed.*, Springer Verlag, Berlin.

[44] **Kress, R.**, 1998. *Linear integral equations 2nd. ed*, Springer Verlag, Berlin.

[45] **Hanke, M.**, **Neubauer, A. and Scherzer, O.**, 1995. A convergence analysis for the Landweber iteration for nonlinear ill-posed problems, *Numerical Math.*, **72**, 21–37.

[46] **Colton, D. and Monk, P.**, 1985. A novel method for solving the inverse scattering problem for time-harmonic acoustic waves in the resonance region, *Siam J. Appl. Math*, **45** , 1039–1053.

[47] **Colton, D. and Monk, P.**, 1986. A novel method for solving the inverse scattering problem for time-harmonic acoustic waves in the resonance region II, *Siam J. Appl. Math*, **46** , 506–523.

[48] **Colton, D. and Monk, P.**, 1987. The Numerical Solution of the Three-Dimensional Inverse Scattering Problem for Time Harmonic Acoustic Waves *SIAM J. Sci. and Stat. Comput.*, **8**, 278–291.

[49] **Kirsch, A. and Kress, R.**, 1986. On an integral equation of the first kind in inverse acoustic scattering, *Inverse Problems (Cannon and Hornung, eds.)*, **77**, 93–102.

[50] **Kirsch, A. and Kress, R.**, 1987. A numerical method for an inverse scattering problem. *Inverse Problems (Engl and Groetsch, eds.)*, 279–290.

[51] **Kirsch, A. and Kress, R.**, 1987. An optimization method in inverse acoustic scattering. *Boundary Elements IX, Vol.3 Fluid Flow and Potential Applications (Brebbia et al.,eds)*, 3–18.

[52] **Çayören, M.**, **Akduman, I.**, **Yapar, A. and Crocco, L.**, 2007. A new algorithm for the shape reconstruction of perfectly conducting objects, *Inverse Problems*, **23**, 1087–1100.

[53] **Angell, T. S.** , **Kleinmann, R. E. and Roach, G.F.**, 1987. An inverse transmission problem for the Helmholtz equation, *Inverse Problems*, **3**, 149–180.

[54] **Angell, T. S.** , **Kleinmann, R. E.**, **Kok, B. and Roach, G.F.**, 1989. A constructive method for identification of an impenetrable scatterer, *Wave Motion*, **11**, 185–200.

[55] **Jones, D. S. and Mao, X. Q.**, 1989. The inverse problem in hard acoustic scattering, *Inverse Problems*, **5**, 731–748.

[56] **Kress, R.**, 2003. Newton's method for inverse obstacle scattering meets the method of least squares, *Inverse Problems*, **19**, 91–104 .

[57] **Serranho, P.**, 2006. A hybrid method for inverse scattering for shape and impedance, *Inverse Problems*, **22**, 663–680.

[58] **Kress, R. and Serranho, P.**, 2007. A hybrid method for sound-hard obstacle reconstruction, *J. Comput. Appl. Math.* , **204**, 418–427.

[59] **Serranho, P.**, 2007. A hybrid method for inverse scattering for sound-soft obstacles in 3D, *Inverse Problems and Imaging*, **1**, No:4, 691–712.

[60] **Serranho, P.**, 2007. *A hybrid method for inverse obstacle scattering problems*, PhD thesis, University of Göttingen.

[61] **Kress, R.**, **Tezel, N. and Yaman, F.**, 2009. A second order Newton method for sound-soft inverse obstacle scattering, *Jour. of Inv. and Ill-Posed Problems*, **17**, 173-185.

[62] **Potthast, R.**, 1996. A fast new method to solve inverse scattering problems, *Inverse Problems*, **12**, 731–742.

[63] **Potthast, R.**, 1998. A point source method for inverse acoustic and electromagnetic obstacle scattering problems, *IMA J. Appl. Math.*, **61**, 119–140.

[64] **Potthast, R.**, 2001. *Point sources and multipoles in inverse scattering theory,* Chapman & Hall/Crc Statistics and Mathematics, London.

[65] **Colton, D. and Kirsch, A.**, 1996. A simple method for solving inverse scattering problems in the resonance region, *Inverse Problems*, **12**, 383–393.

[66] **Colton, D.**, **Piana, M. and Potthast, R.**, 1997. A simple method using Morozov's discrepancy principle for solving inverse scattering problems, *Inverse Problems*, **13**, 1477–1493.

[67] **Kress, R. and Kühn, L.**, 2002. Linear sampling methods for inverse boundary value problems in potential theory, *Appl. Num. Math.*, **43**, 161–173.

[68] **Arens, T.**, 2004. Why linear sampling works, *Inverse Problems*, **20**, 163–173.

[69] **Kirsch, A.**, 1998. Characterization of the shape of a scattering obstacle using the spectral data of the far field operator, *Inverse Problems*, **14**, 1489–1512.

[70] **Kirsch, A. and Grinberg, N.**, 2008. *The factorization method for inverse problems,* Oxford Univer. Press, Inc. New York.

[71] **Potthast, R.**, 2000. Stability estimates and reconstructions in inverse acoustic scattering using singular sources, *J. of Comp. and Appl. Math.*, **114**, 247–274.

[72] **Ikehata, M.**, 1998. Reconstruction of an obstacle from the scattering amplitude at a fixed frequency, *Inverse Problems*, **14**, 949–954.

[73] **Ikehata, M.**, 1999. Reconstruction of obstacle from boundary measurements, *Wave Motion*, **30**, 205–223.

[74] **Ikehata, M.**, 1999. Enclosing a polygonal cavity in a two-dimensional bounded domain from Cauchy data, *Inverse Problems*, **15**, 1231–1241.

[75] **Ikehata, M.**, 1999. Reconstruction of a source domain from the Cauchy data, *Inverse Problems*, **15**, 637–645.

[76] **Luke, D. R. and Potthast, R.**, 2003. The no response test - a sampling method for inverse scattering problems, *SIAM J. Appl. Math.*, **63**, 1292–1312.

[77] **Potthast, R.**, 2004. A set-handling approach for the no-response test and related methods, *Math. Comput. Simul.*, **66**, 281–295.

[78] **Potthast, R.**, 2007. On the convergence of the no response test, *SIAM J. Math. Anal.*, **38**, 1808–1824.

[79] **Colton, D. and Kirsch, A.**, 1981. The determination of the surface impedance of an obstacle from measurements of the far field pattern, *SIAM J. on Appl. Math.*, **41**, 8–15.

[80] **Kedzierawski, A. W.**, 1992. The determination of the surface impedance of an obstacle *Proceedings of the Edinburgh Math. Soc.*, 35, 1-15

[81] **Haddar, H. and Kress, R.**, 2005. On the Fréchet derivative for obstacle scattering with an impedance boundary condition, *SIAM J. on Appl. Math.*, **65**, 194–208.

[82] **Akduman, I. and Kress, R.**, 2003. Direct and inverse scattering problems for inhomogeneous impedance cylinders of arbitrary shape, *Radio Science*, **38**, 1055–1064.

[83] **Smith, R. T.**, 1985. An inverse acoustic scattering Problem for an obstacle with an impedance boundary condition, *Jour. of Math. Analy. and App.*, **105**, 333–356.

[84] **Lin, H.**, **Kindermann, S. and Sini, M.**, 2009. Reconstruction of shapes and impedance functions using few far-field measurements, *J. of Comp. Phys.*, **228**, 717–730.

[85] **Kress, R.**, **Yaman, F.**, **Yapar, A. and Akduman, I.**, 2009. Inverse scattering for an impedance cylinder buried in a dielectric cylinder, *Inverse Problems in Science and Engineering*, **17**, No:4, 473-488.

[86] **Kleinman, R. E. and Van den Berg, P. M.**, 1994. Two-dimensional location and shape reconstruction, *Radio Science*, **29**, No:4, 1157–1169.

[87] **Belkebir, K.**, **Kleinman, R.E. and Pichot, C.**, 1997. Microwave imaging - location and shape reconstruction from multifrequency scattering data, *IEEE Trans. on Microwave Theory and Tech.*, **45**, No:4, 469–476.

[88] **Yaman, F. and Yapar, A.**, 2008. Shape reconstructions of sound-soft obstacles buried in arbitrarily shaped penetrable cylinders *Spring Conference Widening Horizons in Acoustic Research*, 252–259.

[89] **Yaman, F.**, 2009. Location and shape reconstructions of sound-soft obstacles buried in penetrable cylinders, *Inverse Problems*, **25**, No:6, 1-17.

[90] **Angell, T.S. and Kirsch A.**, 1992. The conductive boundary condition for Maxwell Equations, *SIAM J. Appl. Math.*, **52**, 1597-1610.

[91] **Hettlich, F.**, 1996. Uniqueness of the inverse conductive scattering problem for time-harmonic electromagnetic waves, *SIAM J. Appl. Math.*, **56**, 588-601.

[92] **Gerlach, T. and Kress, R.**, 1996. Uniqueness in inverse obstacle scattering with conductive boundary condition, *Inverse Problems*, **12**, 619-625.

[93] **Torun, G. and Ates, U.D.**, 2006. Properties of the far field operator in the inverse conductive scattering problem, *Applied Math. and Comp.*, **175**, 1503-1514.

[94] **Yaman, F.**, 2008. Numerical solution of an inverse conductive boundary value problem, *Radio Science*, **43**, Issue:6, RS6004.

[95] **Yaman, F.**, 2008. Inverse scattering of an arbitrarily shaped buried scatterer with conductive boundary condition, *8th. World Congress on Computational Mechanics , 5th European Congress on Computational Methods in Applied Sciences and Engineering.*

[96] **Rundell, W.**, 2008. Recovering an obstacle and a nonlinear conductivity from Cauchy data, *Inverse Problems*, **24**, 1-22, DOI:10.1088/0266-5611/24/5/055015.

[97] **Rundell, W.**, 2008. Recovering an obstacle and its impedance from Cauchy data, *Inverse Problems*, **24**, 1-22, DOI:10.1088/0266-5611/24/4/045003.

[98] **Colton, D. and Kress, R.**, 1983. Integral equation methods in scattering theory, Wiley-Interscience Publications, New York.

[99] **Kussmaul, R.**, 1969. Ein numerisches Verfahren zur Lösung des Neumannschen Außenraumproblems für die Helmholtzsche Schwingungsgleichung, *Computing*, **4**, 246–273.

[100] **Martensen, E.**, 1963. Über eine Methode zum raumlichen Neumannschen Problem mit einer Anwendung für torusartige Berandungen, *Acha Math.*, **109**, 75–135.

[101] **Kress, R.**, 1995. On the numerical solution of a hypersingular integral equation in scattering theory, *Journal of Computational and Applied Mathematics*, **61**, 345–360.

[102] **Eom, H. J.**, 2004. *Electromagnetic wave theory for boundary-value problems. An advanced course on analytical methods*, Springer Verlag, Berlin Heidelberg.

[103] **Harrington, R.F.**, 1967. Matrix methods for field problems, *Proceedings of the IEEE*, **55**, 136–149.

[104] **Richmond, J.H.**, 1965. Scattering by a dielectric cylinder of arbitrary cross section shape, *IEEE Transactions on Antennas and Propagation*, **13**, 334–341.

[105] **Stoer, J. and Bulirsch, R.**, 1992. *Introduction to numerical analysis, Second Edition,* Springer-Verlag, New York.

[106] **Kress, R.**, 1998. *Numerical analysis, Springer-Verlag* , New York.

[107] **Balanis, C. A.**, 1989. *Advanced engineering electromagnetics*, John Wiley & Sons, Inc., New York.

[108] **Hoppe, D.J. and Rahmat-Samii, Y.** , 1995. *Impedance Boundary Conditions in Electromagnetics*, Taylor and Francis, New York.

APPENDICES

APPENDIX A. : PARAMETRIC REPRESENTATION OF THE CURVES

APPENDIX B. : TIKHONOV REGULARIZATION

APPENDIX C. : LEAST SQUARES APPROXIMATION

APPENDIX A. : PARAMETRIC REPRESENTATION OF THE CURVES

For the numerical applications of the thesis the boundary curves Γ_0 and Γ_1 were chosen as one of the boundaries given in Table 1.

Table 1: Parametric Representation of the Boundary Curves

Contour Type:	Parametric Representation:
Apple Shaped:	$\Gamma^{(a)} = \left\{ \dfrac{0.5+0.4\cos t+0.1\sin 2t}{1+0.7\cos t}(\cos t, \sin t) : t \in [0,2\pi] \right\}$
Circle:	$\Gamma^{(c)} = \{c_0(\cos t, \sin t) : t \in [0,2\pi]\}$, c_0 : constant
Ellipse:	$\Gamma^{(e)} = \{(e_0 \cos t, e_1 \sin t) : t \in [0,2\pi]\}$, e_0, e_1 : constant
Kite Shaped:	$\Gamma^{(k)} = \left\{(\cos t + 1.3\cos^2 t - 0.8, 1.5\sin t) : t \in [0,2\pi]\right\}$
Peanut Shaped:	$\Gamma^{(p)} = \left\{ \sqrt{\cos^2 t + 0.25\sin^2 t}\,(\cos t, \sin t) : t \in [0,2\pi] \right\}$
Rounded Square:	$\Gamma^{(s)} = \left\{ \dfrac{3}{2}(\cos^3 t + \cos t, \sin^3 t + \sin t) : t \in [0,2\pi] \right\}$
Rounded Rectangle:	$\Gamma^{(r)} = \left\{ \dfrac{2}{3}(\sin^{10} t + \dfrac{2}{3}\cos^{10} t)^{-0.1}\,(\cos t, \sin t) : t \in [0,2\pi] \right\}$
Rounded Triangle:	$\Gamma^{(t)} = \{(2+0.3\cos 3t)\,(\cos t, \sin t) : t \in [0,2\pi]\}$

APPENDIX B. : TIKHONOV REGULARIZATION

Let's consider a compact linear operator $A : X \mapsto Y$ from a normed space X into a normed space Y. Then the equation

$$A\varphi = f, \tag{1}$$

is called well-posed, in the case of A is bijective and the inverse $A^{-1} : Y \mapsto X$ is continuous. Otherwise the equation is called ill-posed and to obtain a stable approximate solution of the ill-posed equation we replace the following equation

$$\alpha\varphi + A^*A\varphi = A^*f, \tag{2}$$

with the (1), where $A^* : Y \mapsto X$ is the adjoint operator of the A and α is a positive parameter. Then according to theorem 4.13 in the book [43] for each $\alpha > 0$ the operator $\alpha I + A^*A : X \mapsto X$ is bijective and has a bounded inverse.
It is also noted in the book [43] that the choice for selecting the regularization parameter will generally be *trial* and *error*. For this one choses a few different parameters α in a range and check the most reasonable result.

APPENDIX C. : LEAST SQUARES APPROXIMATION

Let's consider an overdetermined system of equations

$$\sum_{j=1}^{n} A_{ij} X_j = B_i\,, \qquad i = 1, 2, \cdots, m\,, \qquad m > n\,, \tag{3}$$

for m linear equations with n unknowns. In order to find a solution in the least squares sense we need to find the values of X_j that minimizes the following expression

$$\sum_{i=1}^{m} \left| B_i - \sum_{j=1}^{n} A_{ij} X_j \right|^2_{min} . \tag{4}$$

Then according to the theorem 4.8.1.3 of the book [105] the optimal value of $\bar{X}$ is a solution of the following *normal equation*

$$(A^T A)\bar{X} = A^T B\,, \tag{5}$$

where T denotes the matrix transpose .

CURRICULUM VITAE

Candidate's full name: Fatih Yaman

Place and date of birth: Istanbul, 26 June 1978

Permanent Address: Electrical and Electronics Engineering Faculty,
Istanbul Technical University, 34469 Maslak, Istanbul, Turkey.

Universities and Colleges attended:
1989 - 1996 : Çanakkale Milli Piyango Anatolian High School
1997 - 2001 : Istanbul University, Electrical and Electronics Engineering
2001 - 2004 : Istanbul University, Electrical and Electronics Engineering, Master Program
2004 - 2009 : Istanbul Technical University, Institute of Science and Technology, Telecommunication Engineering PhD Program
2006 - 2008 : Georg-August University of Goettingen, Mathematics Faculty, Numerical and Applied Mathematics Institute (Visiting Scholar)

List of Publications:

International Journal Papers:

- **Yaman F.** and Şimşek S ., 2007: Neural Network Approach to Determine Non Smooth One - Dimensional Profiles in Inverse Scattering Theory. *Microwave. and Opt. Tech. Let.*, Vol. 49, No. 12, 3158-3162.
  Erratum: **Yaman F.** and Şimşek S., 2008: Neural Network Approach to Determine Non Smooth One - Dimensional Profiles in Inverse Scattering Theory, *Microwave. and Opt. Tech. Let.*, Vol. 50, No.2, 549.
- **Yaman F.**, 2008: Numerical Solution of an Inverse Conductive Boundary Value Problem, *Radio Science*, 43, RS6004. 1-10.
- **Yaman F.** and Şimşek S., 2009: Shape Reconstruction of an Inhomogeneous Impedance Cylinder via Potential and Neural Network Approach, *Microwave. and Opt. Tech. Let.*, Vol. 51, No. 1, 119-124.
- Kress R., **Yaman F.**, Yapar A., Akduman I., 2009: Inverse scattering for an impedance cylinder buried in a dielectric cylinder, *Inverse Problems in Science and Engineering*, Vol. 17, No.4, 473-488.
- Kress R., Tezel N., **Yaman F.**, 2009: A second order Newton method for sound soft inverse obstacle scattering, *Jour. on Inverse and Ill-Posed Problems*, 17, 173-185.
- **Yaman F.**, 2009 : Location and shape reconstructions of sound-soft obstacles buried in penetrable cylinders, *Inverse Problems*, Vol. 25, No. 6, 1-17.
- **Yaman F.**, 2009: A Combination of Shape and Conductivity Function Reconstruction Methods for an Inverse Boundary Value Problem, *Wave Motion*, DOI: 10.1016/j.wavemoti.2009.10.004, paper in press.

International Conference Papers:

- **Yaman F.** and Yapar A., 2006: One-dimensional profile inversion of a planar layer bounded by an inhomogeneous impedance boundary, *XIth International Seminar / Workshop Direct and Inverse Problems of Electromagnetic and Acoustic Wave Theory, DIPED 2006*, 65-70.
- **Yaman F.** and Yapar A., 2008: Shape reconstructions of sound-soft obstacles buried in arbitrarily shaped penetrable cylinders, *Widening Horizons in Acoustic Res. 2008, Proceedings of the Institute of Acoustics*, Vol.30. Pt.2, 252-259.
- **Yaman F.**, 2008: Inverse scattering of an arbitrarily shaped buried scatterer with conductive boundary condition , *8th. World Congress on Computational Mechanics (WCCCM8), 5th European Congress on Computational Methods in Applied Sciences and Engineering (ECCOMAS 2008) (Eds. B.A. Schrefler and U. Perego),* Venice, Italy.

National Conference Papers:

- **Yaman F.** and Yapar A., 2006: One-dimensional profile reconstruction of a planar layer located over perfectly conducting plane, *URSI-Türkiye 2006 Genel Kurulu ve Bilimsel Kongresi*, 149-151.